Theses and Dissertations

May 2023

Testing the Use of Anisotropy of Magnetic Susceptibility (AMS) in Determining Genetic Origins of Paleoproterozoic Diamictites

Miles A. Harbury
University of Wisconsin-Milwaukee

TESTING THE USE OF ANISOTROPY OF MAGNETIC SUSCEPTIBILITY (AMS) IN DETERMINING GENETIC ORIGINS OF PALEOPROTEROZOIC DIAMICTITES

by

Miles A. Harbury

A Thesis Submitted in

Partial Fulfillment of the

Requirements for the Degree of

Master of Science

in Geology

at

The University of Wisconsin-Milwaukee

August 2023

ABSTRACT

TESTING THE USE OF ANISOTROPY OF MAGNETIC SUSCEPTIBILITY (AMS) IN DETERMINING GENETIC ORIGINS OF PALEOPROTEROZOIC DIAMICTITES

by

Miles A. Harbury

The University of Wisconsin-Milwaukee, 2023
Under the Supervision of Professors Julie Bowles and John Isbell

The Huronian Supergroup (2.4-2.1 Ga) in Ontario, Canada is widely accepted as an important stratigraphic interval for interpreting Paleoproterozoic climate. This is because it contains some of the oldest glaciogenic rocks on the planet. However, massive and poorly-stratified diamictites in the Gowganda Formation of the Huronian Supergroup have varying depositional interpretations among sedimentologists (subglacial, rainout, sediment gravity flow etc.). Diamictites can occur from a variety of processes and, therefore, proper depositional interpretation is essential for unraveling detailed environmental conditions at the time of deposition.

Anisotropy of magnetic susceptibility (AMS) looks at the orientation of magnetic particles within a rock and coupled with sedimentary investigation, can help interpret depositional processes. Rock magnetic data show that magnetism is carried by multi-vortex (titano)magnetite in fine-grained facies and includes the addition of a higher- coercivity contribution (potentially diagenetic goethite) in some sandstone facies. Most magnetic fabrics

are oblite in shape and oriented transverse to flow, although vertical fabrics were found in sites that exhibited substantial deformation or dewatering. Results and observations from this project suggest that Gowganda sedimentation was dominated by sediment gravity flows, deposited on a marine post-glacial slope with a southwestern transport direction. Interpretation of depositional processes through a combination of AMS and sedimentologic observation provide a more comprehensive understanding of the environmental conditions controlling deposition, and in this case, painting a more elaborate picture of Paleoproterozoic climate transitions.

In contrast with subglacially derived diamictites, which are deposited directly under glacial ice, those produced by sediment gravity flows suggest a more glacially distal to non- glacial environment. The presence of bedded diamictites, water escape structures, quarter structures around clasts, a general lack of shear horizons and striated/faceted clasts as well as an abundance of flow-transvers magnetic fabrics observed in most Gowganda facies suggest this more distal environment. However, subglacial deformation and deposition cannot be entirely ruled out for one oriented and striated boulder bed horizon producing flow-aligned magnetic fabrics; both characteristics of subglacial processes.

TABLE OF CONTENTS

LIST OF FIGURES

LIST OF TABLES

ACKNOWLEDGEMENTS

Introduction

Huronian Glaciation

The Huronian Supergroup, deposited on the southern margin of the Superior craton,(~ 30°
north of the equator and 2.4-2.1 Ga) is a cyclic succession (~12,000 m thick*)* of diamictite
facies followed by coarsening upward packages of laminated, siltstone and sandstones (e.g.
Young, 1991; Fig. 1). Three diamictite bearing units are widely acknowledged as glacially-
derived, beginning with the Ramsey Lake Formation of the Hough Lake Group, the Bruce
Formation of the Quark Lake Group, and the Gowganda Formation of the Cobalt Group (The
focus of this project; *Figure 1*). One early interpretation of the Huronian diamictites states that
glaciogenic deposition occurred as basin level was shallow, followed by rapid downwarp as a
result of weight applied to the basin by advancing glacial ice, subsiding to the point where fine
grained sediments were deposited. This was followed by a reactionary uplift (glacial rebound)
after ice retreated and another then another similar cycle *(Frarey and Roscoe, 1970).* Young
(1991) and Casshyap (1969) both suggested that glaciation is key to the stratigraphic cyclicity
of diamictite facies during the Huronian succession and that these sediments are evidence of
glacial advance and retreat.

The Gowganda Formation

The Gowganda Formation is the latest glacial cycle in the Huronian Supergroup and represents
the beginning of the end of the Huronian glaciation and a transition out of a "Snowball Earth"
period. It outcrops in Ontario Canada, north of Lake Huron near the towns of Elliot Lake, Bruce
Mines, Whitefish Falls, and Cobalt (*Figure 2*). Like most of the Huronian Supergroup, the

1

Gowganda includes massive, poorly sorted diamictite followed by coarsening upward sequences

(*Figure 1*), however the presence of bedded diamictites and laminated laminated facies are
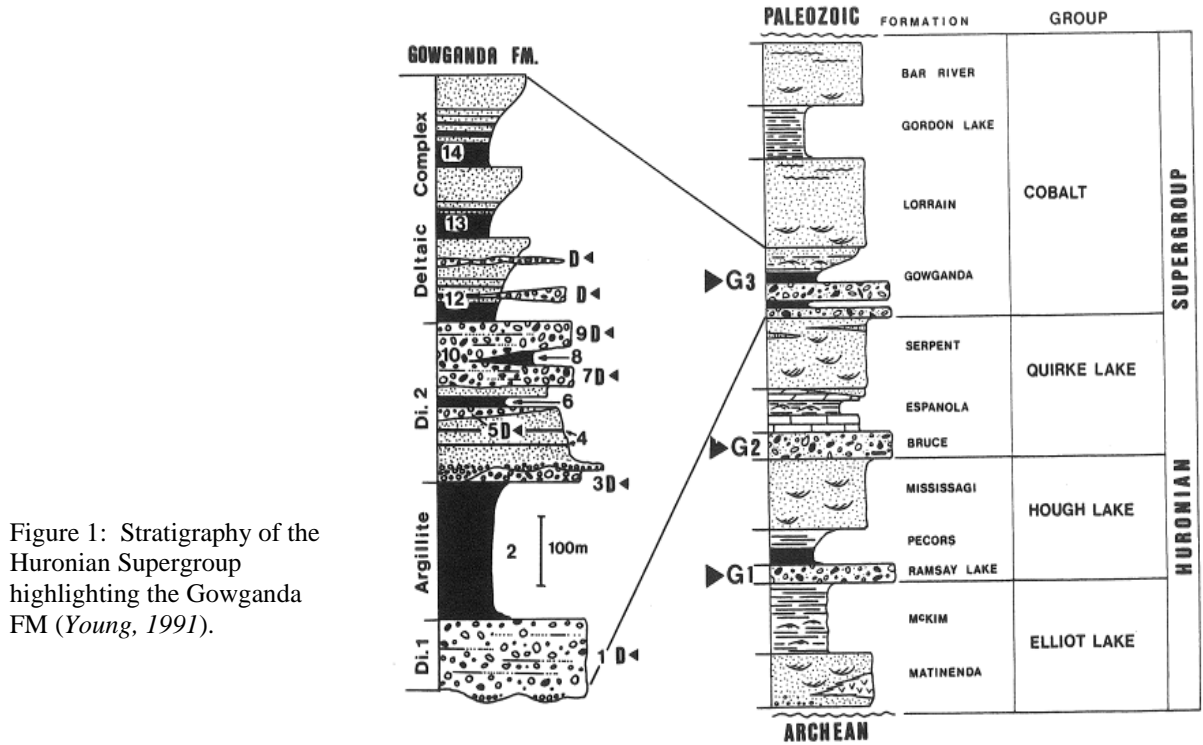
Figure 1: Stratigraphy of the Huronian Supergroup highlighting the Gowganda FM (*Young, 1991*).

Figure 2: Gowganda outcrop locations throughout Ontario (left) and investigated outcrops north of Elliot Lake (right).

unique to the Gowganda. Interpretations of Gowganda diamictite depositional processes differ among geologists. Some argue for sub-glacial derivation (*Lindsey, 1969; Mustard and Donaldson, 1987; Menzies, 2000*) and some arguing in favor of deposition by mass transport/sediment gravity flows (*Miall, 1983; 1985*). These hypotheses suggest different origins: a possible difference in climatic setting and proximity to glacial ice. Therefore, this study will contrast subglacially derived diamictites (deposited under a glacier) with those produced by mass-transport or sediment gravity flows (deposited away from glacial ice or in non-glacial settings). Deciphering between these processes will heighten our understanding of Paleoproterozoic glaciation, and climate at the end of the Huronian "Snowball Earth" period.

Diamictite forming processes

Diamictites form by a variety of processes, each representing different environmental conditions and proximity to glacial ice: settling of fines from meltwater plumes while coarse debris is released from floating ice, sedimentary mass-transport (slides, slumps), sediment gravity flows (debris flows, concentrated density flows, turbidites), or subglacially as lodgement till (*Figure 3*; *Eyles*, 1987; *Benn and Evans, 2010; Vesely, 2020; Isbell et al., 2021*). Although distinguishing between diamictite-forming processes can prove extremely difficult, examination of sedimentary characteristics (micro and macro scale) can aid in the interpretation of diamictite genetic origins (*Menzies, 2022*).

3
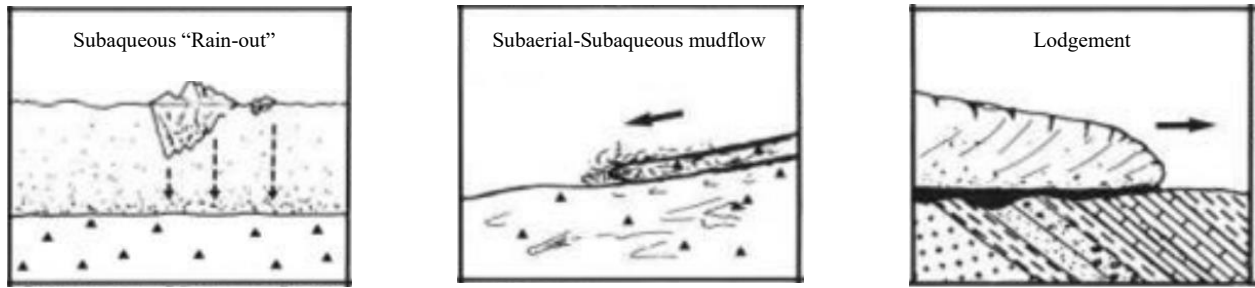
Figure 3: Main diamictite-forming processes (*Eyles, 1987*).

In the absence of (or to supplement) visual evidence like striated clasts, pebble fabrics, and sedimentary structures, it is helpful to "zoom in" to the diamictites fine-grained matrix and observe a sample on a micro scale. Magnetite or other magnetic minerals are often found in glaciogenic sediments where the host rock was completely pulverized, and the particles can move independently due to various geomorphic processes. The preferred alignment, or the lack thereof, of these magnetic particles (magnetic fabric) can be observed through the statistical alignment of magnetic particles, (anisotropy of magnetic susceptibility; AMS) and used as a proxy for rock fabric to be used in interpretation of relative shear-stress applied during deposition and the direction of sedimentary transport (*Eyles, 1987; Hooyer et al., 2008; Iverson, 1997*).

Rain-out/ice-rafting

Rafted debris is a major component of glacimarine sediment and can provide information on the extent of glacial processes and the characteristics of glaciomarine conditions. Sediment is actively incorporated onto ice via glacial erosion, colluvial, fluvial, and aeolian processes and/or frozen into ice via the littoral environment. These sediments are then distributed through bergs or sea ice resulting in the liberation of ice rafted debris as rain-out or dump (*Gilbert, 1990*). Outsized clasts that have rained-out from floating ice (drop-stones) induce bending, penetration,

rucking, and rupture of underlying sedimentary layers as well as the bending, on-lap, and rupture of proceeding sedimentary layers (*Figure 4*; *Thomas and Connell, 1985*). Preferred orientation of a drop-stone's long-axis may be vertical in sediments soft enough to allow penetration but firm enough to preserve the clast's orientation as it falls thought the water column. In sediments that are either very soft or extremely compacted, clasts tend to fall on their side after impact. It is important to note that the presence of rafted debris may not be directly correlated with glacial events, just as the absence of rafted debris is not substantial evidence of a non-glacial environment (*Gilbert, 1990*). Sea and lake ice can also raft particles (*Lisitzin, 2002; Tremblay et al. 2015*).
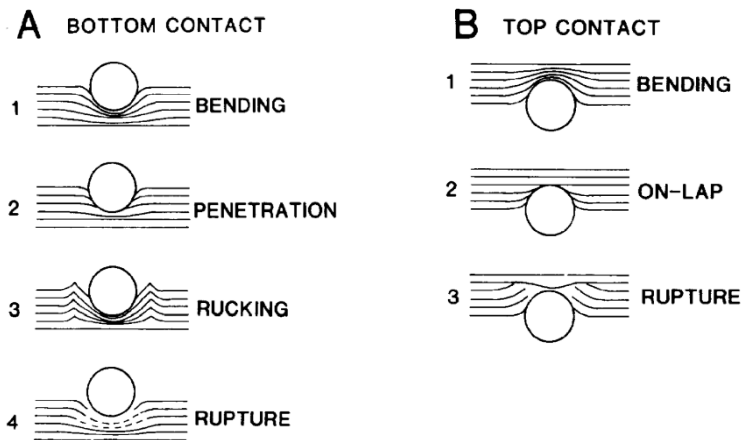
Figure 4: Contacts between dropstones and sedimentary layers (*Thomas and Connell, 1985*).

Sedimentary Mass-transport

Sedimentary mass-transport events can be split into two types: slides and slumps. Slides often leave internal structures within a block undisturbed as they move down a slope but may exhibit compressional or tensional deformation. Slumps show more extensive internal deformation within transported blocks that on large scales may look similar to glaciotectonics. Consideration of paleoslope/paleotopography and surrounding facies is required for accurate

5

interpretation. If transport occurs over long-distance and sufficient water is added to the matrix, slumps and slides can disaggregate, generating debris flows and turbidites (*Benn and Evans, 2010; Rodrigues et al., 2020; Isbell et al., 2021*).

Sediment gravity flows

Sediment gravity flows (SGFs; *Figure 5*) are gravity-driven flows of sediment and water involving grain–grain and grain–fluid interactions (*Figure 5; Hutter and Rajagopal, 1994; Iverson, 1997; Mulder and Alexander, 2001; Talling et al., 2012; Pickering and Hiscott, 2016*). Initially, gravity acts on solid particles in the mixture, inducing downslope flow, gravity pulling the grains and the grains pulling the water. If sufficient potential energy is converted into kinetic energy, transport is induced and will continue if the shear stress generated by the downslope gravity component exceeds frictional resistance to flow and if the grains are inhibited from settling by one of several support mechanisms (turbulence, buoyancy, grain interaction, poor pressure, or matrix strength; *Pickering and Hiscott, 2016*). The presence or absence of matrix affects cohesion of SGFs and plays a major role in depositional character and behavior (*Eyles, 1987*). Flows with high mud content are more cohesive and will cease to move if the downslope component of gravity is not sufficient to generate the required shear stress along the basal surface of the flow. Once moving, matrix strength is believed to play a role in reducing the tendency to overcome a certain amount of residual frictional and cohesive strength necessary for large clasts to settle (*Pickering and Hiscott, 2016*).

Figure 5:
Subaquiouse flows ranging from cohesive to cohesionless depicted with associated diagrams of flow structure, behavior, and depositional sequences (left: *Haughton, 2009*; right: *Mulder and Alexander 2001*).

7

Figure 6: SGF diagram depicting multiple phases of flow transition. (*Pickering and Hiscott, 2016*)

Depositing sheet-like or lobate masses that range from centimeters to hundreds of meters thick and containing a wide range of particle size, SGFs can occur incrementally (alternating low/high density deposits i.e. turbidites/concentrated density flows) or *en masse,* producing ungraded debris flow deposits (*Talling et al., 2012*). The concentration of cohesive mud in a flow changes flow viscosity profoundly affecting turbulence, processes of sediment deposition, resulting deposit types, and whether bedforms develop (*Iverson, 1997; Sumner et al., 2009*; *Baas et al., 2011*). SGFs are subdivided according to their rheological behavior into cohesive (debris flows), non-cohesive flows (inflated sand flows), concentrated density flows (high-density turbidity currents), and turbidity currents (low-density turbidity currents), and can transition between subdivisions (phases) within one flow event (*Pickering and Hiscott, 2016*) (*Figure 6*).

Cohesive flows, which have matrix strength resulting from electrostatic attraction between mud particles, differ from other flows by their pseudoplastic rheology, and do not tend to become diluted by particle loss (via deposition) or entrainment of ambient water. Debris flows have cohesive mud contents sufficient to support sand grains and typically contain sand and mud.

8

Flows with higher cohesive strength may have the ability to carry outsized clasts whereas flows with lower cohesive strength may contain only mud and sand (*Talling et al., 2012; Pickering and Hiscott, 2016*).

The origin and transport process of poorly cohesive debris flows are not yet well-understood. However, a continuum exists between non-cohesive and cohesive flows, as the amount of fine-mud increases (*Talling et al., 2012*). Non-cohesive flows (inflated sand flows) lack mud altogether and consist of well to poorly sorted sand to pebble-sized gravel, with ice-proximal flows containing an abundance of boulder-sized material. Generally deposited incrementally, cohesionless flows are commonly erosive at their base and can form deep, channelized scours incorporating underlying material into the flow and sometimes producing inverse grading above the basal contact either by kinetic sieving or by dispersive pressure, generated by colliding grains (*Ben and Evans, 2010; Pickering and Hiscott, 2016; Talling et al., 2012*). The behavior of non-cohesive flows is related directly to the relative proportion of grains and water. Liquified or fluidized sandy flows may exhibit dewatering structures, evidence of the upward displacement of sediment by escaping pore fluid, and may include subvertical pipes, swirled laminations, and dish structures (*Young, 1991; Ben & Evans, 2010*). Clasts in non-cohesive flows typically show a strong long-axis orientation and imbrication in the direction of flow resulting from the rotation of clasts in a shearing medium (*Massari, 1984; Ben and Evans 2010*).

Low-density flows (turbidity currents) are fully turbulent at their bed, allowing deposition of plane bed laminations and ripple cross-laminated intervals (Baas et al., 2011), and the tapering of turbidite beds as a result of unhindered settling (Talling et al., 2007c). In contrast, high-density

flows (concentrated density flows) have higher sediment concentration near their bed leading to the rapid deposition and damping of turbulence, hindered settling and a lack of bedforms (*Talling et al., 2012*). In both high and low-density flows, deposition occurs as flows slow or become less turbulent, reflecting the rapid deposition of course material and the transport of fine sediment into deeper water (*Ben & Evans, 2010*). Repeated divisions are thought to form by pulsed flows (*Haughton, 1994*) and it is suggested that outsized clasts can be transported by gliding along boundaries between regions of contrasting density (*Postma, 1988b*).

Glacial tills

Glacial tills are produced from the subglacial deposition or erosion of sediment and can undergo a wide range of deformation. Tills can be categorized between two endmembers: *traction till* (*Evans et al., 2006; Evans et al., 2018*) and *glacial tectomict* (*Menzies et al., 2006*), based on degree of deformation. Observations on contemporary glaciers reveal that beds are most likely mosaics of deformation and sliding, and warm based and cold based conditions. Spatial and temporal variability in ice-bed coupling due to changes in pressure distribution of the basal water system leads to variability in basal motion mechanics, resulting in a patchwork of sticky spots and areas of stick-slip sliding (*Fischer et al., 1999; Fischer and Clarke, 2001; Evans et al., 2006*). It is extremely likely that most tills in the geological record are hybrids, produced by the range of processes operating in the subglacial traction zone (*Evans et al., 2006*).

Traction till (*Figure 7A*; *Dreimanis, 1989*) is sediment deposited by plastering of glacial debris from a sliding glacier sole due to pressure melting or other mechanical processes (*Dreimanis,*
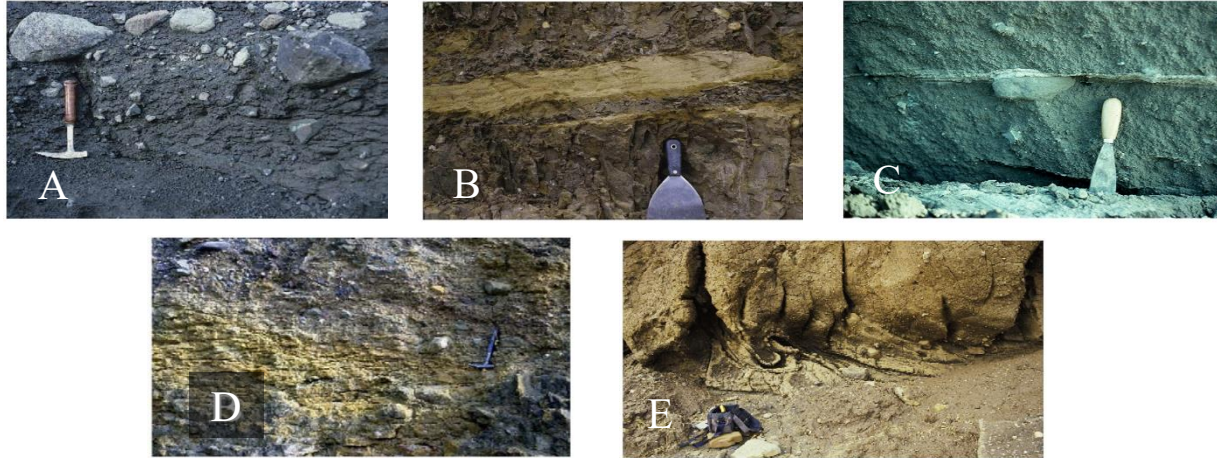
Figure 7:
A) Highly fissile, compacted diamicton with bullet-shaped and facetted clasts, typical of subglacial lodgement till. B) soft sediment intra-till lens, typical of melt-out till. C) single horizontal stringer of stratified sand in till matrix interpreted as the product of thin water films at the ice-bed interface *(Photo by Jan Piotrowski)*. D) Glacitectonically thrust and stacked slices of siltstone bedrock grading vertically to subglacial till *(Hiemstra, and Rijsdijk 2003)*. E) Deformation till showing fold structures due to preferential weathering of sand-rich intra-till wisps *(Evans et al., 2006)*.

1989; Evans et al., 2006). Often overconsolidated (*Ben and Evans, 1998*), traction till deposits can be massive but often show subhorizontal jointing (shear-planes), and typically display bi-modal to multi-modal grainsize distribution with distinct peaks in the silt and gravel size range depending on the integrity of host-rock lithology (*Haldorsen, 1981*). Commonly imbricated upglacier with an A-B plane (long axis – intermediate axis) parallel to the plane of shear, clasts in traction tills show strong preferred orientation parallel with glacial flow and are typically asymmetrical and elongate (bullet shaped) with smooth stoss sides (upglacier) and fractured/plucked lee sides (downglacier) (*Boulton, 1978; Benn, 1994a*). Perhaps the most telling feature in differentiating glacial tills from other diamictite deposits is the upward increase of shear stress in sediments nearer to (but only below) a shear plane (*Figure 8*). Fine-grained tills with a small numbers of clasts facilitate sliding and clast ploughing, when porewater pressure is high enough, lowering the effective stress of the substrate, and basal shear stress is not high

11

enough to deform sediment at depth.

producing a shear zone of as thin as 0.01 m

but can grow thicker as shearing persists

over time (*Tulaczyk, 1999; Evans et al.,*

2006).

Often associated with coarse-grained tills,

glacial tectomict (*Figure 7D*) is rock or

sediment that has been structurally

deformed by subglacial shearing but retains

some of the structural characteristics of the

parent material, reflecting its strain history

and often producing folds or breccias along

Figure 8: Idealized reconstruction of the subglacial deforming till layer and the development of porewater migration pathways, till-matrix framework and till pebbles and their relationship to horizon development and geotechnical properties *(Evans 2006).*

fault planes (*Benn and Evans, 2010; Menzies et al., 2006*). A result of strong ice-till coupling,

deformation can reach depths over 1 m into the substrate (*Tulaczyk, 1999; Evans et al., 2006*).

Under low shear-strain, glacial tectomicts undergo brittle deformation and may take-on

characteristics similar to lodgment till (bullet-shaped clasts aligned parallel to glacial flow).

Under high shear-strain however, glacial tectomicts experience ductile deformation, developing

subhorizontal banding that is usually lithologically distinct. Deformation ranges from the

bending of sediment around deforming material, displaying asymmetric folds around clasts, to

large-scale folding of till bands, and can potentially be mistaken for debris flow deposits (*Hart &*

Roberts, 1994; Ben and Evans, 2010). Glacial tectomicts commonly display increasing

deformation up a vertical section from mildly distorted to total disaggregation, homogenized by

shearing ("deformation till") and include a higher percentage of fractured clasts with a more spatially consistent preferred orientation compared to clasts in debris flow deposits.

Rock Magnetic Properties

Magnetic properties arise from the motion of electrically charged subatomic particles (*Tarling and Hrouda, 1993; Tauxe et al., 2018*), indicating that all materials are susceptible to magnetism, even those that do not hold it permanently. Magnetic susceptibility is a parameter used to describe the nature and intensity of a material's response to an external magnetic field. Susceptibility can be represented by the equation $M = \chi B$, where B is the strength of the applied magnetic field, M is the strength of the induced magnetization, and χ is a constant of proportionality defined as susceptibility, which can be used as a (unitless) scalar or as a tensor where it is directionally dependent as in AMS studies (*Amato, 2017*).

Types of Magnetism

Depending on the nature of magnetization, materials can be classified based on how they respond to an applied field either as diamagnetic, paramagnetic, or ferromagnetic (*Figure 9*) (*Tarling and Hrouda, 1993; Tauxe et al., 2018*). Diamagnetic materials (*Figure 9a*) like calcite and quartz have low or negative susceptibility, typically on the order of 10^{-5} to 10^{-6} SI-units (*Tarling and Hrouda, 1993; Baas et al., 2007*) and magnetization is induced in the direction opposite to the applied field. In paramagnetic material (*Figure 9b*) like olivine, amphibole, pyroxene, and biotite, magnetism is induced in the same direction as the applied field and has a positive susceptibility, typically on the order of 10^{-2} to 10^{-4} SI-units (*Tarling and Hrouda, 1993;*

Baas et al., 2007). Both diamagnetic and paramagnetic materials do not hold magnetic remanence and loose magnetization as soon as the field is removed.

Materials that carry magnetism after the removal of an applied field are ferromagnetic (*sensu lato*) and hold remanent (permanent) magnetization (*Figure 9c*) on the order of 10^{-2} to 10^0 SI-units (*Tarling and Hrouda, 1993; Baas et al., 2007*). Ferromagnetic (*sensu lato*) materials can be separated into three types: ferromagnetic (*sensu stricto*) (*e.g., Fe^0, Figure 9c*),

Figure 9: Illustration depicting the three different classes of magnetization and arrangement of electron spins, both in the presence and absence of an applied field. Black arrows to the left of boxes show the orientation of the applied field, and white arrows to the right of boxes show the orientation of the resulting magnetization. Figure used from *Tarling and Hrouda, 1993*).

ferrimagnetic (e.g., magnetite) and antiferromagnetic (e.g., hematite). Only a very small fraction of ferromagnetic minerals is needed (~0.1% volume of the whole rock) to control the susceptibility anisotropy of a sample (*Tarling and Hrouda, 1993*). In the absence of ferromagnetic minerals, paramagnetic contributions tend to dominate over diamagnetic contributions provided they comprise more than 1% of the rock (*Tarling and Hrouda, 1993*).

14

Domain state

On subatomic level, magnetization of paramagnetic and ferromagnetic materials arises from unpaired electron spins. Electron spins seek the most efficient configuration to minimize total energy (*Figure 10*). In small particles of magnetite (< 40 nm), electron spins are parallel, and the particle is uniformly magnetized throughout (single domain, SD). As particle size increases (~80 nm), the lowest energy configuration involves a non-uniform spin structure where the particle is sub-divided into multiple uniformly magnetized domains, separated by domain walls (multi-domain, MD). Between SD and MD are a range of nonuniform spin structures such as flower or vortex (*Tauxe et al., 2018*), a state sometimes referred to as "pseudo-single domain (PSD)".
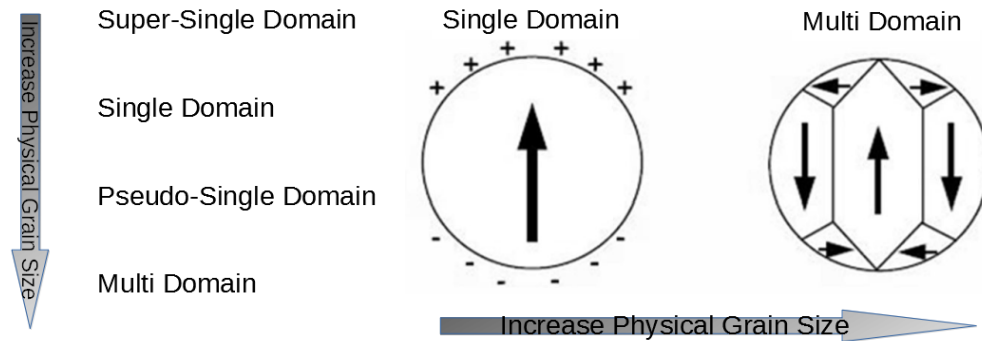
Figure 10: Diagram of single domain and multiple domain magnetic particles as related to grain size. Figure modified after Butler, 1992.

Hysteresis data can help in identifying a sample's dominant type of magnetism and domain-state and can be collected at room temperature using a vibrating sample magnetometer (VSM). The VSM measures a sample's magnetization in an applied field by mechanically vibrating the sample between a system of pickup coils. B is cycled from zero to +1T, back to zero to -1T, while magnetization (M) values are measured (*Tauxe et al., 2018*). The shape of the hysteresis

loop is dictated by the magnitude of the maximum possible magnetization (saturation

magnetization, Ms), the magnetization able to be stored in the rock in zero field (remnant

magnetization, Mr), and the strength of the inducing field where magnetization is equal to zero

(magnetic coercivity, Bc) (Figure 11). By observing the shape of the hysteresis loop, general

information about the magnetic contributions of a sample can be inferred.

Since diamagnetic and paramagnetic minerals do not carry remanent magnetization, they have

null values of coercivity and saturation remanent magnetization and thus have no magnetic

hysteresis. They also do not saturate in normal laboratory fields and therefore only show linear

negative and positive relationships respectively (*Tauxe et al., 2018*). Ferromagnetic minerals

carry remanent magnetization and thus retain magnetization in zero field. Their coercivity is

dependent upon grain size and composition. As SD grains possess high values of coercivity, their

loops tend to be more open than those of vortex or MD grains and they have higher values of

M_r/M_s.
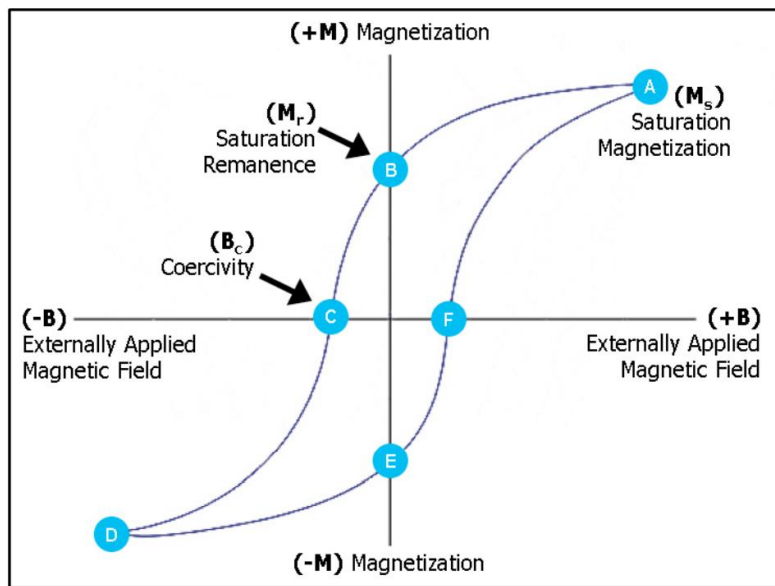
Figure 11: Idealized hysteresis loops of end-member behaviors: (a) diamagnetic, (b) paramagnetic, (c) Ferromagnetic. The size (thickness) of the loop in (c) reflects differences in ferromagnetic grain sizes. Figure from *Tauxe et al., 2018.*

For mixtures of dia/paramagnetic and ferromagnetic populations, we can subtract the linear

paramagnetic or diamagnetic susceptibility at high-fields (Xhs), to isolate the ferromagnetic

signal. To estimate average ferromagnetic domain state, hysteresis parameters are often

summarized on a Day plot (*Day et al., 1977*) of Mr/Ms vs Bcr/Bc (Bcr = coercivity of remanent

magnetization) (*Figure 12*). Dunlop (2002) made theoretical calculations of hysteresis

parameters for magnetite in different domain states (and mixtures of domain states). While

helpful for identifying trends within or between data sets, the Day plot is less useful for

identifying specific domain states in natural materials which typically have complex mixtures of

magnetic mineralogy and grain size (*Roberts et al., 2018*).
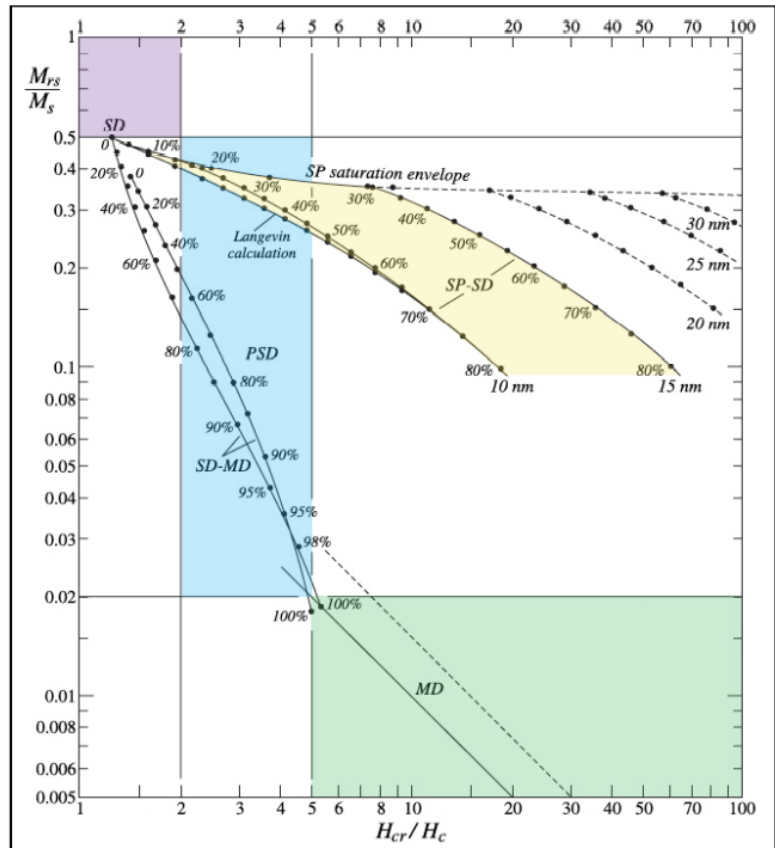
Figure 12: Theoretical Day plot curves for magnetite showing regional locations for domain states and domain state mixtures; purple (SD), blue (PSD), green (MD), yellow (SP-SD). Figure from *Dunlop, 2002*.

17

Magnetic Mineralogy

Magnetic mineralogy can sometimes be identified by the temperature at which a sample's behavior transitions from ferromagnetic to paramagnetic (Curie temperature, T_c) by measuring susceptibility as a function of temperature (*Hrouda, 1994*) (*Figure 13*). Above T_c, magnetic exchange energy (related to the passing of electrons between atoms) is exceeded by thermal

Figure 13: Curie temperature curves of sample EL5-3 (susceptibility as a product of temperature). The red line represents changes in susceptibility while heating, the blue line represents changes in susceptibility while cooling. This particular curve shows a Curie temperature of ~580°C, indicating that magnetite is the dominant source of magnetism in this sample.
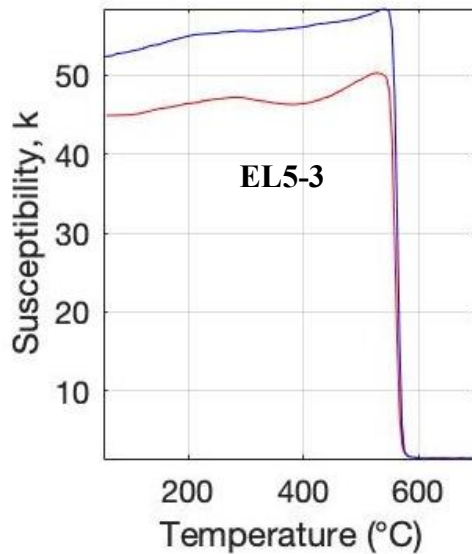
energy, resulting in thermal demagnetization of the ferromagnetic magnetization (*Tarling and Hrouda, 1993*). Compositionally dependent, T_c can be used to infer dominant mineralogy responsible for a sample's magnetism. Magnetite can also be identified at low temperatures by a dramatic changes in magnetism at T=120K (Verwey Transition), undergoing reversible transformations in magnetic properties, lattice structure, and electrical conductivity (*García and Subías, 2004*).

Magnetic Anisotropy

The minimization of energy within a magnetic particle leads to anisotropy in magnetization at the grain (or crystal) level. Certain directions of magnetization are at lower energy than others, resulting in an "easy axis" of magnetization. This preferred direction of magnetization is influenced by either the crystal lattice or crystal shape. Magnetocrystalline anisotropy results from lattice forces acting on electron spin configurations, resulting in magnetization along a specific crystallographic axis or plane (*Tarling and Hrouda, 1993*). Shape anisotropy arises from the interaction between magnetization and an internal demagnetizing field. This interaction results from the alignment of poles (surface charges) at opposite ends of each grain (*Butler, 1992*). In shape anisotropy, the preferred magnetization is normally oriented along the long axis of the grain to minimize its total energy. Both magnetocrystaline anisotropy and shape anisotropy are dependent upon a material's magnetic mineralogy and grain size. For most naturally occurring minerals, shape anisotropy controls the magnetization direction, which means magnetic measurements can be useful in quantifying deformation features in rocks (petrofabrics) (*Potter and Stephenson, 1988*).

So long as the physical orientation of the magnetic grains does not change after deposition, AMS fabric is unaffected by later changes in the remanent magnetization (remagnetization). If diagenesis is accompanied by the formation of new magnetic minerals, the fabric could be altered. However, any diagenetic minerals growing in or around pre-existing particles are likely to inherit the anisotropy of the depositional fabric.

At the grain or the rock scale, AMS is geometrically represented by a susceptibility ellipsoid with three principal axes: k_1(max), k_2, k_3(min) (*Figure 14a*), which describe the orientation of the eigenvectors of the susceptibility tensor. Additionally, each of these eigenvectors has an eigenvalue (τ_1, τ_2, and τ_3 respectively) which are used to describe magnitude of the susceptibility axis and indicate shape of the ellipsoid (oblate, prolate, and triaxial). Directions of these principal axes are plotted on a lower hemisphere equal area (LHEA) stereonet projection (*Figure 15*).
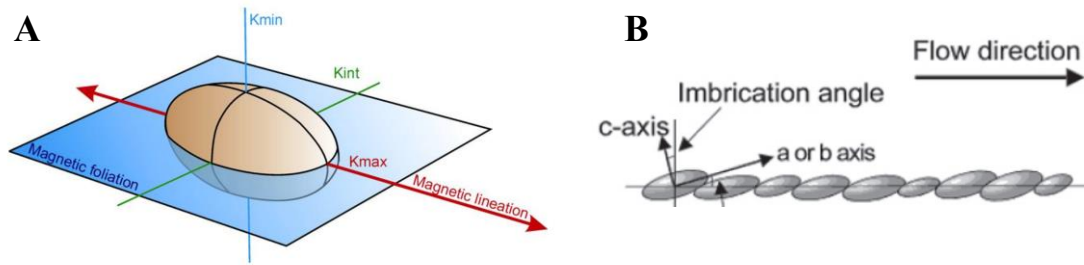
Figure 14:
A) Model of a magnetic susceptibility ellipsoid displaying three perpendicular axes (eigenvectors) *(Chadima 2021)*.
B) Imbrication of susceptibility ellipsoids as a result of fluid flow *(Hailwood & Ding 2000)*.
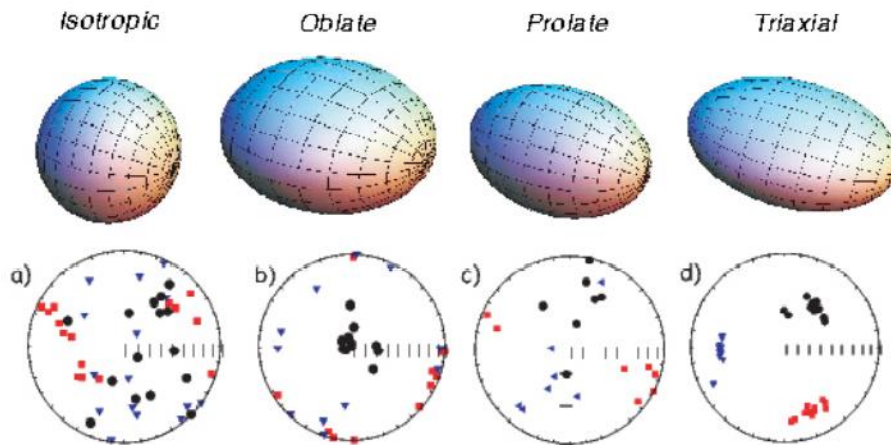
Figure 15:. (a-d) Example datasets, plotted as eigenvector directions from individual specimens.
Figure modified after *Tauxe et al., 2018.*

AMS has been used in several studies regarding glaciogenic and geomorphologic features to infer the directional force applied to those sediments by observing the orientation of silt-sized magnetic particles within the deposits (*Hooyer et al., 2008; Ives and Iverson, 2019*). In this way, AMS can be an indicator of sedimentary transport direction (*Figure 14b*). There are four primary fabric patterns associated with different depositional processes: (1) horizontal fabric, (2) flow-aligned fabric, (3) flow-transverse fabric, (4) flow-oblique fabric (*Figure 16*) (*Baas et al., 2011*). Flow-aligned and flow-transverse fabrics are common in subaqueous debris flows, but flow-oblique fabrics have also been observed (*Rees, 1983*).

When grains are deposited in a low energy environment and fall through a still column of water (or air), the dominant influence on particle orientation is gravity. If the surface of deposition is horizontal, the long (k1) and intermediate (k2) grain axes will be almost parallel to the plane, and the short axes (k3) perpendicular (Figure 16a). Common in lacustrine and marine environments, this 'horizontal fabric' is characterized by a weak foliation. In a glaciolacustrine or glaciomarine environment, sand- to boulder-sized clasts that bend or penetrate sedimentary layers may accompany horizontal magnetic fabrics, suggesting deposition by rainout of ice-rafted debris.

Experimental observations by Rees (1983) demonstrate that in low to medium velocity flows or flows with sediment concentrations <1.2% (low viscosity) and >11.1% (high viscosity) by volume, alignment of long axes was parallel to flow. Grains tend to imbricate up-current with their long axes parallel to flow (Figure 11b) resulting in a tight cluster of k3 slightly off from

vertical (10-30°), with a cluster of k1 dipping slightly from the bedding plane on an equal-area stereonet. This 'flow-aligned fabric' is usually accompanied by a lineation (Figure 16b) and flow direction is indicated by imbrication of k3 eigenvectors deflected from vertical.

Grains transported by high velocity or mid-viscosity flows (sediment concentration between 1.2% and 11.1% by volume; *Rees, 1983*) align with their long axes perpendicular to flow and often are present in the turbulent upper portion of a bipartite flow that experiences deposition at high-flow regime. The result is a split cluster of k_1 along the bedding plane, and a tight cluster of k_3 imbricated up to 30° from vertical. This '*flow-transverse fabric*' is commonly referred to as a '*rolling fabric*' (*Figure 16c*) and flow direction is indicated by the imbrication of k_3 eigenvectors deflected from vertical.

Figure 16: Four primary depositional fabric patterns in lower hemisphere equal area stereonet projection. Imbricated subtypes shown in (b), (c) and (d). Horizontal fabric (a) is non-imbricated by definition. Black arrows in drawings and stereograms denote flow direction. Figure used from *Amato, 2017*, modified from *Baas et al., 2007*.

Baas et al. (2007) define a *flow-oblique fabric* as when the k_1 axes are oriented at a significant angle to the main flow direction. Causes for flow-oblique fabrics have been attributed to clast interactions in viscous flows, spatial changes in

current direction, changes in flow regime, changes in substrate roughness, and soft sediment deformation (*Baas et al., 2007*). For the purpose of this study, a flow-oblique fabric is defined as when the k_1 and k_2 axes are oriented at ~45° from the direction in which the k_3 is deflected from vertical (*Figure 16d; Amato, 2017*) and is a strong indicator of debris flow deposits involving clast interactions. It should be noted that grain imbrication may or may not develop in flow-aligned, flow-transverse, and flow-oblique fabrics. Why imbrication may not occur has not been thoroughly explored, but suggested causes include sudden changes in flow regimes, and compaction (*Amato, 2017*). The capability of AMS to indicate transport direction is fully reliant on the presence of imbricated grains. However, field observations are also important in identifying flows, especially if there are deposits in adjacent layers that can suggest true directions (rippled sands).

To aid in distinguishing between a diamictite produced from SGFs and one produced subglacially it may be helpful to examine a rock's magnetic fabric. It is generally agreed that the long axes of clasts in till are statistically aligned parallel to the direction of ice movement. Consequently, it would be expected that the long axes of the magnetic particles would also be aligned parallel to the direction of ice flow (*Figure 17*). However, differentiating between flow-aligned fabrics produced subglacially and those produced by other means require field observations such as glacial striations and facetted clasts to make a sound interpretation of depositional process (*Embleton and King, 1975; Gravenor et al., 1973*). True tills show signs of shear and tend to produce triaxial magnetic fabrics at shear strains > 25 (*Hooyer et al., 2008*) with orientations of k_1 and k_3 susceptibility axes in the longitudinal flow plane and azimuths parallel to shear: k_1 oriented up-flow and k_3 oriented down-flow (*Ives and Iverson, 2019; Figure*

16; Flow aligned fabric). Diamictites that have experienced less shear strain may display k_1 distributed along great circles (girdles) symmetrically disposed about orientations of k_3 clusters (*Gentoso et al., 2012*; *Hopkins et al., 2016*; *Ives and Iverson, 2019*). AMS fabrics infer sedimentary transport direction by clustering of the k_3 axes (k_3 axes cluster parallel to shear) and shed light on the amount of shear strain experienced during deposition. Because mass-transport and SGF deposits may undergo substantial shearing at their bases during transport, stratigraphic context and field observations are necessary in differentiating between subglacial shearing and shearing at the base of a SGF or mass-transport deposit. In tills, shear strain increases toward the former ice-substrate interface from below whereas mass-transport or SGF deposits show a decrease in shear strain above and away from the shear plane.
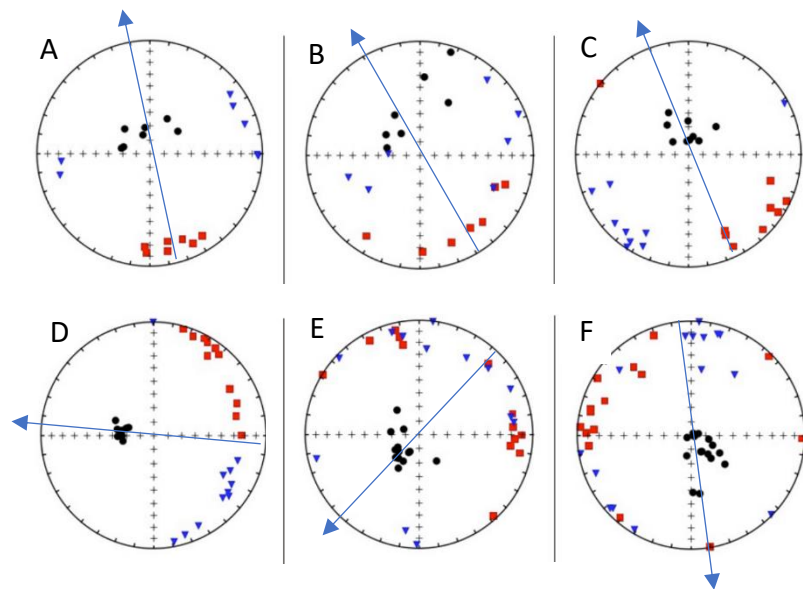
Figure 17: A, B, C: Examples of flow aligned fabrics produced subglacially.
D: Flow oblique fabric generated by sedimentary mass transport.
E, F: Examples of flow transverse-flow fabrics produced by sedimentary mass transport. (Data from *Amato, 2017*).

Procedures

Field Procedures and Sampling

This project investigates ten outcrops of the Gowganda Formation exposed 4 to 11 km north of Elliot Lake, Ontario Canada along highway 108 (46°25'17.7"N 82°40'13.2"W to 46°27'56.7"N 82°38'32.7"W) (*Figure 2*) using typical sedimentological surveying methods. Sedimentary units were photographed, measured in thickness using a Jacob's staff and classified according to lithology. Clast shape, size, lithology, and abundance were noted along with grain size, bedding contacts, bed geometries, and sedimentary structures and drafted in stratigraphic columns to record field observations. Dip and dip direction were recorded from measurable bedding surfaces for regional dip as well as the orientation of cross stratification as an indicator of paleocurrent directions. Blocks of lithified Gowganda (here-on referred to as sites) were selected and sampled in the field using a rock hammer based on observed features and high matrix content, oriented, and labeled in the field using a north arrow, up arrow, strike, and dip and transported to the University of Wisconsin – Milwaukee (UWM) for paleomagnetic core sampling.

All 10 outcrops sit in the Sudbury syncline which trends and plunges west and are named in order from oldest (EL1 on the south side of the syncline to youngest (EL10) near the middle. It is reasonable to believe that tectonism occurred post-deposition, however no major folds were observed. Sites were collected over two field sessions. Sites collected during session one were labeled in the fashion: EL#-# which indicates the Elliot Lake area (EL), the outcrop number (EL#) and the site number (EL#-#). Sites collected during the second field session were labeled similarly and marked with a '*' to indicate that it was collected during the second field session (e.g., *EL#-#).

25

Three to four cores (samples) were extracted from each site using a drill press with a 1" diameter diamond drill core bit. Because clasts have their own magnetic fabrics and thus do not represent fabrics produced through sedimentary deposition, care was taken to avoid any large clasts while drilling. Cores were oriented by first reorienting the site in a sandbox, then orienting the sample using a Pomeroy orienting device and Brunton compass. Once oriented, each sample was cut in half, separating each sample into two specimens to contrast a weathered and non-weathered surface. AMS for each specimen was measured at the UWM Department of Geosciences using a AGICO Geophysika MFK1- FA Multifuction Kappabridge in a 976 *Hz* applied field at room temperature with a 200 *Am^{-1}* peak intensity. Susceptibility data are collected as the sample is rotated about three orthogonal axes using the MFK1-A's spinning specimen method outlined in *Jelinek* (*1997*). Data are then processed and plotted via Anisoft software by AGICO that plots eigenvector data for each specimen in a site on a lower-hemisphere equal-area stereonet. Data are then corrected to compensate for regional tilt and magnetic declination.

To understand domain-state of magnetic particles present in the specimens, magnetic hysteresis measurements were collected using a Lakeshore 8600 Series VSM located at the Institute for Rock Magnetism (IRM), University of Minnesota - Twin Cities. Magnetism was measured at room temperature in a field of -1T to 1T, producing hysteresis loops to analyze coercivity and saturation magnetism for each specimen. A Day Plot was generated, plotting M_r/M_s over B_{cr}/B_c, to estimate average magnetic domain state and trends in coercivity.

To infer dominant magnetic mineralogy, two specimens were selected based on hysteresis data, as endmembers for low temperature analysis (one that expressed high coercivity and one that expressed low coercivity) using a Magnetic Property Measurement System (MPMS) Superconducting QUantum Interference Device (SQUID) magnetometer at the IRM. Two experiments were performed to identify the magnetite Verwey transition or other composition-specific low-temperature behavior. In the first experiment, the sample is given a room-temperature (saturation) isothermal remanent magnetization (RTSIRM) in a 2.5T applied field. This magnetization is then measured as a function of temperature while cooling from 300K to 10K then warmed back up to 300K. In the second experiment (the so-called field-cooled/zero-field cooled experiment), the sample is cooled from room temperature to 10K in the presence of a large (2.5 T) field (field-cooled, FC). At 10K, the field is turned off and the remanent magnetization is measured on warming back to room temperature. The sample is then cooled back to 10 K in zero field (zero-field cooled, ZFC). At 10K, the sample is briefly exposed to a 2.5T field, and the resulting magnetization is then measured on warming back to room temperature.

Additional compositional information was gleaned from Curie temperature (T_c) data, collected at UWM using a CS4 furnace attachment for the Kappabridge and the Sufyte5W thermomagnetic curve control software (*AGICO, 2011b*; *Amato, 2017*). Pulverized samples were heated under Ar atmosphere from room temperature to 700°C and then cooled while continuously measuring susceptibility. A full background correction was performed by measuring the empty furnace from room-temperature to 700°C and subtracting the results from the sample data.

Six sample sites were selected for microsedimentary analysis based on observations of magnetic fabric. Three sites that produced subvertical magnetic fabrics (EL6-1, EL7-2, & *EL9-1) and three sites that produced subhorizontal magnetic fabrics (EL4-3, *EL8, & *EL10-1) were cut, examined under petrographic microscope, and photographed for examination of microsedimentary structures. Magnetic data will supplement microsedimentary and field observations to aid in the interpretation of sedimentary deposition type and transport direction.

Observations

The Gowganda Formation in the area north of Elliot Lake measures approximately 760m in thickness from the base of outcrop EL1 to the top of outcrop EL10 (*Figure 18*). EL1 sits on the southern edge of the Sudbury Syncline which trends northeast to southwest with EL10 near its center, representing what is interpreted here as the last sedimentary unit of the

Figure 18: Complete stratigraphy showing full thickness of the Gowganda Formation in the area north of Elliot Lake, Ontario including site locations.

28
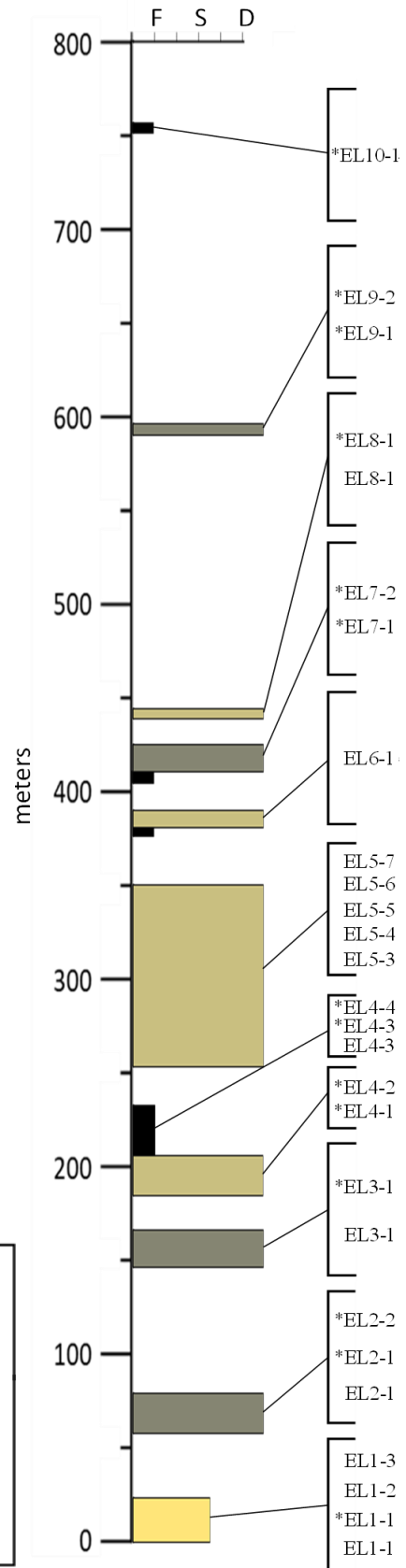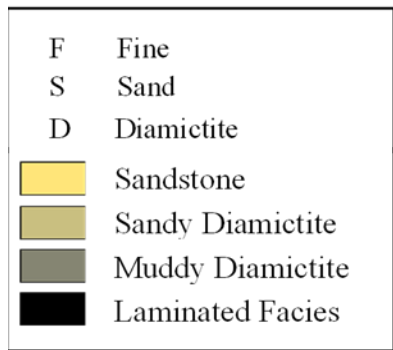
Gowganda in this area. Thickness was calculated using the dip of bedding which decreases from ~15° in outcrops EL1-EL6 to ~5° in EL7-EL10. Diabase dykes are present in EL2 and EL5 (*Figure 19*), and gaps in the stratigraphy are due to erosion by more contemporary river channels. The formation is dominated by sandy and muddy Dsm and Dmm facies but also includes four sections of thinly laminated fines with dropstones (except EL10) and one outcrop dominated by cross-laminated sandstones (EL1).

<u>*Facies Descriptions*</u>

At its base, the Gowganda contains an erosional contact with carbonates of the Paleoproterozoic Espanola Formation, with the Serpent Formation completely missing in this area (*Figure 1*) (*Young, 1991*). Diamictite facies are dominant throughout the Gowganda although laminated and sandstone facies also occur (*Figure 19, Table 1*). Angular to rounded outsized clasts (< 2 m diameter) are common throughout, composed of igneous (> 70% felsic and 15% mafic), metamorphic (10%), and sedimentary (< 5%) rock. All three facies types (diamictite, sandstone, laminated) can be further broken down and are discussed in this section using classification codes outlined by Benn and Evans (2010) (*Table 1*; *Table 2*).

Diamictite Facies

Description: Diamictite facies can be observed in three broad categories: muddy, sandy and clast supported (*Benn and Evans, 2010; Figure 19*). Muddy diamictites (EL2, EL3, EL7, EL9; *Figure 19; Figure 20A*) are meters to 10s of meters thick, massive, matrix supported (Dmm), and clast-poor, except EL9 which contains faint pebble horizons, bordering on sandy matrix-supported and stratified (Dms). Clasts throughout the muddy Dmm facies display faint rotational structures and

no apparent preferred orientation (*Figure 22*). Sub-vertical clastic dykes are found in most Dmm

facies and are ubiquitous in EL7, along with sub-vertical water-escape pipes visible only under

petrographic microscope. Deformed rafts of coarse sands, sometimes containing their original

sedimentary structures also make EL7 unique, as they are typically found in sandy Dmm facies

(EL4, EL5, EL7, EL8, EL9) (*Figure 19; Figure 22*).

Diamictite Sub-facies Classification Codes

<u>Code</u>	<u>Discription</u>
Dmm	Matrix-supported massive
Dms	Matrix-supported stratified
Dcm	Clast-supported massive
Dcs	Clast-supported stratified

Table 1: Facies classification and codes, modified from *Ben and Evans 2010*.
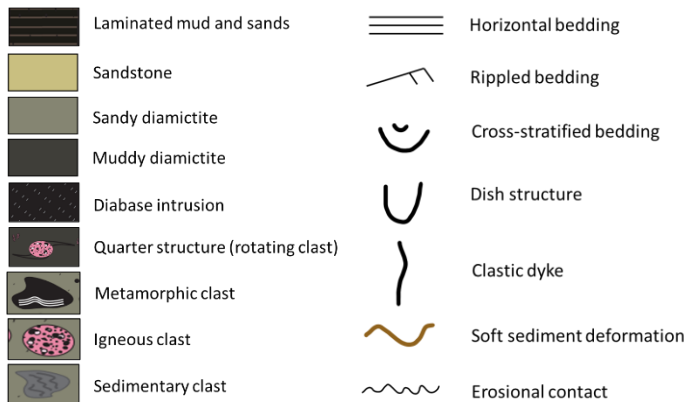
Figure 19: Left) symbol key for stratigraphic columns.
Pg 31, 32, 33) Stratigraphic columns of the Gowganda FM, north of Elliot Lake, Ontario Canada.
All outcrops were measured in meters and include grain-sizes very fine (VF), fine (F), medium (M), coarse (C), granule (G), and diamictite (D) from smallest to largest with D representing a mixer of all grain-sizes. For outcrop locations see Figure 2.

EL 5

EL 6
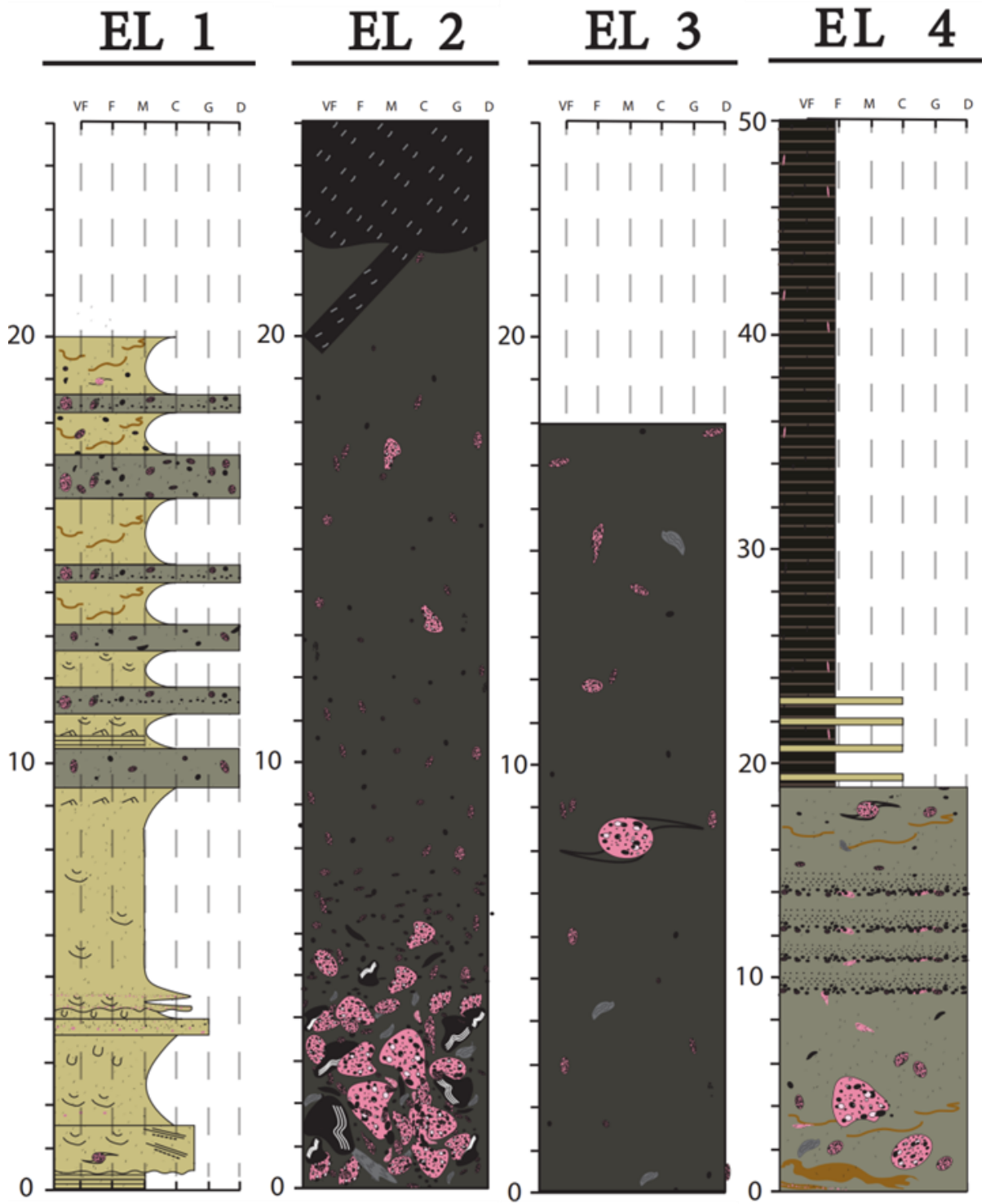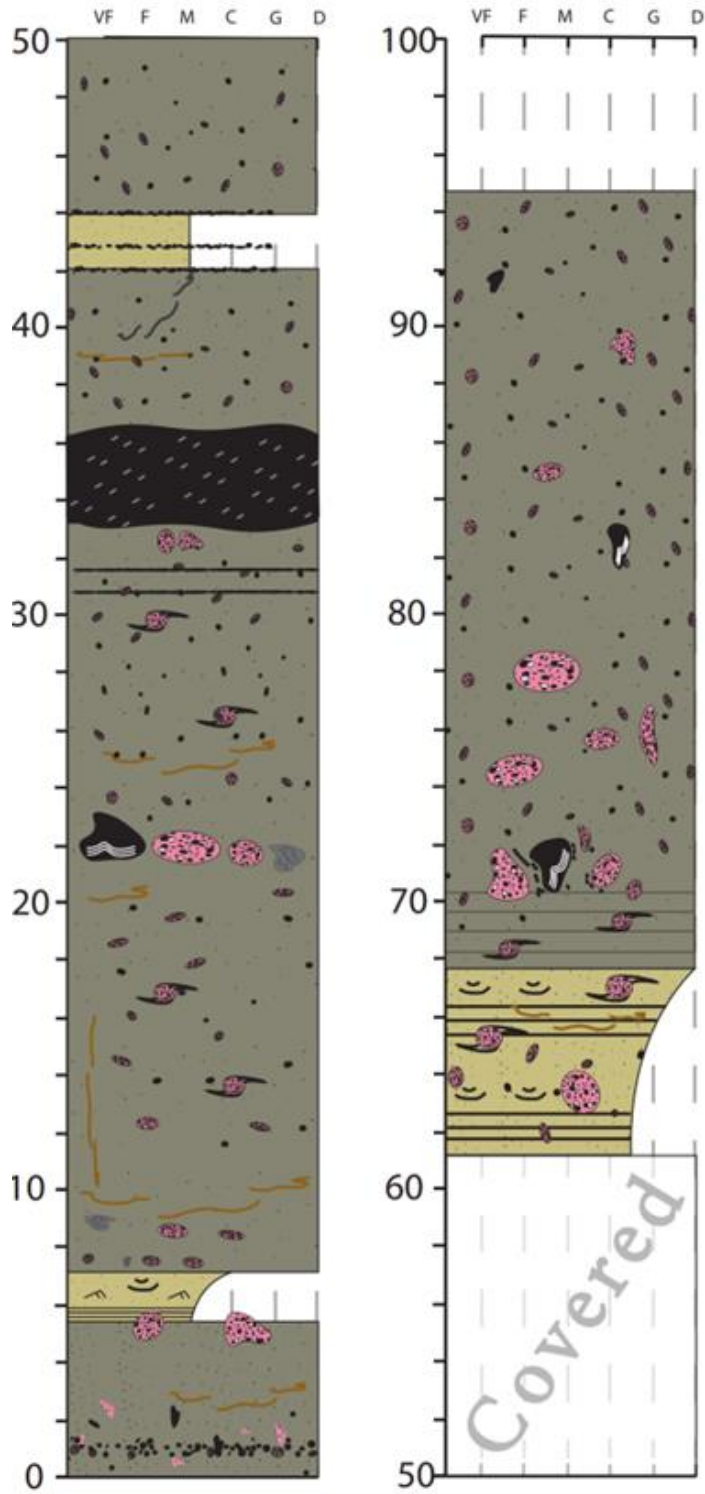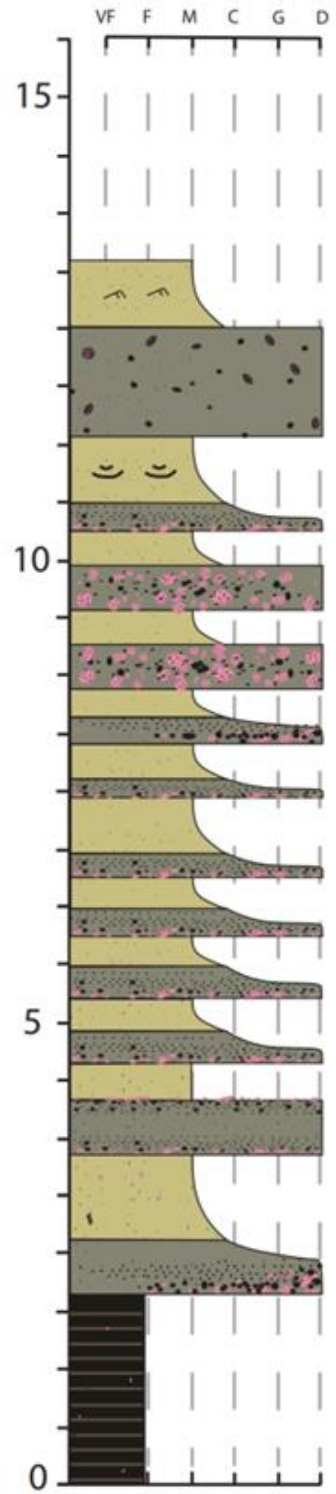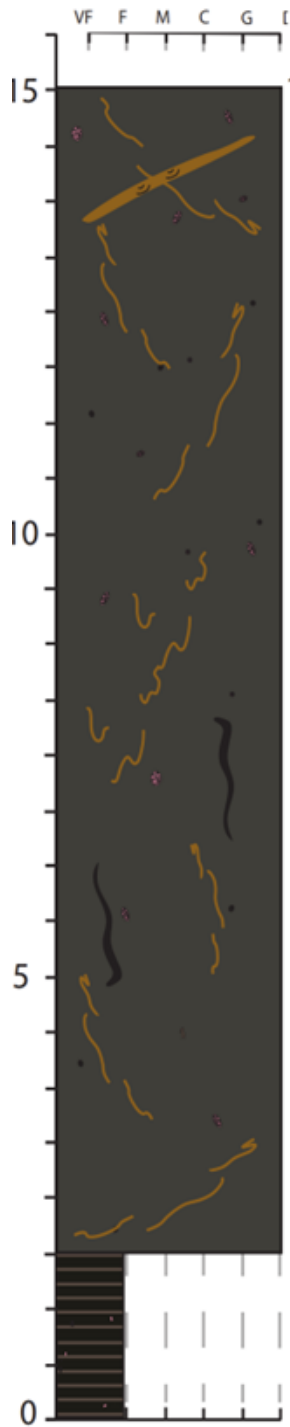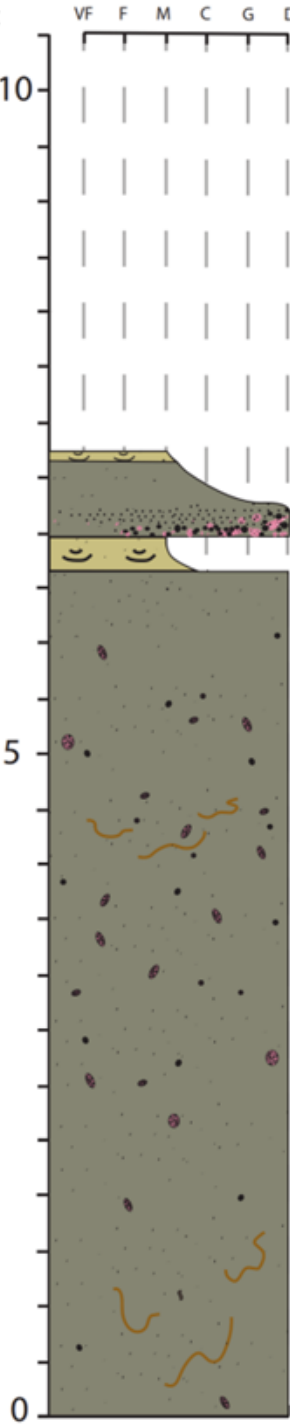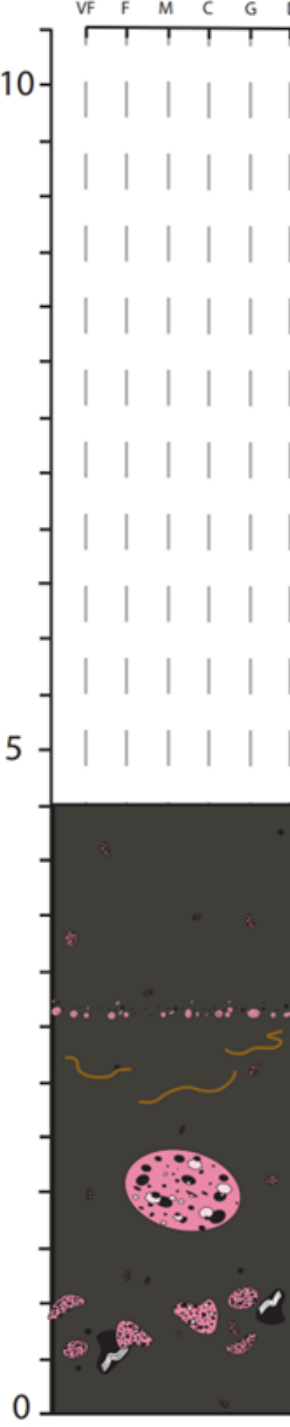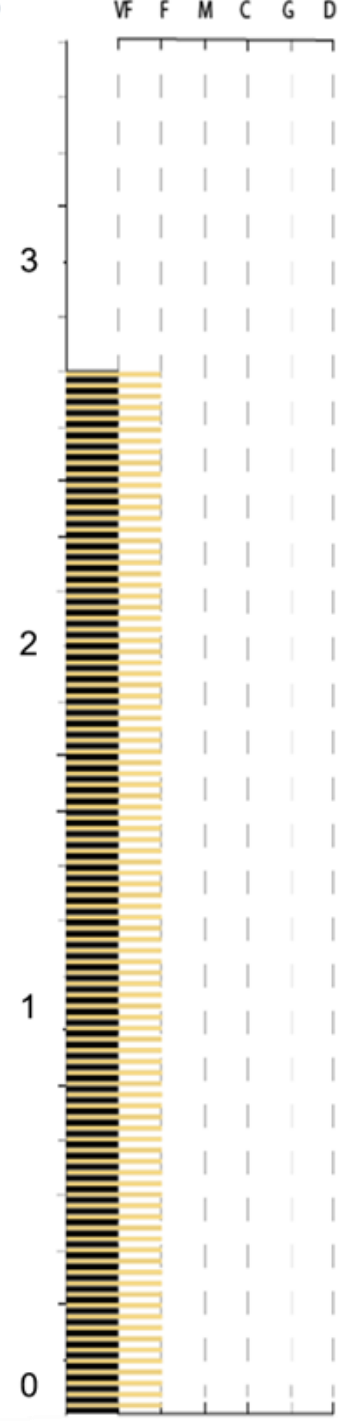
Outcrop	Location	Outcrop Description	Sites	Magnetic Fabrics	Flow Type (Flow genetics)
EL1	N46° 09.780' W082° 04.769'	Medium-course, horizontal-cross-laminated sandstone with sections containing deformed bedding and water escape structures, interlayered with clast-poor-intermediate sandy Dsm facies with erosional base contacts.	EL1-3 Dsm EL1-2 Sandstone *EL1-1 Sandstone	Triaxial-oblate, sub-horizontal - sub-vertical, flow transverse-oblique	Inflated sand flow layered with more cohesive debris flow.
EL2	N46° 25.010' W082° 40.252'	Clast-poor-intermediate muddy Dmm facies with Dcm facies at its base.	*EL2-2 Dmm EL2-1 Dmm *EL2-1 Dmm	Triaxial-oblate, sub-horizontal, flow transverse.	Thick cohesive debris flow (Dmm) and possible ice-rafted dump (Dcm).
EL3	N46° 25.230' W082° 40.241'	Clast-poor-intermediate muddy Dmm facies.	*EL3-1 Dmm EL3-1 Dmm	Triaxial-oblate, sub-horizontal, flow transverse.	Thick cohesive debris flow.
EL4	N46° 25.272' W082° 40.244'	Sandy Dmm-Dsm with visible clast pavements and possible shear zones below a thick sections of thinly-bedded marine turbidite deposits.	*EL4-4 Turbidites *EL4-3 Turbidites *EL4-2 Dsm *EL4-1 Dsm	Triaxial-oblate, sub-horizontal - sub-vertical, flow transverse (Dsm); triaxial, horizontal-sub-horizontal (turbidites).	Debris flow, less cohesive than Dmm facies below a series of concentrated density flows and low-density turbulent flows.
EL5	N46° 25.532' W082° 40.170'	Sandy Dsm-Dmm containing clast and boulder pavements and possible shear zones layered with medium-course, reverse graded sandstone.	EL5-7 Dsm EL5-6 Sandstone EL5-5 Dsm EL5-4 Dsm EL5-3 Dsm	Triaxial-oblate, sub-horizontal, flow transverse-oblique.	Debris flow (EL5-3, EL5-4, EL5-6, EL5-7). Glacial till (EL5-5).

Outcrop name	Latitude/Longitude	Outcrop description	Site names	Magnetic fabric	Flow type interpretation
EL6	N46° 25.800' W082° 40.065'	Thinly-bedded turbidite deposits below a series of alternating Dcm/Dmm (laterally discontinuous) and massive-horizontal-cross-laminated, normally graded, medium-course sandstone facies.	EL6-1 Sandstone	Triaxial, sub-vertical.	Concentrated density flows and turbidity flows below bipartite inflated grain flows (Dcm/Dcs, and sandy facies).
EL7	N46° 25.996' W082° 40.042'	Thinly-bedded turbidite deposits with granule-sized clasts below muddy Dmm facies.	*EL7-2 Dmm *EL7-1 Dmm	Triaxial, sub-vertical.	Concentrated density flows and turbidity flows below a thick cohesive low-density (turbidity) flow.
EL8	N46° 26.188' W082° 40.057'	Sandy Dmm-Dsm with rippled-horizontal-cross-laminated medium-course normally graded sandstone.	EL8-1 Dsm *EL8-1 Dsm	Oblate, sub-horizontal - sub-vertical, flow transverse-oblique.	Debris flows, less cohesive than Dmm facies.
EL9	N46° 27.178' W082° 39.874'	Muddy-sandy Dmm-Dsm facies exhibiting deformed rafts of course red sands, granule horizons/clast pavements, and a boulder ~ 2 m diameter.	*EL9-1 Dsm *EL9-2 Dsm	Oblate, sub-horizontal - sub-vertical, flow transverse-oblique.	Debris flows, more cohesive than EL8 but less cohesive than Dmm facies.
EL10	N46° 27.950' W082° 38.710'	Series of thinly-bedded turbidite deposits depicting layers of massive-cross-laminated very-fine sands alternating with mud.	*EL10-1 Turbidites	Triaxial, horizontal	Concentrated density flows and turbidity flows.

Table 2: Outcrop name, Latitude/Longitude, Outcrop description, Site names and descriptions, Magnetic fabric, Flow type interpretation.

Thinner than muddy diamictites, sandy diamictites in the Gowganda are decimeters to meters thick. Most are matrix supported and stratified (Dms), containing granule to boulder-sized clast horizons, although massive (sandy Dmm) sections are present between some sandy Dms facies. Unlike outcrops with muddy Dmm facies, massive, reverse, or normal graded sandstones accompany sandy Dms facies (EL1, EL4, EL5, EL6, EL8; *Figure 19; Figure 20B,C*). Dms facies themselves typically show normal grading and deformation structures (quarter structures, sand wisps/rafts) that are more pronounced compared to muddy Dmm facies and present sub-horizontal orientation. Of the outcrops that include sandy Dms facies, EL5 shows particularly interesting characteristics. Generally composed of sandy Dmm facies, EL5 depicts layers of clast-rich Dms, one that includes a bed of striated boulders with their apparent long axes aligned (*Figure 19; Figure 23*).

Clast-supported diamictites, both massive (Dcm) and stratified (Dcs), are present in outcrop EL8 and dominant throughout EL6 (*Figure 19; Figure 24*). Most are stratified (Dcs) and show normal or reverse grading, typically scouring underlying sand. Normally graded Dcs facies, decrease sands, although some sands in EL6 are massive. Shear planes are often visible at the base of reverse graded Dcs facies while overlying sand is draped over boulders protruding from its top. Some are discontinuous (EL6, EL8), laterally transitioning from Dcs to Dmm from north-east to south-west respectively.

Figure 20 (next page): Diamictite Facies: A) Muddy Dmm with granule – cobble clasts (EL2) ; C) Sandy Dmm with subvertical whisps of fine sand (EL5); E) Sandy Dsm with normal graded subhorizontal bedding(EL5); G) Dcm showing reverse grading then normal grading between coarse sands, layers of which are massive, normally graded, or reverse graded. (EL6). B, D, F, H) highlighted features of photos from left. Meter stick and Jacobs staff for scale.
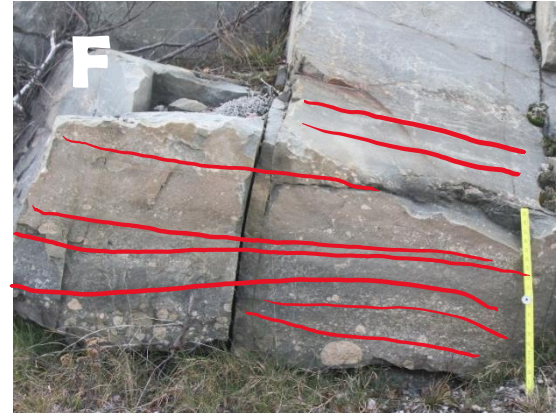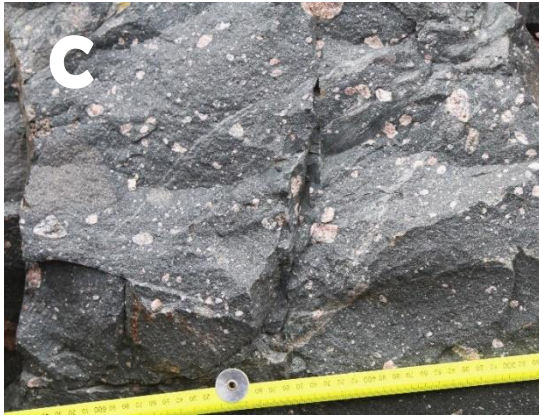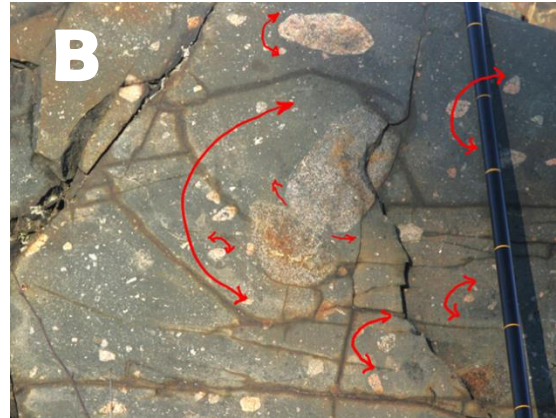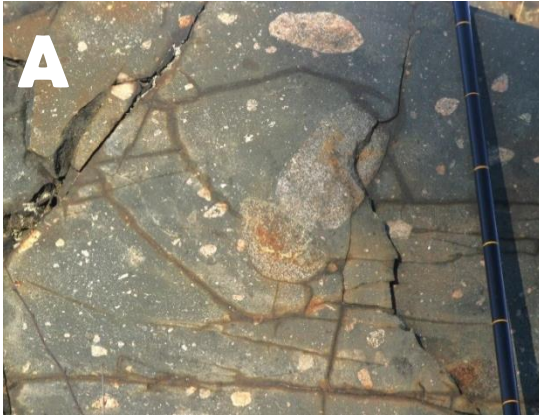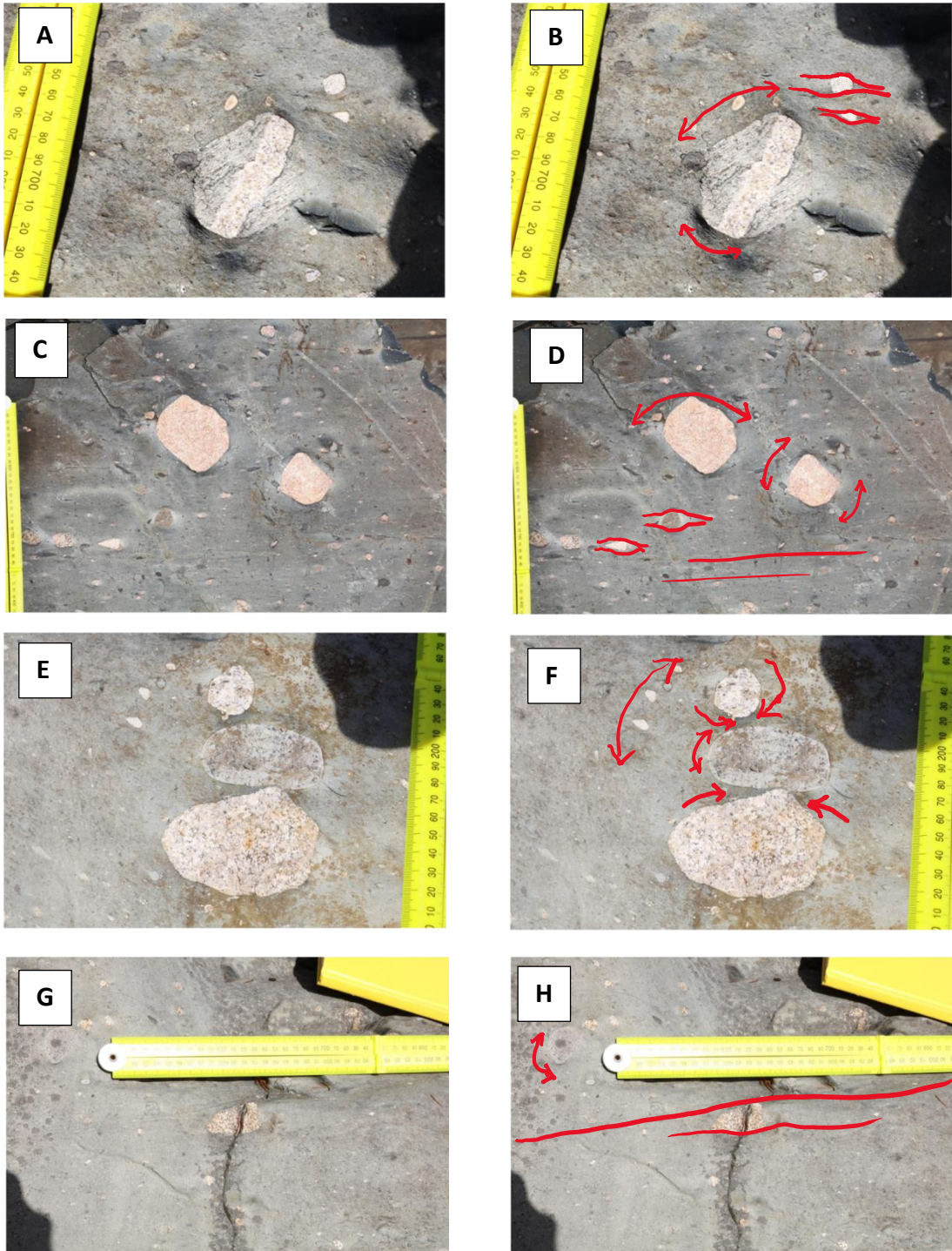
Figure 21: Evidence of clast rotation in a clast-poor, massive, muddy diamictite. A) Gneiss coble with smaller granite clasts circling around it. C) eye-shaped deformation of sediment around clasts (quarter structures). E) squeezing of saturated sediment between clasts (necking) and small clasts aligned and circling stacked cobles. G) Quarter structure around granite pebble. B, D, F, H) Highlighted features from photos from the left. Meter stick for scale.
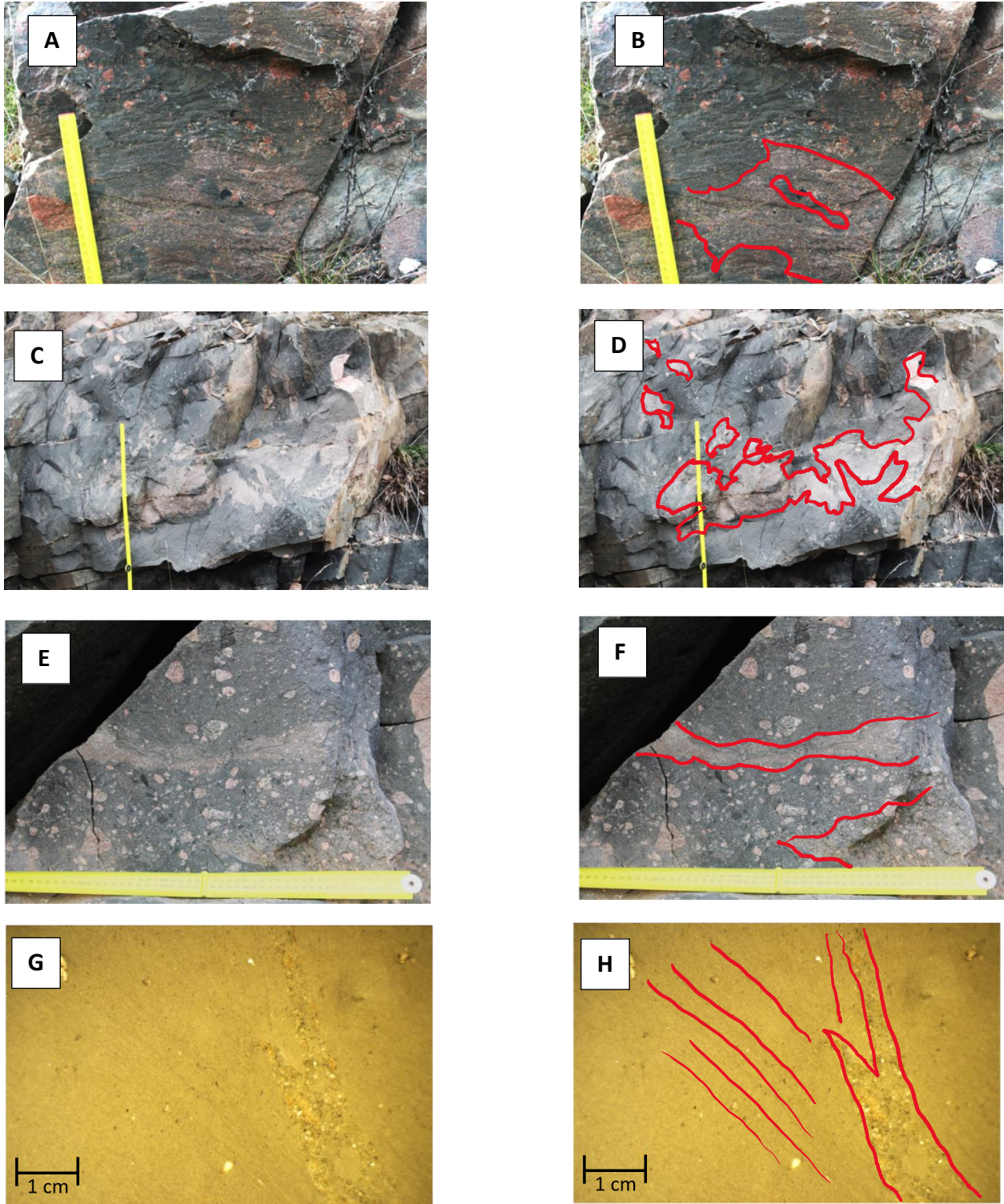
Figure 22: Deformed sands: A) EL4 coarse sand in slightly stratified, sandy diamictite., C)EL5 medium sand in massive sandy diamictite. E) EL7 Coarse sand in massive muddy diamictite. G) EL7 clastic dyke and water escape pipes in massive muddy diamictite. B, D, F, H, highlight features from photos on the left. Meter stick for scale except G and H.

Figure 23: Boulder beds at EL5. A) Outcrop-scale photo showing alignment of facetted boulders as well as sandy and muddy stratified diamictite. B) Boulder alignment at the base of EL5. C) Close-up of boulder alignment in photo A. D) Close-up of center boulder of photo C, facetted and striated with arrow indicating striation orientation. Meter stick for scale.

41
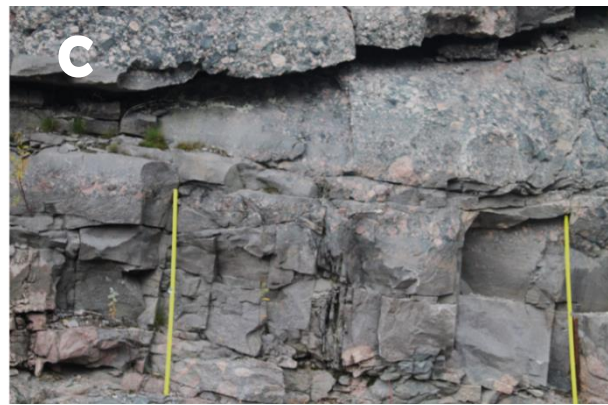
Figure 24 (previous page): Photos of EL6. A) Sandstones and coarse Dcs, reverse graded with larger clast protruding from the top of layer . C) Massive, reverse graded, and normal graded sandstones layered with Dcs that in parts has normal grading and reverse grading in others. E) Sharp contacts between Dcm and coarse massive-normal graded sandstones. G) reverse graded Dms at the base with hard contacts with massive – normal graded sandstone. B, D, F, H) highlight features from photos on the left. Scale: A = 2m thick , C = meter stick for scale. E= 1m thick, G = 2m thick.

Diamictite AMS description: Magnetic fabrics in both muddy and sandy Dmm facies are typically triaxial to oblate in shape, except for EL7-1 and EL5-3 which are triaxial-prolate. Of the muddy Dmm facies (EL2, EL3, EL7, EL9; *Figure 25*), sites EL2-1, *EL2-1 and EL3-1 show flow-oblique magnetic fabric whereas, *EL3-1, and *EL9-2 show flow-transverse fabrics. K_3 eigenvectors are well clustered between 50° and 70° dip in a southwesterly direction (azimuth 170° – 230°) and girdling of k_1 and k_2 axes is apparent to varying degrees in all Dmm facies except EL7. Deformed sands and signs of dewatering accompany vertical magnetic fabrics in both muddy and sandy Dmm facies.

Sandy Dmm facies (EL4, EL5, EL6, EL8) showed AMS fabrics similar to sandy Dms facies (EL1, EL4, EL5; *Figure 26*), containing triaxial to oblate shaped and flow-transverse to flow-oblique fabrics with clusters of k_3 axes between 20° and 50° dip southwest (azimuth 170° - 230°). Girdling of k_1 and k_2 axes is well-defined in most sites except *EL4-4 which demonstrates girdling of k_2 and k_3 axes and deformed wisps of sand.

Unfortunately, high clast concentrations prevented the acquisition of quality samples of diamictite matrix to be used in AMS analysis and field observations serve as the bulk evidence used in depositional interpretation of Dcm and Dcs facies (EL6).
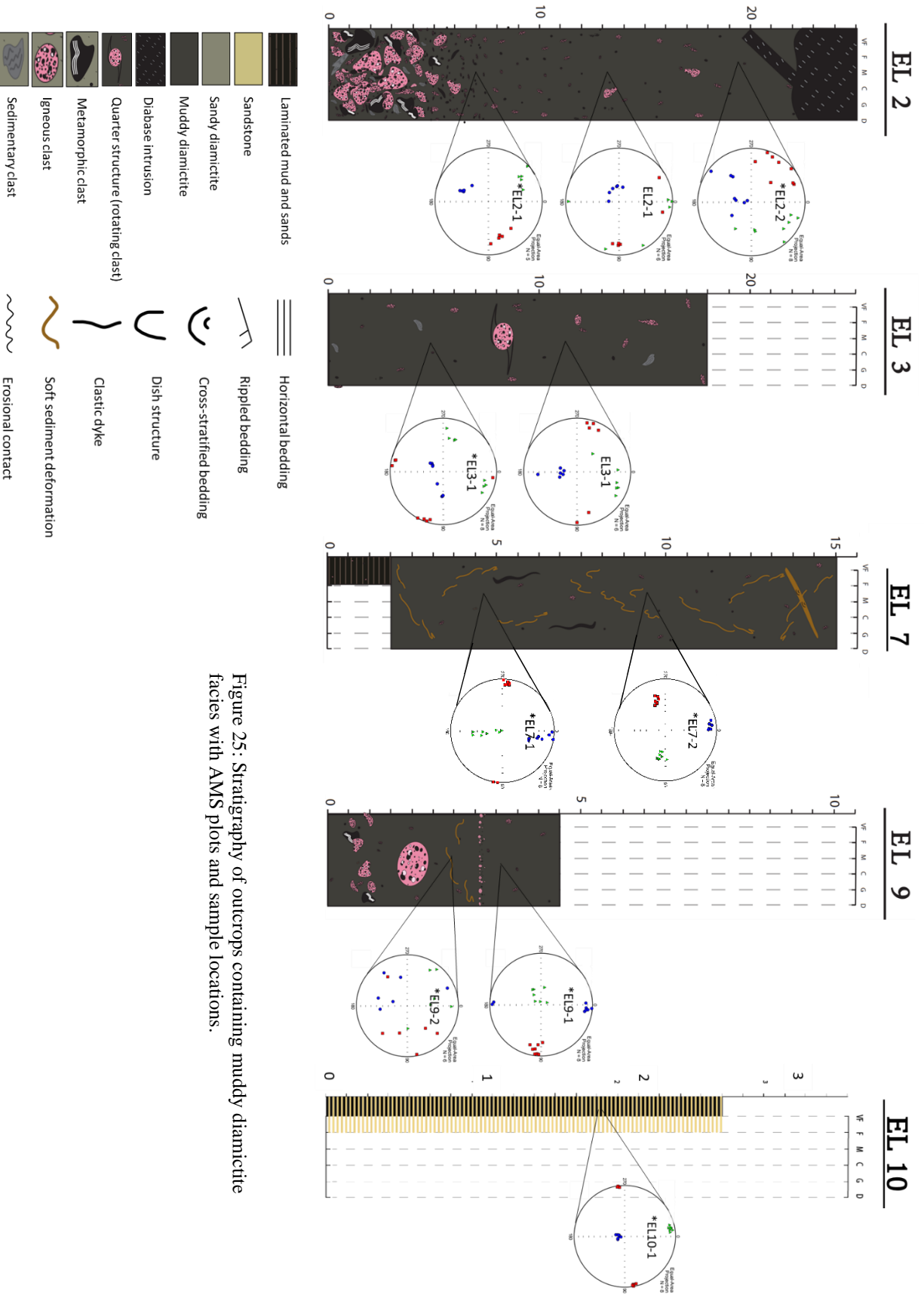
Figure 25: Stratigraphy of outcrops containing muddy diamictite facies with AMS plots and sample locations.

43
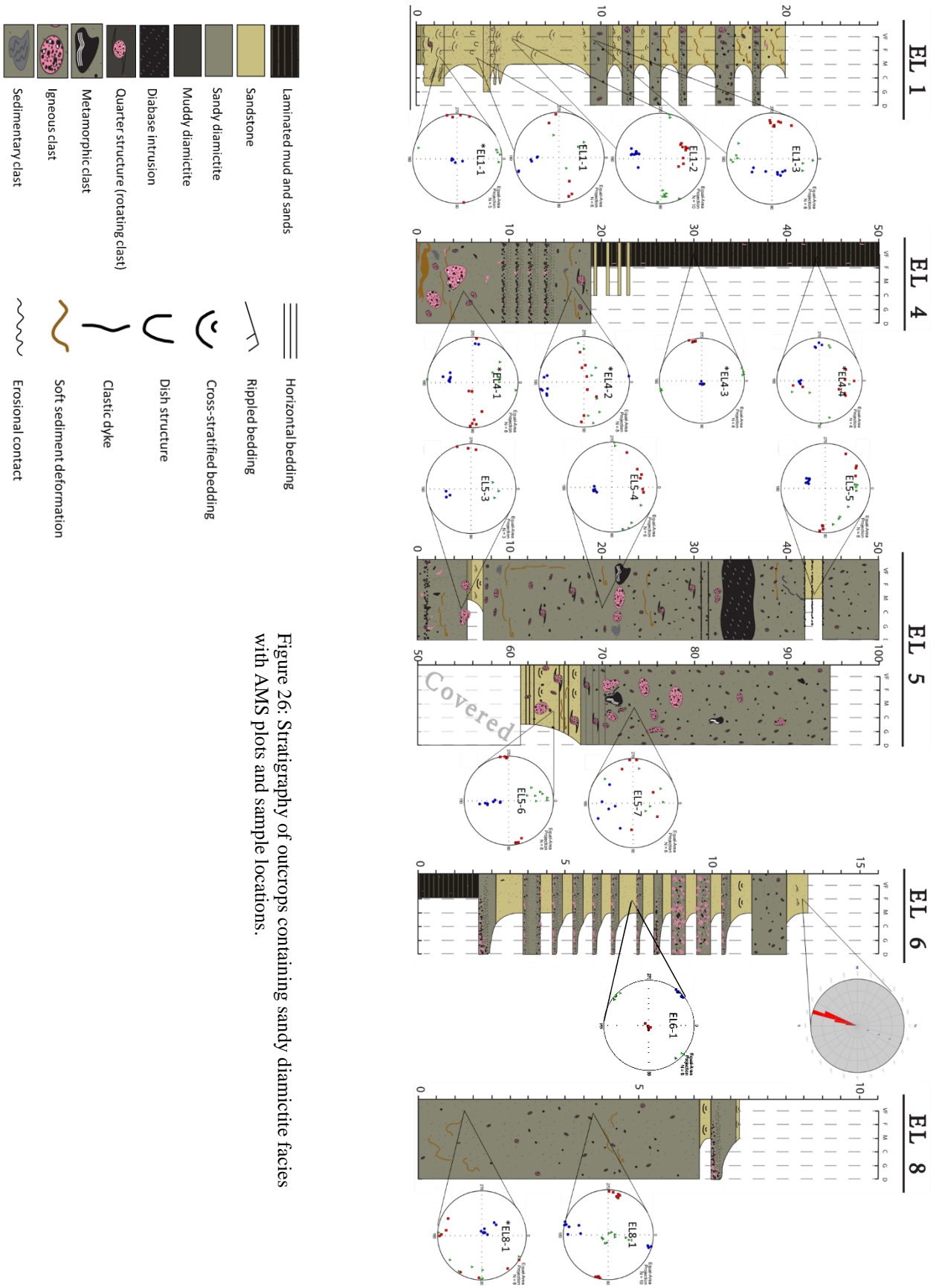
Figure 26: Stratigraphy of outcrops containing sandy diamictite facies with AMS plots and sample locations.

Sandstone Facies

Description: Two distinct types of sandstone facies occur throughout the Gowganda that can be distinguished by texture and color. Sandstones in EL1 are unique, displaying buff-grey color compared to the red-purple sands in the rest of the EL outcrops. The medium-coarse grained sand includes granule horizons, very sparse outsized clasts (cm scale), and abundant macro-scale dewatering (dish) structures (*Figure 27A*). Horizontal to cross-laminated bedforms range from undisturbed to totally deformed. Sandstone facies at EL1 can be massive or show normal or reverse grading, with sedimentary structures: trough crossbedding, and horizontal bedding).

Sandstone layers in EL5 (*Figure 27B*) are coarse, normal or reverse graded or massive, and are grey-purple in color. Horizontal to cross-laminated, they are reverse graded into sandy Dsm facies and include subangular to subrounded, centimeter-scale outsized clasts with quarter structures (*Figure 27*).

Sandstones in EL6 and EL8 are thin and resemble sands in EL5 in size and color. Massive or graded normally out of Dcs facies, they exhibit planer to cross-laminated bedforms and current ripples, and typically lack granule horizons and outsized clasts, compared to those in EL1 and EL5. Ripples from one sandstone layer in EL6 were oriented, suggesting a southwestern paleoflow direction (azimuth 195° – 205°)while another layer, observed at the outcrop to be massive, contained abundant centimeter-scale water-escape pipes and dish structures apparent only under petrographic microscope (*Figure 28*).

45
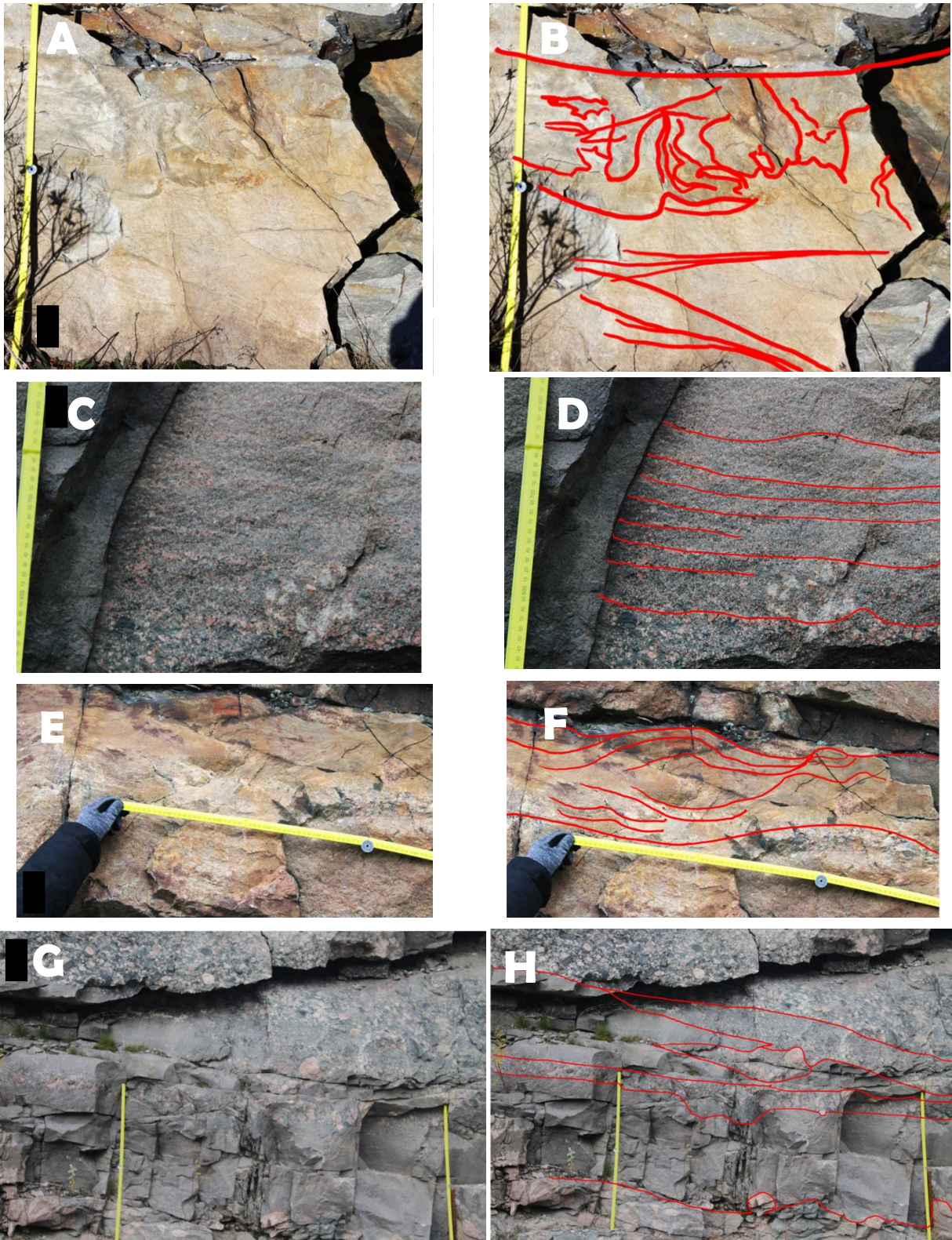
Figure 27: Sandstone facies: A) dewatering structures deforming horizontal-cross-laminated medium sand (EL1); C) Normal graded, granule-medium sand (EL5); E) Anti-dune preserved in thin sandstone layer (EL5), normally graded granule-medium sand; G) massive-normally graded course-medium sand layered with Dcm/Dcs facies (EL6). Highlights of features on the right. B, D, F, H) Highlight features from photos on the left. Meter stick for scale.

Unique to EL8, a slab of medium sandstone ~ 15 cm thick occurs stratigraphically between sandy Dmm facies (*Figure 29*). Laterally discontinuous, the slab of red sand appears in the outcrop to be massive, although AMS data suggests otherwise (interpretation below).
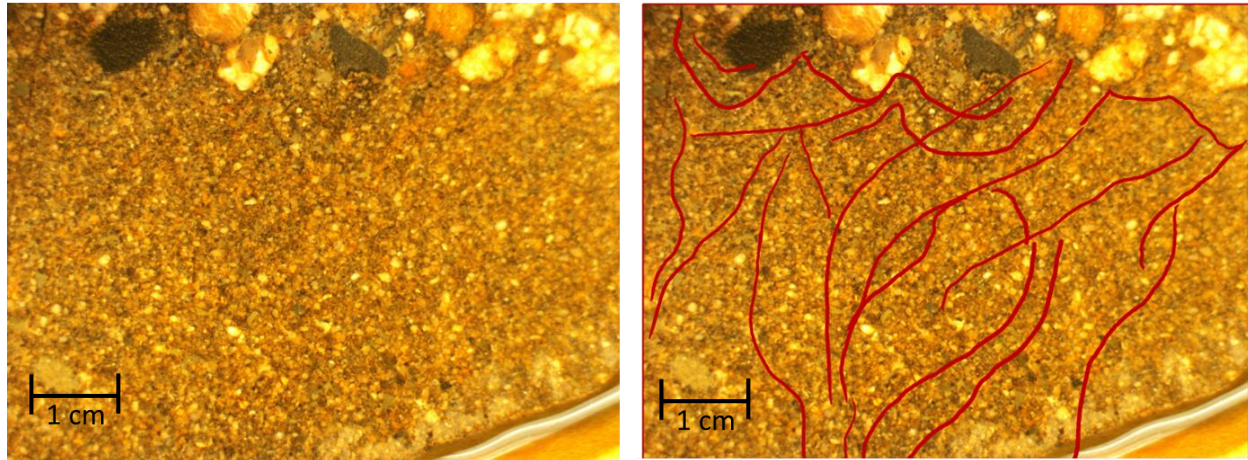
Figure 28: Photomicrograph of massive sandstone from EL6 showing water escape structures (highlighted on right.

Figure 29: Photo of sample sites EL8-1, a slab of coarse red sand between clast-poor muddy diamictite facies. Meter stick for scale.

Sandstone AMS description: Magnetic fabrics collected from sandstones throughout the EL outcrops are directionally consistent with fabrics from diamictite facies and with ripple orientations measured from EL6, suggesting a southwestern paleoflow direction (*Figure 30*). Sands from EL1 produced a variety of fabric types: Flow-oblique fabrics are apparent in *EL1-1 with k_3 axes clustering between 50° and 80° dip (azimuth 180°) and in EL1-2 which has k_3 clusters between 30° and 50° dip (azimuth 210° - 240°). EL1-1 shows a sub-vertical fabric with k_1 and k_2 axes clustered between 40° and 50° dip in opposite directions and k_3 axes clustered around 0°.

Sandy facies in EL5 have AMS characteristics that mimic those of their associated sandy Dms facies that bracket the sandstones stratigraphically. EL5-5 (massive sandstone) depicts a flow-transverse fabric and girdling of k_1 and k_2 axes whereas EL5-6 (reverse graded) shows a flow-oblique fabric and no girdling. In both cases, k_3 axes are clustered around 40° dip (azimuth 170° - 210°).

Outcrop EL6 proved extremely difficult to acquire block samples (sites) from, providing only one site (EL6-1) for AMS analysis which produced a vertical fabric, showing a tight cluster of k_1 at nearly 90° dip and k_2 and k_3 clusters close to 0°.

AMS produced sub-horizontal, oblate, flow-transverse fabrics from the strange slab of sand in EL8 expressing a north-western paleoflow direction (azimuth ~ 300°).
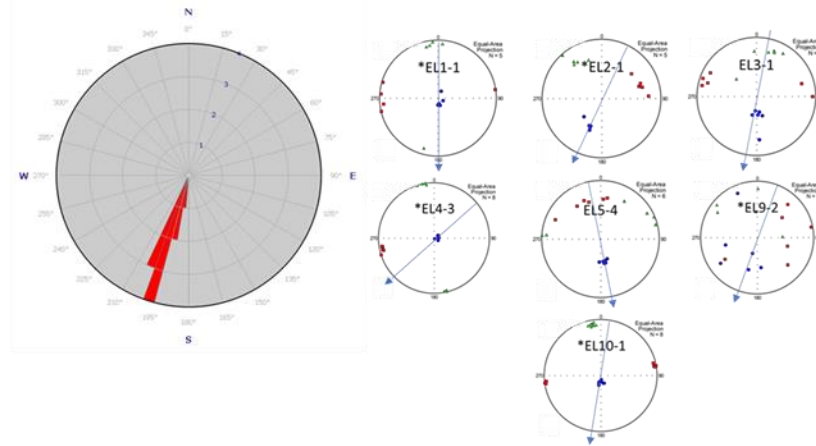
Figure 30: AMS (right) and ripple orientation (left) agreeing on a southwestern trend in transport direction.

Laminated Facies

Description: Sections of outcrops EL4, EL6, EL7 and the entirety of EL10 (*Figure 19; Figure 31*) resemble incomplete Bouma Sequences. Massive muds (centimeters thick) interbedded with thin, red, normally graded, very-fine sand dominate the sequence in EL4, EL6, and EL7 while EL10 contains much thinner mud layers and centimeter thick cross-laminated sands. Outsized clasts range from granule to cobble-sized, decreasing in size and abundance from EL4 to EL7, while EL10 is completely void of outsized material.

Laminated Facies AMS description: Laminated facies in outcrops EL4 and EL10 depict flow-transverse fabrics that are almost horizontal and show tight triaxial clustering of eigenvector axes: k_3 clustering near 80° dip in EL4-4 and 70° dip in *EL10-1. Specimens from EL7 produced vertical magnetic fabrics.

49
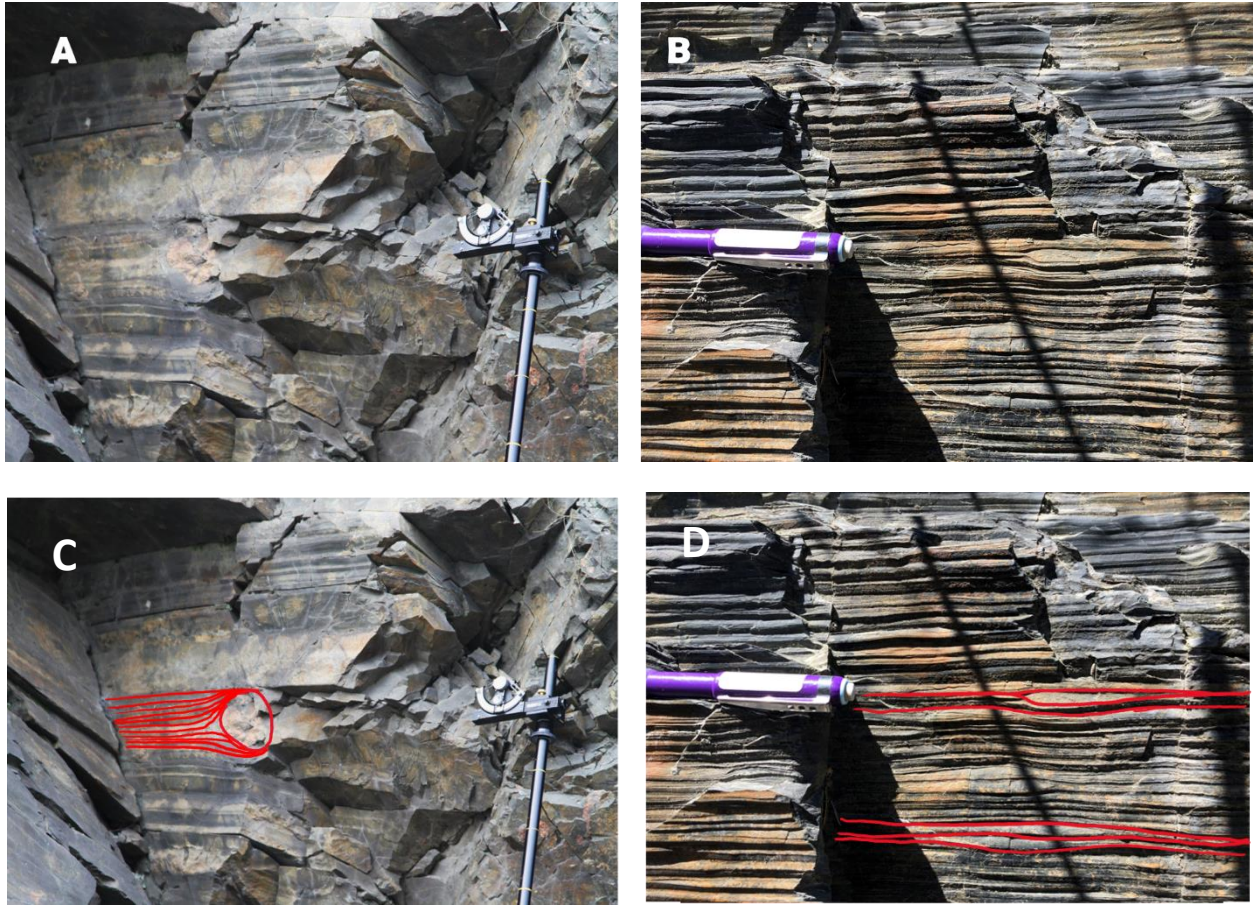
Figure 31: Laminated facies: Partial Bouma sequences at EL4 (A,C) show thicker layers and clasts whereas sequences at EL10 (B, D)are thinner, and do not include outsized clast. C) Highlighting a cobble-sized clast bending horizontal bedding below with onlapping layers above. D) Highlighting horizontal bedding and lenses of fine sand. Jacobs staff and pencil for scale.

.
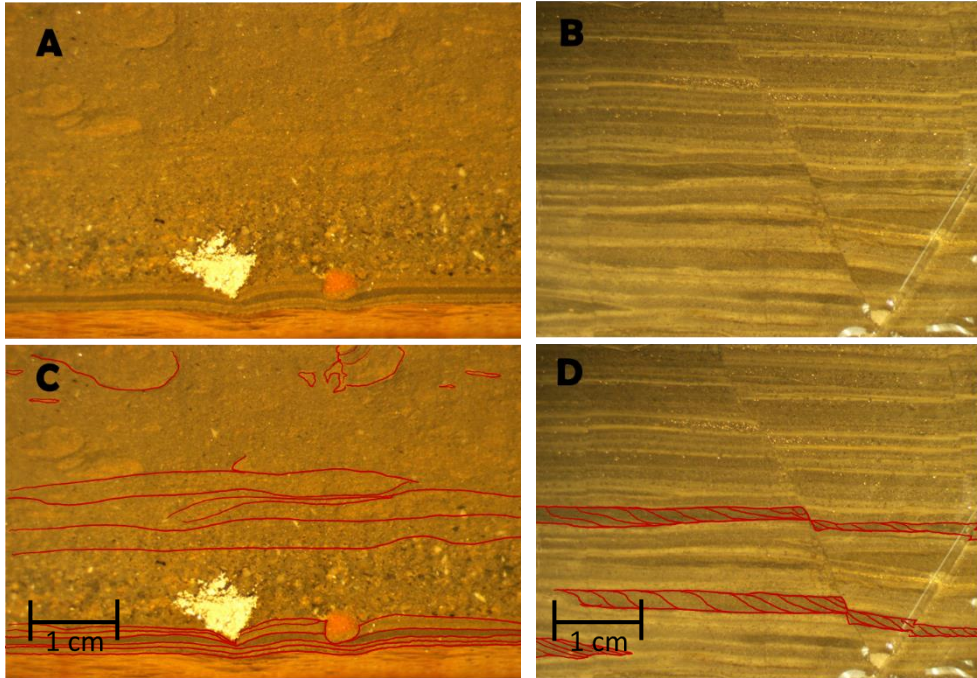
Figure 32: Microphotography of specimens displaying subhorizontal magnetic fabrics. A) *EL4-3 shows subhorizontal layering and normal grading. B) EL10-1 shows subhorizontal bedding of mud and fine-sands. Some sand layers displaying sedimentary structures suggesting the downstream accession of sediments. C and D highlight sedimentary microstructures.

Magnetic Behavior

Hysteresis Analysis

Hysteresis data show saturation magnetization ranging from 1.1x10-3 Am2/kg (EL1-1) to 1.8x10-1 Am^2/kg (EL5-4) (*Figure 33*) with most specimens displaying low coercivity (~12 – 50 mT) except EL1-1 and EL5-6 (*Appendix 1*) which have coercivities of ~100 mnT. An Mr/Ms over Bcr/Bc plot (*Figure 34*) shows that almost all specimens fall into the section of the Day plot consistent with multi-vortex magnetic behavior (or mixtures of SD and MD) and fall to the right of expected trends for pure magnetite developed in Dunlop (2002). This shift towards higher values of Bcr/Bc is consistent with contributions from higher-coercivity minerals (e.g.,
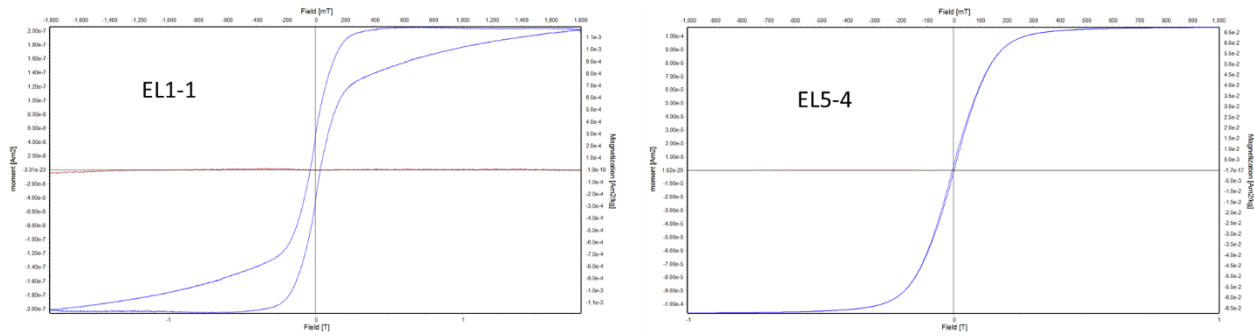
Figure 33: Hysteresis loops, depicting magnetic moment as a function of induced field intensity. These specimens were selected as behavioral endmembers, EL1-1 shows a wasp-wasted loop with low saturation magnetization and high coercivity whereas EL5-4 shows a very slim loop with higher saturation magnetization and low coercivity.
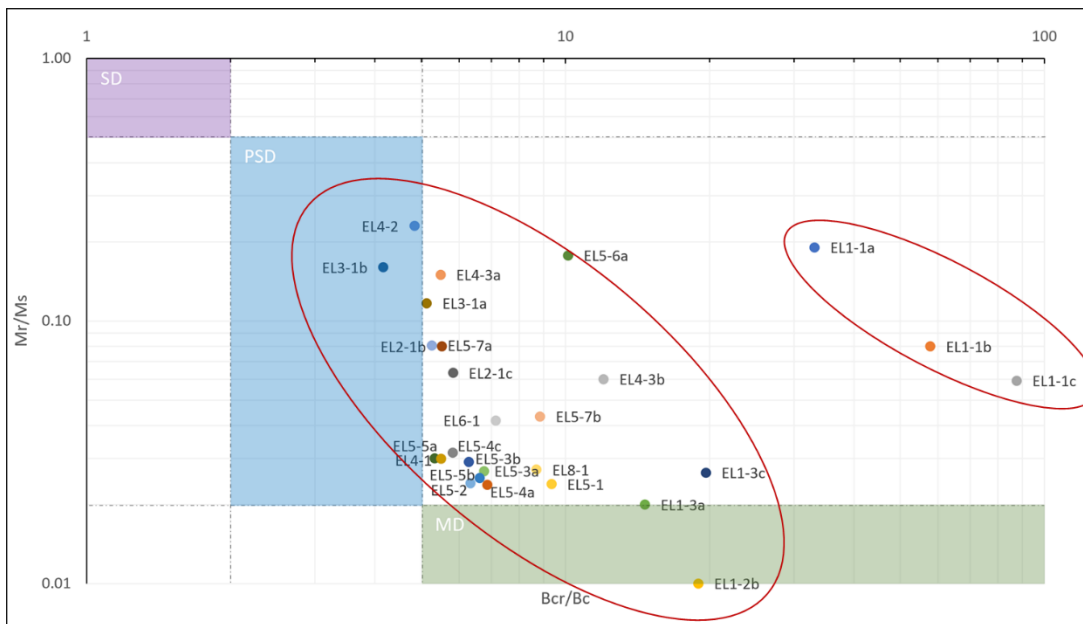
Figure 34: Day Plot showing two distinct groups of multi-vortex behavior: one with low coercivity and one with higher coercivity.

titanomagnetite, hematite, goethite). Bimodally distributed, the data show a distinct cluster of specimens with lower Mr/Ms to Bcr/Bc values (lower coercivity), expressing characteristics of multi-vortex magnetite or titanomagnetite, compared to values from the EL1 outcrop which show strong influence from higher coercivity components, most likely diagenetic goethite. (See below for additional evidence of goethite.)

Thermomagnetic Analysis

Oxidation resembling rust present at EL1 suggests diagenetic processes as a possible source of the higher coercivity values. Endmembers (EL1-1 and EL5-4) from each cluster (low coercivity and high coercivity respectively) were selected for further magnetic analysis at low-temperature (*Figure 35*). Specimen EL5-4, the low coercivity endmember, shows a clear Verwey Transition around 120K in both the FC/ZFC experiments and the RTSIRM experiment. This demonstrates the presence of near stoichiometric magnetite. EL1-1 has a much lower saturation magnetization, a much more subtle Verwey transition, and shows much stronger magnetization in the FC curve than its corresponding ZFC curve. This is consistent with acquisition of a thermal remanent magnetization in goethite during field cooling, possibly because of the very low Curie temperature of goethite (~ 70-125°C; *Liu et al., 2006*).

Curie temperature curves (high temperature analysis) (*Figure 36; Appendix B*) show Curie temperatures ~535 - 560 °C, although some data are extremely noisy (EL1-2c, EL4-4c, EL5-7c, and EL7-2d) due to low magnetic susceptibility. This suggests the presence of magnetite but in some cases, it is clear that magnetite is being created during the high-temperature measurement process (EL1-1*; Figure 36; Appendix B,*) making it difficult to determine whether it was present

prior to heating. In other cases (EL5-3, EL6-1, EL8-1), heating and cooling curves are nearly

reversible, suggesting the presence of magnetite in the starting sample. Although high

temperature data suggests magnetite is dominant present in all specimens, low temperature data

and high coercivity in EL1-1 most likely point to more than one magnetic component, most

likely the addition of goethite.

Figure 35: Low-temperature analysis of behavioral endmembers EL1-1 and EL5-4. EL5-4 shows a Verwey Transition, seen in the inflection point in the cooling curves around 120 K, which is typical of magnetite. EL1-1 has much lower saturation magnetism and shows inflection points around 20 K, 120 K and 190 K. The inflection at 120 K suggests trace amounts of magnetite, however, indicates that magnetism is dominated by other mineralogy, possibly goethite.
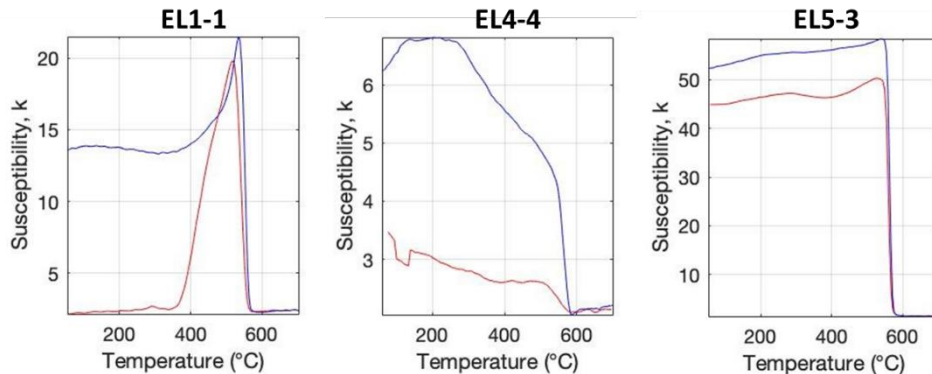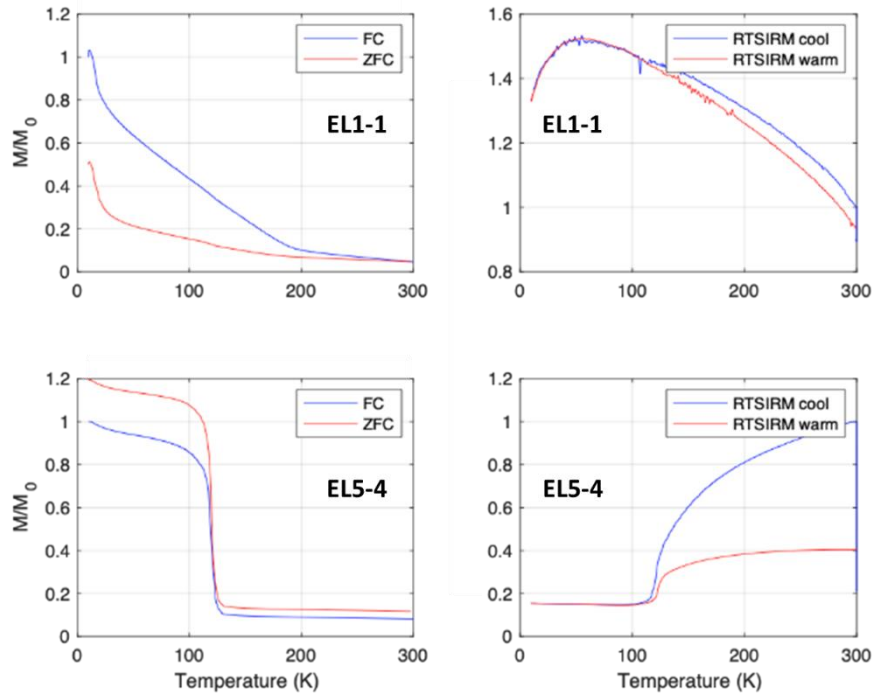
Figure 36: Three categories of Curie temperature curves showing magnetic susceptibility as a function of temperature (heating = red, cooling = blue). These specimens were selected based on hysteresis data that raised questions about magnetic mineralogy. EL1-2, EL4-4, EL5-7, and EL7-2 have extremely noisy data, most likely as a result of very low magnetic susceptibility (*Appendix B*).

AMS Data Analysis

Plots were made to visualize the trends in shape and degree of anisotropy (*Figure 37*). Degree of anisotropy (P) is the ratio of the maximum to the minimum eigenvectors (k_1/k_3; *Nagata, 1961*). A shape parameter (T; *Jelinek, 1981*) is also calculated from the eigenvectors, and ranges from 1 (oblate) to -1 (prolate). The lineation parameter (*Balsley and Buddington, 1960*), L, is equal to the ratio of k_1/k_2, and the foliation parameter (*Stacey et al., 1960*) F, is equal to the ratio of k_2/k_3.

Figure 37: T/P plot showing most specimen fabrics in the triaxial-oblate range. Flin Plot (L/F) showing mostly oblate fabrics with low degree of anisotropy. P/Kmean plot showing that most specimens have a low degree of anisotropy (1.01 – 1.14).

At the specimen level, magnetic anisotropy data show a general oblate to triaxial trend in susceptibility ellipsoid shape, except *EL7-1 which has a prolate shaped ellipsoid. P values ranges between 1.01 and 1.14 (*Figure 37*). Sites with more dispersed P values typically display greater uncertainty in eigenvector orientation than those with P values that are tightly clustered. This may be an indication that magnetic fabrics are less profound in specimens containing a variety of particle shape and degree of anisotropy (P values) (*Appendix C*).

Most sites throughout the Gowganda showed flow-transverse to flow-oblique fabrics hinting at the deposition of sediment-rich viscous flows that involved clast interaction (oblique fabric) and high-velocity fluid-like flow (flow-transverse fabrics). Fabric orientation throughout the sites can be separated into two main categories: horizontal/subhorizontal and vertical/subvertical in orientation (*Figure 38*). Sixteen of 25 sites produced horizontal/subhorizontal AMS fabrics depicting clusters of k_3 eigenvectors typically deviating from <10° to 45° from vertical in almost all cases toward a south/southwestern direction. Of these sites, most magnetic fabrics showed girdling of k_1 and k_2 eigenvectors and are indicative of the down-slope transport of sediment due to gravity. Nine out of 25 sites however, produced vertical/subvertical fabrics (*Figure 39*, depicting k_1 or k_2 eigenvectors clustered near the center and k_3 eigenvectors clustered near the edge of the stereonet. Sites producing vertical/subvertical fabrics showed physical evidence of dewatering, most likely due to rapid escape of water from previously dilated poor-space upon settling of a SGF (see below).
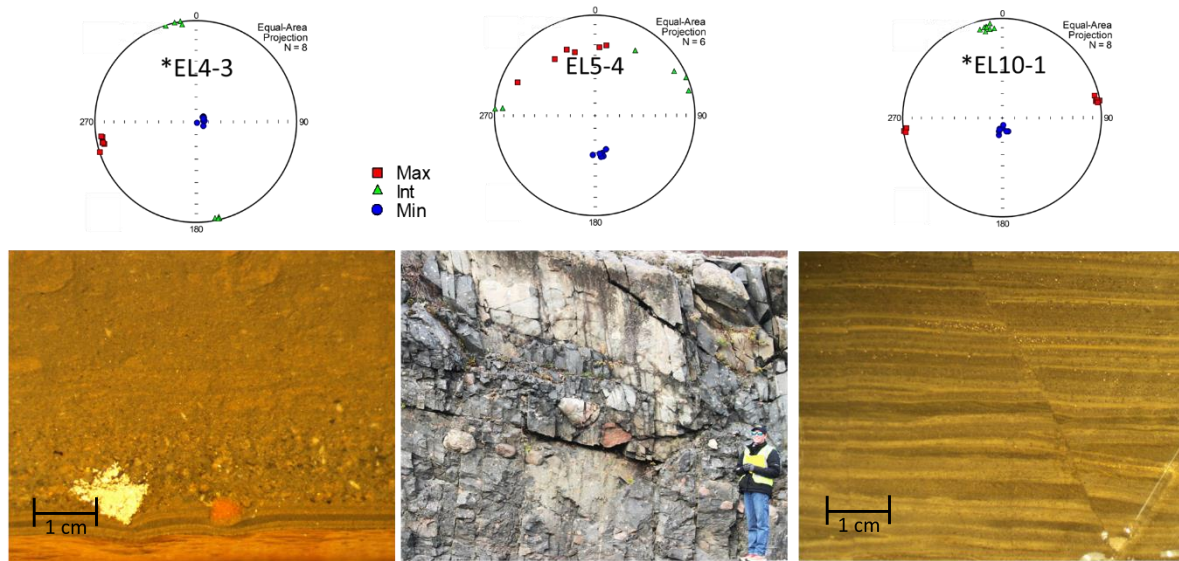
Figure 38: Examples of horizontal-subhorizontal AMS plots associated with horizontal-subhorizontal sedimentary features. *EL4-3 (left) and *EL10-1 (right) show nearly horizontal sedimentary structures and nearly horizontal AMS fabrics. EL5-4 (center) shows dipping bed and magnetic fabric dipping ~30°.
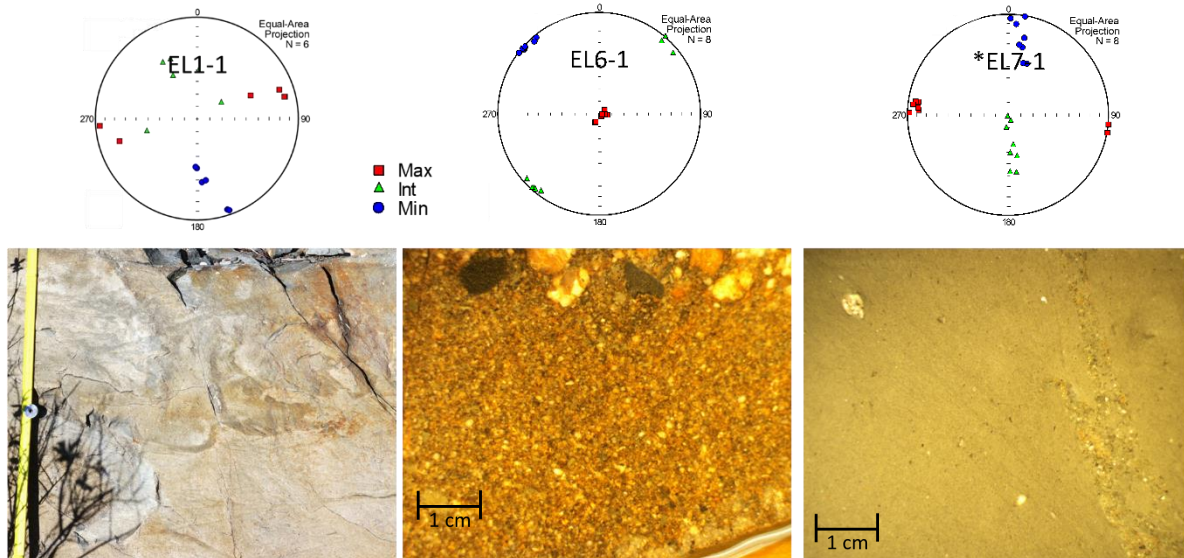
Figure 39: Examples of vertical-subvertical AMS plots associated with vertical-subvertical sedimentary features (dewatering structures). EL1-1 (left; Meter stick for scale) shows macro-scale dewatering structures (dish structures). EL6-1 (center) is a sandstone that appeared massive at the outcrop but produced vertical AMS fabric and shows vertical dewatering structures in photomicrograph. EL7-1(right) is a massive muddy diamictite that produced vertical AMS fabrics and shows vertical dewatering structures in photomicrograph.

Figure 40: Stratigraphy showing the full thickness of the Gowganda, depicted with site locations and their AMS plots. Sites names are arranged in order of superposition.
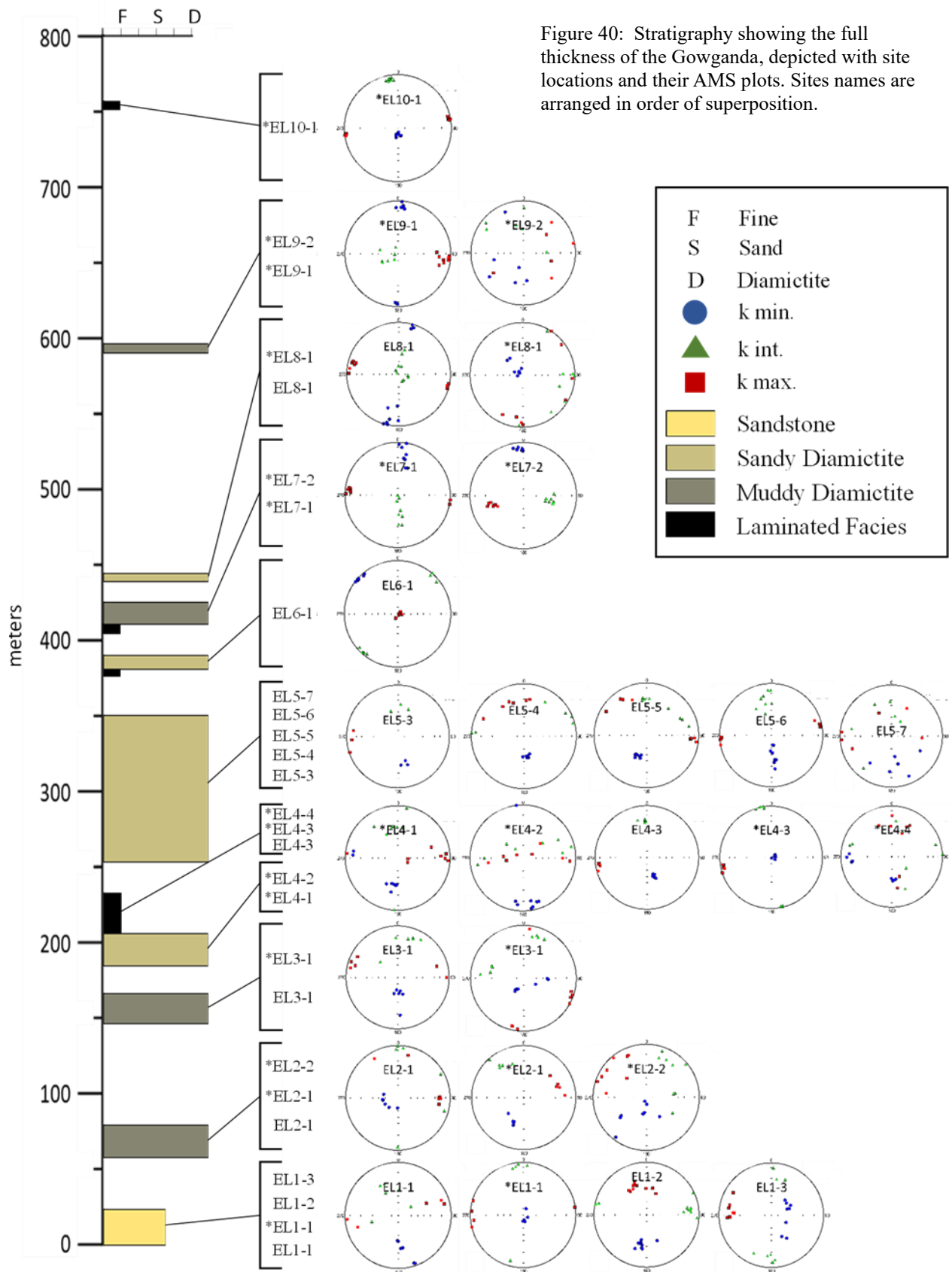
Discussion

Interpretations

Muddy Diamictite Facies: Muddy Dmm diamictites fit the description of non-cohesive SGF

deposits laid out by Rees 1983 (sediment concentration between 1.2% and 11.1% by volume)

showing evidence of laminar flow in the form of horizontal/sub-horizontal magnetic fabrics,

clast horizons, quarter structures (eye-shaped distortion of sediment around clasts suggesting

clast rotation), and necking (the squeezing of saturated sediment between clasts). (*Figure 5*;

Eyles, 1987; Mulder and Alexander, 2001; Haughton, 2009). Although muddy Dmm and sandy

Dms facies exhibit very similar traits, differences in matrix sand content, stratification, and clast

abundance may reflect sedimentation at different stages of a flow (i.e., as cohesion decreases).

For instance, muddy Dmm facies depict characteristics of hyperconcentrated density flows

(*Figure 5; Mulder and Alexander, 2001*): high porewater pressure and larger transport distance.

Dmm facies have the finest matrix throughout the EL outcrops and are completely ungraded.

Unlike in other muddy Dmm facies, outsized clasts in EL7 are extremely sparse. Vertical

magnetic fabrics and water-escape structures point to the *en masse* deposition of fine material

with porewater pressure large enough to carry cobble-sized clasts in suspension (*Figure 5*;

Haughton, 2009; Talling et al., 2012).

Sandy Diamictite Facies: Sandy Dms facies show the same characteristics of muddy Dmm but

with the addition of sub-horizontal deformation structures and clast horizons, evidence of co-

genetic/composite flow behavior (*Figure 5; Figure 20C,D*). Dms produced steeper dipping sub-

horizontal magnetic fabrics than muddy Dmm facies, and show Sedimentary observations and

AMS data show that Dms facies within the EL outcrops may be attributed to non-cohesive

concentrated density flows (*Figure 5; Mulder and Alexander, 2001*). Sandier sediments are interpreted as being deposited closer to the source compared to muddy Dmm facies based on muds being able to travel longer distances than larger particles.

Clast-Supported Diamictite: Discontinuous and laterally graded Dcm facies of EL6 and EL8 can also be attributed to hyperconcentrated density flows (*Figure 5; Mulder and Alexander, 2001*). Reverse grading in Dcs facies may be attributed to kinetic sieving (the upward movement of larger particles) resulting from clast interaction. Evidence for hyperconcentrated density flow deposition in EL6 is further depicted by the settling of sand around protruding boulders at the top of the flow body, a characteristic typical of co-genetic deposition where smaller particles are incorporated into the water column and settle after the coarser material is deposited (*Mulder and Alexander, 2001*).

Sandstone Facies: Planner to cross-laminated bedforms inferable in EL1 range from undisturbed to totally deformed as a result of dewatering (*Young, 1991*). These characteristics are standard of dilated, non-cohesive, hyperconcentrated density flows (grain flows; *Figure 5*; *Mulder and Alexander, 2001*) or high-density turbidity flows (*Talling et al., 2012*) where water is forced to escape from oversaturated pore space upon rapid deposition, deforming sedimentary bedforms. Furthermore, those exhibiting horizontal/sub-horizontal bedforms produced sub-horizontal magnetic fabrics, with flow-transverse orientation, a characteristic of laminar flow, whereas those containing dewatering features produced sub-vertical magnetic fabrics.

Normal grading and dewatering features in sandstones of EL6 (*Figure 27; Figure 28*), and EL8 display co-genetic depositional behavior with the stratigraphically adjacent Dcm/Dcs facies. Evidence here suggests the settling of particles under non-cohesive conditions and can most likely be attributed to the deposition of concentrated density flows (*Figure 5; Mulder and Alexander, 2001; Haughton, 2009*). In his 1983 publication, Miall describes a subaqueous channel which may explain the slab of sand in EL8 (*Figure 29*) with a SW paleoflow direction.

Laminated Facies: Characteristic of concentrated density flows and turbidity flows (underflows) are depicted in the layering of mud and fine sand in outcrops EL4, EL6, EL7 and EL10 (*Figure 5; Mulder and Alexander, 2001*). EL4 shows thin layers of sand normally grading into mud, sometimes containing vertical water-escape pipes and soft-sediment deformation whereas EL10 shows thinner mud layers and much finer, cross-laminated sands (*Figure 32B, C*). Slightly flow-transverse magnetic fabrics indicate particles settling from suspension and influenced by impulses of turbulent flow, directionally consistent with the rest of the EL outcrops (SW) (*Figure 30*). Some clasts present in these facies range from granule to cobble-sized and display evidence of individual deposition by subaqueous rain-out in the form of bending, penetration, and rucking of underlying laminae as well as the onlap of overlying sediments, yet others show deformation that suggest plowing of sediment (*Figure 32A*). Coarser material at EL4 along with the lack of out-sized clasts in EL10 suggest that deposition of EL4 had occurred closer to the source and that sea-ice or icebergs were present during the deposition of EL4, but not during EL10.

Overview

Field observations and AMS data show characteristics of SGF processes. *Frarey and Roscoe's* 1970 paper suggests basin downwarp from the advance of glacial ice leading to rapid sedimentation, triggering reactionary rebound oscillations. Although identifying such dynamics is highly speculative, this perspective could allow for the floating of ice during periods of downwarp and grounding (evident from the striated, facetted boulder pavement at EL5) during periods of rebound, potentially influencing changes in grain-size concentration. However, it is more likely that short-scale ice advances and retreats have contributed to depositional variation throughout the Gowganda as well, but it is possible that deposition was influenced by both processes, or possibly more.

Most outcrops lack substantial evidence of basal ice contact, except a boulder bed at EL5. Boulders in this horizon are the only potential evidence of grounded ice and appear striated, facetted, and with their long axes aligned. Associated with this boulder bed is a flow-aligned magnetic fabric, which are typical in sediments which have undergone subglacial deformation and is used here to interpret EL5 as a product of sediment/ice contact (*Figure 23*). The rest of the Gowganda in this area shows evidence of proglacial deposition by SGFs on a continental margin under varying conditions. EL1 may represent a proglacial deltaic progradation into a deep marine basin, possibly reworked sands of the Serpent Formation, redeposited by hyperconcentrated density flows (grain flows). After EL1, the Gowganda records 5 periods of decreased sand content represented by muddy Dmm and turbidites, and 4 periods of increased sand content shown by Dms, Dcs, and sandstone facies.

In EL6 and EL8 Dcs and sandstone facies alternate, showing co-genetic characteristics (*Haughton, 2009*). Argument for 'transitional' concentrated density flow is presented in erosional contacts between reverse graded cobble-sized material and underlying sands, along with the draping of sands around protruding clasts possibly due to sands of a flow settling later than coarser material (*Mulder and Alexander 2001; Figure 5; Figure 24*). To further support this hypothesis, dewatering structures and vertical magnetic fabrics from one sandstone layer in EL6 suggest rapid deposition of saturated sediment. The abundance of coarse material may suggest deposition potentially close to the grounding line.

Sandy diamictites have features that suggest low-viscosity, non-cohesive (concentrated density flows). With higher mud content, sandy diamictite facies may experience more cohesion than sandstone or Dcs facies, possibly aiding in greater transport distance and deposition further away from the grounding line. Likewise, muddy diamictites may experience higher cohesion than sandy diamictites, potentially resulting in deposition even more distal than sandy diamictites.

Laminated muds in EL4, EL6, EL7, and EL10 represent even more distal deposition than muddy diamictite facies and are interpreted as turbidites. Outsized clasts are common in all but EL10. Penetration and disturbance of underlying bedding by outsized clasts provides evidence for the rain-out of debris by sea-ice or icebergs. These dropstones decrease in size and concentration from EL4, to EL7 and are completely absent in EL10. It is possible that the Dcm facies at the base of EL2 is a result of ice-rafting, potentially dumped from a rolling iceberg.

AMS fabrics in sandy Dmm and Dsm facies depict steeper imbrication angles compared to those generated by muddy Dmm facies and the thinly layered Laminated facies are nearly horizontal. The decline in imbrication angle from sandy Dms (high) to thinly layered turbidites (low) may indicate that sandy Dms facies were deposited on a post-glacial or continental slope and turbidites deposited on an abyssal plane. Sites with steeper k_3 dips (sandy diamictites) may represent sedimentary transport in the early stages of flow transformation, deposited mid-proglacial slope, while thinly layered turbidites are deposited on the basin floor and muddy diamictites somewhere between. It is probable that variations in sand content may record isostatic basin adjustments through time, although the possibility of small-scale advance and retreat of the ice sheet cannot be ruled out (*Figure 41*).
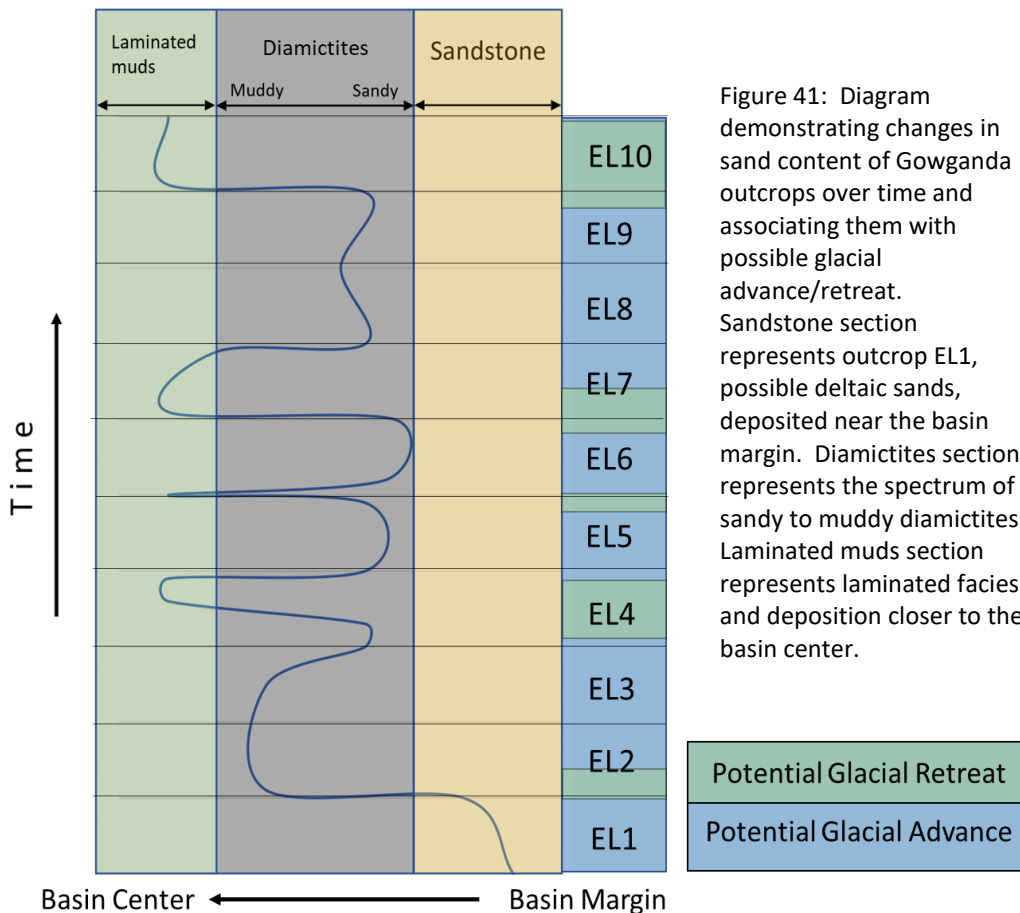
Figure 41: Diagram demonstrating changes in sand content of Gowganda outcrops over time and associating them with possible glacial advance/retreat. Sandstone section represents outcrop EL1, possible deltaic sands, deposited near the basin margin. Diamictites section represents the spectrum of sandy to muddy diamictites. Laminated muds section represents laminated facies and deposition closer to the basin center.

Transport/Paleoflow Direction

Magnetic fabrics, ripple orientation, and thinning Dcs facies throughout the EL outcrops agree on a general southwesterly paleoflow direction, except for a small number of vertical magnetic fabrics, most likely products of the vertical escape of water from oversaturated pore-space during deposition. The association of vertical magnetic fabrics with water escape structures grants confidence that AMS data displays clear, minimally-altered depositional fabrics and can be used in determining paleoflow direction.

Conclusions

The Gowganda Formation represents the last of three major advances of the Huronian glaciation on the southern continental margin of the Superior craton during the Paleoproterozoic. Of debatable origin among sedimentologists, diamictites of the Gowganda have been previously identified as glacial till (*Young, 1991*) and as pro-glaciomarine sediments (*Miall, 1983*) which occur under quite different conditions and have different implications for modeling climate and glaciation. Insights gleaned from this project align with the findings of Miall, suggesting that most facies types throughout the Gowganda north of Elliot Lake were deposited by a spectrum of SGF deposits in a glaciomarine environment. Findings outlined in this paper demonstrate that the use of magnetic fabric analysis coupled with sedimentological evaluation can offer a detailed understanding of sedimentary processes that can be used relatively straightforward to infer sedimentary transport direction and paleoenvironmental conditions even in ancient sediments.

Future investigation on exposures near Cobalt, Whitefish Falls, and Bruce Mines Ontario

(northeast, southeast and west of Elliot Lake respectively) using methods from this paper is

necessary for a broader vision of conditions controlling Gowganda deposition and may provide a

more robust sense of ice extent and depositional dynamics during the Paleoproterozoic.

References:

Amato, J.A., 2017. Using AMS to Help Interpret Glaciogenic Deposits of the Late Paleozoic Ice Age in the Paraná Basin, Brazil (MS thesis, The University of Wisconsin-Milwaukee).

Baas, J.H., Hailwood, E.A., McCaffrey, W.D., Kay, M. and Jones, R., 2007. Directional petrological characterisation of deep-marine sandstones using grain fabric and permeability anisotropy: methodologies, theory, application and suggestions for integration. *Earth-Science Reviews*, *82*(1-2), pp.101-142.

Baas, J.H., Best, J.L. and Peakall, J., 2011. Depositional processes, bedform development and hybrid bed formation in rapidly decelerated cohesive (mud‑sand) sediment flows. *Sedimentology*, 58(7), pp.1953-1987.

Balsley, J.R. and Buddington, A.F., 1960. Magnetic susceptibility anisotropy and fabric of some Adirondack granites and orthogneisses. *American Journal of Science*, *258*(6), p.e20.

Benn, D., 1994. Fabric shape and the interpretation of sedimentary fabric data. *Journal of Sedimentary Research*, 64(4a), pp.910-915.

Benn, D. and Evans, D.J., 2010. *Glaciers and Glaciation* (pp. 363-440), Routledge Oxfordshire.

Boulton, G.S., 1978. Boulder shapes and grain-size distributions of debris as indicators of transport paths through a glacier and till genesis. *Sedimentology*, 25(6), pp.773-799.

Butler, R.F., 1992. *Paleomagnetism: Magnetic Domains to Geologic Terranes*. Boston: Blackwell Scientific Publications.

Casshyap, S.M., 1969. Petrology of the Bruce and Gonganda formations and its bearing on the evolution of Huronian sedimentation in the Espanola-Willisville area, Ontario (Canada). *Palaeogeography, Palaeoclimatology, Palaeoecology*, 6, pp.5-36.

Chadima, M. and Jezek, J., 2021, April. A toolbox for convenient calculation of anisotropy of magnetic remanence. *EGU General Assembly Conference Abstracts* (pp. EGU21-1155).

Day, R., Fuller, M. and Schmidt, V.A., 1977. Hysteresis properties of titanomagnetites: grain-size and compositional dependence. *Physics of the Earth and Planetary Interiors*, *13*(4), pp.260-267.

Dreimanis, A., 1989. Tills: their genetic terminology and classification. *Genetic classification of glacigenic deposits. Final report of the commission on genesis and lithology of glacial Quaternary deposits of the International Union for Quaternary Research (INQUA)*, pp.17-83.

Dunlop, D.J., 2002. Theory and application of the Day plot (Mrs/Ms versus Hcr/Hc) 1. Theoretical curves and tests using titanomagnetite data. *Journal of Geophysical Research: Solid Earth*, *107*(B3), pp.EPM-4.

Embleton, C. and King, C.A.M., 1975. Glacial and periglacial geomorphology.

Evans, D.J.A., Phillips, E.R., Hiemstra, J.F. and Auton, C.A., 2006. Subglacial till: formation, sedimentary characteristics and classification. *Earth-Science Reviews*, 78(1-2), pp.115-176.

Evans, D.J., Roberts, D.H., Hiemstra, J.F., Nye, K.M., Wright, H. and Steer, A., 2018. Submarginal debris transport and till formation in active temperate glacier systems: the southeast Iceland type locality. *Quaternary Science Reviews*, *195*, pp.72-108.

Eyles, N., Day, T.E. and Gavican, A., 1987. Depositional controls on the magnetic characteristics of lodgement tills and other glacial diamict facies. *Canadian Journal of Earth Sciences*, 24(12), pp.2436-2458.

Fischer, U., Clarke, G.K.C., Blatter, H., 1999. Evidence for temporally varying "sticky spots" at the base of Trapridge Glacier, Yukon Territory, Canada. *Journal of Glaciology* 45, pp. 352–360.

Fischer, U., Clarke, G.K.C., 2001. Review of subglacial hydromechanical coupling: Trapridge Glacier, Yukon Territory, Canada. *Quaternary International* 86, pp.29–43.

Frarey, M.J. and Roscoe, S.M., 1970. The Huronian Supergroup north of Lake Huron. In *Symposium on basins and geosynclines of the Canadian Shield* (Vol. 70, pp. 143-157). Geological Survey of C, Paper 70-40.

García, J. and Subías, G., 2004. The Verwey transition—a new perspective. *Journal of Physics: Condensed Matter*, 16(7), pp.R145.

Gentoso, M.J., Evenson, E.B., Kodama, K.P., Iverson, N.R., Alley, R.B., Berti, C. and Kozlowski, A., 2012. Exploring till bed kinematics using AMS magnetic fabrics and pebble fabrics: the Weedsport drumlin field, New York State, USA. *Boreas*, 41(1), pp.31-41.

Gilbert, R., 1990. Rafting in glacimarine environments, in Dowdeswell, J.A., and Scourse, J.D., *Geological Society, London, Special Publications*, *53*(1), pp.105-120.

Gravenor, C.P., Stupavsky, M. and Symons, D.T.A., 1973. Paleomagnetism and its relationship to till deposition. *Canadian Journal of Earth Sciences*, *10*(7), pp.1068-1078.

Hailwood, E. and Ding, F., 2000. Sediment transport and dispersal pathways in the Lower Cretaceous sands of the Britannia Field, derived from magnetic anisotropy. *Petroleum Geoscience*, *6*(4), pp.369-379.

Haldorsen, S., 1981. Grain-size distribution of subglacial till and its realtion to glacial crushing and abrasion. *Boreas*, 10(1), pp.91-105.

Haughton, P.D., 1994. Deposits of deflected and ponded turbidity currents, Sorbas Basin, Southeast Spain. *Journal of Sedimentary Research*, 64(2a), pp.233-246.

Haughton, P., Davis, C., McCaffrey, W. and Barker, S., 2009. Hybrid sediment gravity flow deposits–classification, origin and significance. *Marine and Petroleum Geology*, 26(10), pp.1900-1918.

Hart, J.K. and Roberts, D.H., 1994. Criteria to distinguish between subglacial glaciotectonic and glaciomarine sedimentation, I. Deformation styles and sedimentology. *Sedimentary Geology*, 91(1-4), pp.191-213.

Hiemstra, J.F. and Rijsdijk, K.F., 2003. Observing artificially induced strain: implications for subglacial deformation. *Journal of Quaternary Science*, *18*(5), pp.373-383.

Hooyer, T.S., Iverson, N.R., Lagroix, F. and Thomason, J.F., 2008. Magnetic fabric of sheared till: A strain indicator for evaluating the bed deformation model of glacier flow. *Journal of Geophysical Research: Earth Surface*, *113*(F2).

Hopkins, N.R., Evenson, E.B., Kodama, K.P. and Kozlowski, A., 2016. An anisotropy of magnetic susceptibility (AMS) investigation of the till fabric of drumlins: support for an accretionary origin. *Boreas*, 45(1), pp.100-108.

Hrouda, F., 1994. A technique for the measurement of thermal changes of magnetic susceptibility of weakly magnetic rocks by the CS-2 apparatus and KLY-2 Kappabridge. *Geophysical Journal International*, *118*(3), pp.604-612.

Hutter, K. and Rajagopal, K.R., 1994. On flows of granular materials. *Continuum Mechanics and Thermodynamics*, 6(2), pp.81-139.

Isbell, J.L., Vesely, F.F., Rosa, E.L.M., Pauls, K.N., Fedorchuk, N.D., Ives, L.R.W., McNall, N.B., Litwin, S.A., Borucki, M.K., Malone, J.E., Kusick, A.R., 2021. Evaluation of physical and chemical proxies used to interpret past glaciations with a focus on the late Paleozoic Ice Age. *Earth-Science Reviews*, 103756.

Iverson, R.M., 1997. The physics of debris flows. *Reviews of Geophysics*, *35*(3), pp.245-296.

Ives, L.R.W. and Iverson, N.R., 2019. Genesis of glacial flutes inferred from observations at Múlajökull, Iceland. *Geology*, *47*(5), pp.387-390.

Jelínek, V., 1981. Characterization of the magnetic fabric of rocks. *Tectonophysics*, *79*(3-4), pp.T63-T67.

Jelínek, V., 1997. Measuring anisotropy of magnetic susceptibility on a slowly spinning specimen—basic theory. *AGICO print*, (10), pp.27.

Lindsey, D.A., 1969. Glacial sedimentology of the Precambrian Gowganda Formation, Ontario, Canada. *Geological Society of America Bulletin*, *80*(9), pp.1685-1702.

Lisitzin, A. P., 2002. Sea-Ice and Iceberg Sedimentation in the Ocean: Recent and Past. Lisicyn, A. P., *Springer Science & Business Media*, New York, pp.563.

Liu, Q., Yu, Y., Torrent, J., Roberts, A.P., Pan, Y. and Zhu, R., 2006. Characteristic low-temperature magnetic properties of aluminous goethite [α-(Fe, Al) OOH] explained. *Journal of Geophysical Research: Solid Earth*, 111(B12).

Massari, F., 1984. Resedimented conglomerates of a Miocene fan-delta complex, Southern Alps, *Sedimentology of Gravels and Conglomerates − Memoir 10, 1984. Ancient Fan-Delta Systems*, pp. 259-277.

Menzies, J., 2000. Microstructures in diamictites of the lower Gowganda Formation (Huronian), near Elliot Lake, Ontario: evidence for deforming-bed conditions at the grounding line? *Journal of Sedimentary Research*, 70(1), pp. 210-216.

Menzies, J., van der Meer, J.J. and Rose, J., 2006. Till—as a glacial "tectomict", its internal architecture, and the development of a "typing" method for till differentiation. *Geomorphology*, *75*(1-2), pp.172-200.

Menzies, J., 2022. Differentiation of diamictons (glacigenic‑non-glacigenic) using microstructure abundancies and types. *Proceedings of the Geologists' Association*, 133(6), pp.603-615.

Miall, A.D., 1983. Glaciomarine sedimentation in the Gowganda Formation (Huronian), northern Ontario. *Journal of Sedimentary Research*, *53*(2), pp.477-491.

Mulder, T., and Alexander, J., 2001. The physical character of subaqueous sedimentary density flows and their deposits. *Sedimentology* 48, pp.269-299.

Mustard, P.S. and Donaldson, J.A., 1987. Substrate quarrying and subglacial till deposition by an early Proterozoic ice sheet: evidence from the Gowganda Formation at Cobalt, Ontario, Canada. *Precambrian research*, *34*(3-4), pp.347-368.

Nagata, T., 1961. Rock Magnetism. Tokyo: Maruzen.

Pickering, K., and Hiscott, R., 2016. *Deep marine systems: Processes, deposits, environments, tectonics and sedimentation*. Wiley:American Geophysical Union: West Sussex, England, 1393 pp.

Postma, G., Nemec, W. and Kleinspehn, K.L., 1988. Large floating clasts in turbidites: a mechanism for their emplacement. *Sedimentary Geology*, 58(1), pp.47-61.

Potter, D.K. and Stephenson, A., 1988. Single-domain particles in rocks and magnetic fabric analysis. *Geophysical Research Letters*, *15*(10), pp.1097-1100.

Roberts, A. P., Tauxe, L., Heslop, D., Zhao,X., & Jiang, Z. (2018). A critical appraisal of The "Day" diagram. *Journal of Geophysical Research: Solid Earth*, 123, 2618–2644.

Rodrigues, M.C.N.d.L., Trzaskos, B., Alsop, G.I., Vesely, F.F., 2020. Making a homogenite: An outcrop perspective into the evolution of deformation within mass-transport deposits. *Marine and Petroleum Geology* 112, 104033.

Rees, A.I., 1983. Experiments on the production of transverse grain alignment in a sheared dispersion. *Sedimentology*, 30(3), pp.437-448.

Stacey, F.D., Joplin, G. and Lindsay, J., 1960. Magnetic anisotropy and fabric of some foliated rocks from SE Australia. *Geofisica pura e applicata*, *47*, pp.30-40.

Sumner, E.J., Talling, P.J. and Amy, L.A., 2009. Deposits of flows transitional between turbidity current and debris flow. *Geology*, 37(11), pp.991-994.

Talling, P.J., Wynn, R.B., Masson, D.G., Frenz, M., Cronin, B.T., Schiebel, R., Akhmetzhanov, A.M., Dallmeier-Tiessen, S., Benetti, S., Weaver, P.P.E. and Georgiopoulou, A., 2007. Onset of submarine debris flow deposition far from original giant landslide. *Nature*, 450(7169), pp.541-544.

Talling, P.J., Masson, D.G., Sumner, E.J., Malgesini, G., 2012. Subaqueous sediment density flows: Depositional processes and deposit types. *Sedimentology* 59, 1937-2003.

Tarling, D. and Hrouda, F. eds., 1993. The *Magnetic Anisotropy of Rocks*. Chapman and Hall: New York, pp.217.

Tauxe, L, Banerjee, S.K., Butler, R.F. and van der Voo R, *Essentials of Paleomagnetism*, 5th Web Edition, 2018.

Thomas, G.S. and Connell, R.J., 1985. Iceberg drop, dump, and grounding structures from Pleistocene glacio-lacustrine sediments, Scotland. *Journal of Sedimentary Research*, 55(2), pp.243-249.

Tremblay, L. B., Schmidt, G. A., Pfirman, S., Newton, R., & DeRepentigny, P., 2015. Is ice-rafted sediment in a North Pole marine record evidence for perennial sea-ice cover? Philosophical Transactions of the Royal Society A: *Mathematical, Physical and Engineering Sciences*, 373(2052), 20140168. https://doi.org/doi:10.1098/rsta.2014.0168.

Tulaczyk, S., 1999. Ice sliding over weak, fine-grained tills: dependence of ice-till interactions on till granulometry. *in* Mickelson, D. M., and Attig, J. W., *Glacial Processes Past and Present*, *Geological Society of America Special Paper 337*, pp.159-178.

Vesely, F., 2020. Lithological indicators of glaciation: why do they still matter? *Geological Society of America Abstracts with Programs* 52.

Young, G.M., 1991. Stratigraphy, sedimentology and tectonic setting of the Huronian Supergroup. *Geological Association of Canada*, pp.34.

APENDIX A

Hysteresis Data

Appendix A

Appendix A: Hysteresis loops, depicting magnetic moment as a function of induced field intensity.
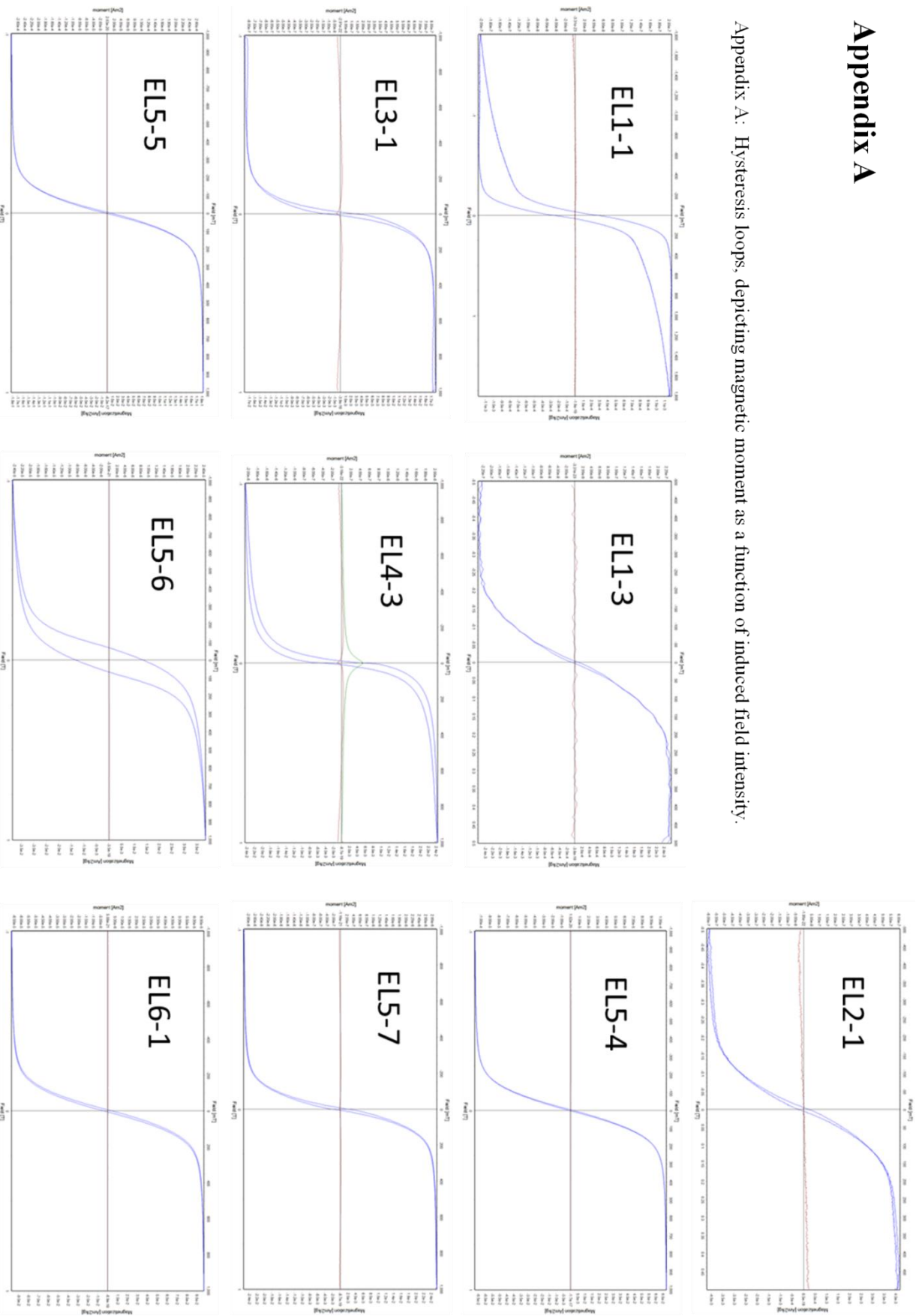
APENDIX B
Curie Temperature Data

Appendix B
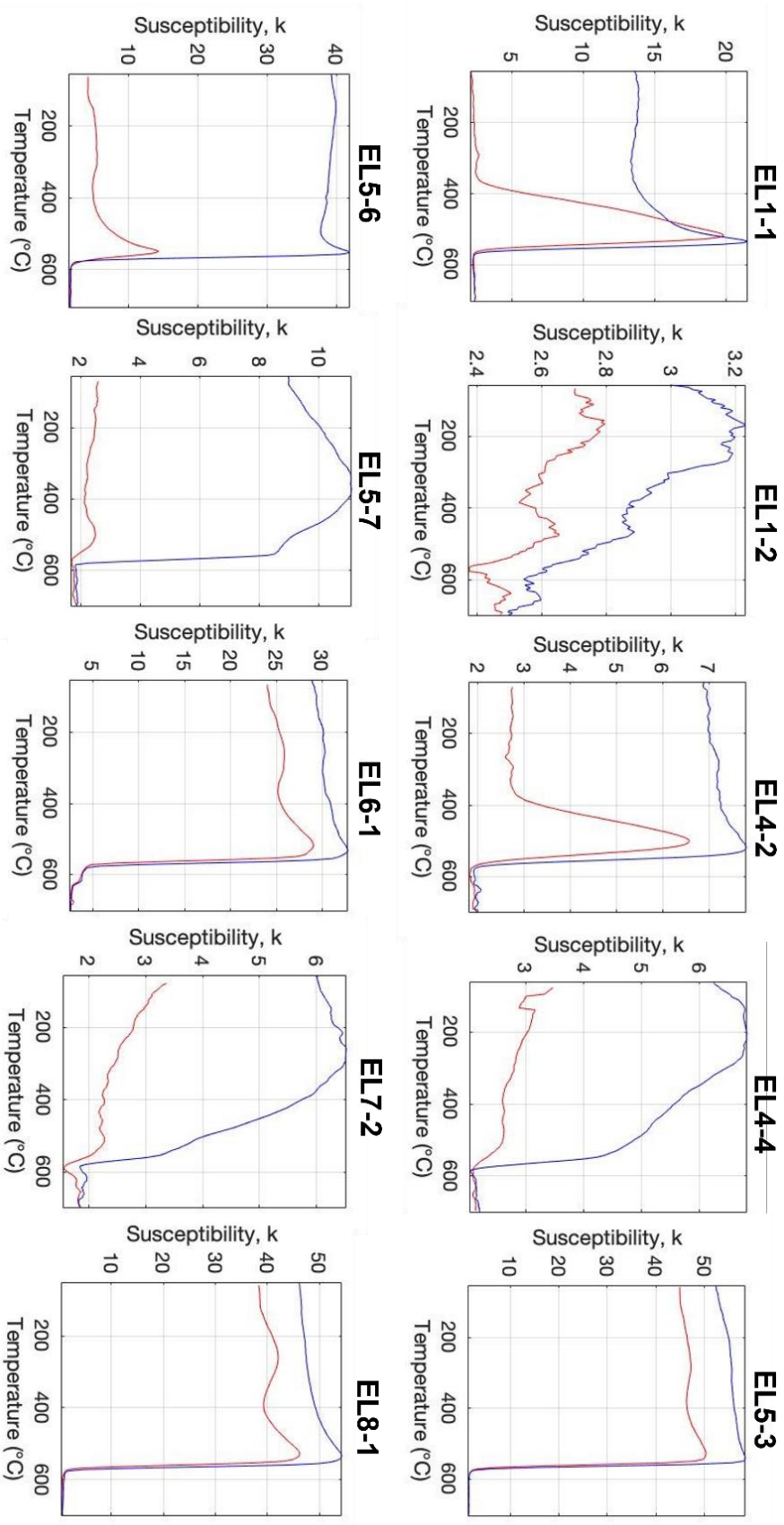
Appendix B: Curie temperature curves showing magnetic susceptibility as a function of temperature (heating = red, cooling = blue). These specimens were selected based on hysteresis data that raised questions about magnetic mineralogy. EL1-2, EL4-4, EL5-7, and EL7-2 have extremely noisy data, most likely as a result of very low magnetic susceptibility.

76

APENDIX C

Raw Anisotropy Data

Specimen	Field	Frequency	Kmean	L	F	P	Pj	T	U	Q	E	Kmax_Dec	Kmax_Inc	Kint_Dec	Kint_Inc	Kmin_Dec	Kmin_Inc	FTest_F	FTest_F12	FTest_F23	E12	E23	5	E13
*EL1-1A-BOT	200	976	7.32E-05	1.0059	1.0106	1.0165	1.0168	0.2882	0.2844	0.4357	1.0047	101.3	21	358.6	29.8	221	52.2	141.4	41.4	122.3	9.4	3.4	2.5	3.5
*EL1-1B-BOT	200	976	1.01E-04	1.0034	1.0143	1.0178	1.0189	0.6127	0.6099	0.2161	1.0109	112.6	16	17.5	17	243.3	66.3	283.3	23	387.7	14	2.9	2.1	2.9
*EL1-1B-TOP	200	976	7.21E-05	1.005	1.0127	1.0177	1.0183	0.4368	0.4332	0.3302	1.0077	89	20.7	350.1	22.2	217.7	58.8	389.9	63.9	418.2	7	2.8	2.1	2.1
*EL1-1C-TOP	200	976	7.05E-05	1.0074	1.0124	1.02	1.0202	0.249	0.2443	0.4658	1.0049	89.3	29.3	344.2	25	220.8	49.8	257.1	80.9	215.7	6.3	3.8	2.5	2.8
*EL1-1C-BOT	200	976	7.44E-05	1.0057	1.0136	1.0193	1.0199	0.4089	0.4049	0.3495	1.0079	84	28.6	340	24	216.5	51.1	160.8	30.8	170.5	10	4.3	3.8	3.1
*EL2-1A-TOP	200	976	3.51E-04	1.0095	1.0225	1.0323	1.0331	0.3947	0.3566	0.3495	1.0128	72.4	44.6	325.3	16.6	220.5	40.8	486.5	89.5	548.2	6.2	3	2.5	2
*EL2-1A-BOT	200	976	4.06E-04	1.0086	1.0086	1.036	1.0376	-0.5199	-0.5135	1.2257	0.982	49.7	46.4	145.2	5.2	240.2	43.1	1856.1	741.4	260.1	1.4	1.7	1	2
*EL2-1B-BOT	200	976	3.44E-04	1.0271	1.0051	1.0361	1.036	-0.5135	-0.5199	1.0058	0.982	76.3	48.2	322.4	19.9	217.7	35	2052.4	741.4	1138.4	1.7	1	0.4	4.5
*EL2-1C-TOP	200	976	4.22E-04	1.0149	1.0209	1.0361	1.034	0.1641	0.1554	0.5333	1.0058	79.4	44	327.6	21.1	219.8	38.5	741.4	1623.5	1623.5	1.1	1.3	0.8	3
*EL2-1C-BOT	200	976	4.08E-04	1.0138	1.0199	1.0338	1.0363	0.1766	0.1685	0.5248	1.0059	94.5	36.4	340	29.3	222.2	39.7	1184.4	619.9	1483.2	2.1	1.3	0.8	2
*EL2-2A-BOT	200	976	3.62E-04	1.0166	1.0165	1.0334	1.0334	-0.0022	-0.0104	0.6759	0.9999	94.5	36.4	340	29.3	250.6	17.1	929.1	673.7	719.4	2.2	2.2	0.7	1.8
*EL2-2A-TOP	200	976	3.30E-04	1.0093	1.0051	1.0144	1.0146	0.3359	0.3313	0.4015	1.0058	147.5	4.1	23	56.2	250.6	72.1	673.7	670	203.8	2.8	5.3	2.2	1
*EL2-2B-TOP	200	976	4.25E-04	1.0166	1.0139	1.0209	1.0213	0.3359	0.3313	0.4015	1.007	115.4	8.6	23	56.2	233.2	72.4	929.1	219.4	960.4	2.6	2.7	1	1.6
*EL2-2B-BOT	200	976	4.08E-04	1.0138	1.0051	1.0144	1.017	0.4378	0.4345	0.3293	1.0072	121.9	3.9	29.7	29.7	218.6	60	546.8	636.2	203.8	6.9	5.3	2	1.3
*EL2-2C-TOP	200	976	3.44E-04	1.0063	1.0144	1.0188	1.0197	0.5386	0.5353	0.2629	1.0101	311	0.6	41.4	1.2	172.8	33.3	792.7	102.8	1033.6	7.2	2.1	0.9	1.6
*EL2-2C-BOT	200	976	4.33E-04	1.0022	1.0125	1.0189	1.0191	0.3295	0.3255	0.4058	1.0062	281.9	11.6	18.5	29.5	172.8	57.9	582.5	155.6	654.2	4.6	2.5	0.8	1.5
*EL2-2D-TOP	200	976	1.14E-03	1.0168	1.0191	1.0209	1.0211	0.7655	0.7655	0.1257	1.0146	312.3	37.9	186	11.6	44.7	3.1	525.9	11.1	764.6	15.3	2.5	2.2	2.5
*EL2-2D-BOT	200	976	8.68E-04	1.041	1.0289	1.0711	1.0715	-0.1708	-0.1874	0.8444	0.9883	341.5	11	90.1	58.7	245.3	28.9	56630.9	44290.4	18845.7	0.3	0.4	0.2	2.2
*EL3-1A-TOP	200	976	5.48E-04	1.0153	1.0189	1.0584	1.0595	-0.3536	-0.3411	1.023	0.9808	339.2	61.4	91.2	61.4	243.5	25.8	5612.9	5531.3	1138.4	0.8	1.6	0.6	3.1
*EL3-1A-BOT	200	976	5.65E-04	1.0304	1.04	1.0659	1.0578	-0.4421	-0.4311	0.3316	1.0243	201.1	0.9	291.4	23	109	67	30602.4	5661.3	35896.8	0.4	0.4	0.3	2
*EL3-1B-TOP	200	976	5.28E-04	1.0172	1.0145	1.0454	1.0463	-0.3504	-0.3601	1.0305	0.9846	10.8	11.9	280.1	3.5	174.1	77.6	14731.2	15268.7	3686.6	1.2	1.2	0.5	1.5
*EL3-1B-BOT	200	976	5.07E-04	1.0223	1.0314	1.0492	1.0498	0.2874	0.2764	0.4417	1.0139	201.8	1.8	292.5	21.3	107.2	68.6	15479.7	4799.2	14994.3	1.1	0.6	0.4	1.3
*EL3-1C-TOP	200	976	5.28E-04	1.0223	1.0263	1.0491	1.0492	0.0821	0.0702	0.6057	1.0039	13.8	1.2	283.4	20.9	106.9	69	792.7	2345.9	3310.4	1.4	1.3	0.7	2
*EL3-1C-BOT	200	976	5.14E-04	1.0244	1.0276	1.0526	1.0526	0.0607	0.0479	0.6248	1.0031	120.4	19	19.7	28.4	239.6	54.8	11701.4	6619	7684.3	0.9	0.8	0.4	1.6
*EL3-1D-TOP	200	976	5.33E-04	1.0205	1.0348	1.0561	1.0567	0.2553	0.2425	0.4672	1.014	126.6	13.6	28.9	29	238.8	57.4	193889.9	6785.9	17747.2	0.5	0.5	0.3	2.5
*EL3-1D-BOT	200	976	1.09E-02	1.0236	1.0259	1.0502	1.0502	0.046	0.0338	0.6369	1.0023	113.9	22.3	339.7	40.8	236.3	52.6	5288.3	2818.3	3305.3	1.3	1.2	0.5	3.1
*EL4-1D-TOP	200	976	1.03E-02	1.0185	1.0344	1.0535	1.0544	0.2978	0.2859	0.4347	1.0157	116.5	45.1	316.4	44.2	208.7	58.8	27001.4	7900.1	26251.4	0.8	0.4	0.2	2
*EL4-1D-BOT	200	976	1.11E-02	1.0127	1.0489	1.0622	1.0657	-0.5824	-0.5723	0.2394	1.0357	83.2	17	18.2	22.1	271.3	5.2	63079.8	47505.3	27007.1	0.3	0.2	0.1	1.2
*EL4-1A-TOP	200	976	1.01E-02	1.0263	1.018	1.0476	1.0476	-0.3267	-0.315	0.9926	0.9837	92	15.5	346.3	44.2	196.3	41.7	561138.8	561138.8	162363	0.2	1.1	1.3	3.5
*EL-4-1B-TOP	200	976	1.01E-02	1.0425	1.018	1.0536	1.0553	-0.6516	-0.6588	1.4171	0.9677	155.2	78.3	1.7	9.9	276	6	70266.8	104692.2	4784.4	0.2	1.1	1	2.9
*EL4-1B-BOT	200	976	9.56E-03	1.0188	1.0206	1.0517	1.0553	0.3089	0.3019	0.4229	1.0097	267.9	21.8	55	64.5	172.8	12.5	1176	386.1	1384.3	3.1	1.7	0.8	2.1
*EL4-1C-TOP	200	976	1.15E-02	1.0238	1.0185	1.0546	1.0548	0.1176	0.1045	0.5769	1.006	87.2	30.3	355.7	46.7	177.1	4.1	6805	3046.1	2116.1	1.2	0.8	0.7	2.5
*EL4-1C-BOT	200	976	1.11E-02	1.0129	1.0247	1.0383	1.0389	0.5806	0.5704	0.2406	1.0113	274.5	48	69.6	39.2	170.1	12.6	3253.2	909.1	3024.2	1	1	0.4	2.1
*EL4-2A-BOT	200	976	2.87E-04	1.0045	1.0124	1.017	1.0176	0.4644	0.4611	0.3114	1.0079	49.4	67.3	275.1	16.3	180.5	15.4	2135.1	375.3	2494.4	3.4	1.2	0.9	0.9
*EL4-2A-TOP	200	976	2.74E-04	1.0045	1.026	1.0307	1.0332	0.7007	0.6968	0.164	1.0214	74.4	87.9	268.2	2.1	178.2	0.5	8801.4	482.5	11579.3	3.3	0.5	0.5	0.5
*EL4-2B-TOP	200	976	2.93E-04	1.0207	1.0155	1.0366	1.0367	-0.1527	-0.1439	0.9948	0.9908	264.5	51.7	359.7	38	231.1	4.1	1151.5	841.9	457	2.6	1.2	0.6	0.8
*EL4-2B-BOT	200	976	2.66E-04	1.0207	1.0292	1.0346	1.0373	0.6946	0.6902	0.1679	1.0239	103.1	23.6	297.3	65.7	195.4	5.3	3626.1	193.4	6121.2	4.5	0.9	0.6	0.8
*EL4-2C-TOP	200	976	2.75E-04	1.0052	1.0346	1.0373	1.0399	0.3688	0.3616	0.3798	1.0123	100.7	38.1	302.9	49.7	199.5	11.1	3496.5	780.4	4000.1	2	1	0.6	0.3
*EL4-2C-BOT	200	976	2.66E-04	1.0105	1.023	1.0338	1.0346	0.4626	0.4467	0.321	1.0377	84.4	5.8	174.4	0.1	265.5	84.2	305442	507219	359493.3	0.3	0.1	0.1	0.1
*EL4-2D-TOP	200	976	2.61E-04	1.0217	1.0603	1.0834	1.0864	0.2989	0.2903	0.321	1.0229	84.8	6.3	354.4	3.4	236.1	82.8	51638.6	13433.2	51554.8	0.6	0.3	0.2	0.2
*EL4-2D-BOT	200	976	2.87E-04	1.0226	1.0461	1.0708	1.0711	0.3362	0.3212	0.4088	1.0229	84.8	6.3	354.4	3.4	236.1	82.8	7321.1	1246.2	8597.2	2	0.3	0.2	0.2
*EL4-2D-TOP	200	976	2.75E-04	1.0221	1.0608	1.0842	1.0873	0.4593	0.4433	0.3234	1.0378	86.5	6.1	356.5	0.5	261.9	83.9	7321.1	1246.2	8597.2	0.8	0.1	0.6	0.6
*EL4-3B-TOP	200	976	2.52E-04	1.0219	1.0472	1.0701	1.0717	0.3614	0.3467	0.3904	1.0248	88	5.3	357.6	4	231.1	83.3	249847.7	61117	259130.9	0.3	0.1	0.1	0.1
*EL4-3B-BOT	200	976	2.75E-04	1.0207	1.0668	1.0888	1.0883	0.5189	0.5033	0.2836	1.0451	83.7	5.2	353.6	0.9	253.3	84.8	31735.4	3484.7	38032.8	0.4	0.4	0.3	0.3
*EL4-3A-TOP	200	976	2.61E-04	1.0198	1.0333	1.0537	1.0543	0.2519	0.2397	0.4694	1.0133	88.6	6.5	357.7	7.9	217.8	79.7	238239	7159.8	20863.8	0.5	0.5	0.3	0.3
*EL4-3A-BOT	200	976	2.75E-04	1.0194	1.0593	1.0726	1.0751	0.4518	0.4378	0.3271	1.0322	79.9	11.9	349.3	3	245.2	77.7	26413.2	3609.2	29167.6	0.9	0.4	0.3	0.2
*EL4-3C-TOP	200	976	5.70E-04	1.0213	1.041	1.0819	1.0849	0.7841	0.7894	0.3196	1.0372	84.6	6.1	354.4	1.5	250.5	83.7	38517.3	5089.5	43207.9	0.3	0.3	0.2	0.3
*EL4-3C-BOT	200	976	5.75E-04	1.0207	1.041	1.046	1.047	0.7486	0.7439	0.1368	1.032	336.2	32.9	82.8	23.8	201.5	47.4	1097.1	42	1862.8	10.7	1.5	0.8	0.8
*EL4-3D-TOP	200	976	5.80E-04	1.0053	1.0375	1.043	1.046	0.5874	0.4489	0.2338	1.022	185.6	33.6	19.3	55.6	279.9	6.4	904.2	95.8	1210.1	7.3	1.8	1.5	1.5
*EL4-3D-BOT	200	976	6.14E-04	1.0077	1.0299	1.0378	1.04	0.4556	0.4477	0.3204	1.0184	184.1	53.3	6.6	36.7	275.7	1.2	7144	128	8090.7	1.9	0.7	0.5	1.3
*EL4-4A-BOT	200	976	5.11E-04	1.0109	1.0408	1.0184	1.0184	0.7715	0.7646	0.1251	1.0184	18.1	57.2	172.6	30.2	269.5	11.6	4017.9	67.4	7178.3	6.5	0.9	0.7	0.5
*EL4-4A-TOP	200	976	5.24E-04	1.0078	1.0618	1.0701	1.077	0.8076	0.8039	0.1031	1.0537	2.9	24.9	159.5	63.2	268.5	9.3	4210.8	128	6738.9	6.8	0.8	0.7	0.7
*EL4-4B-TOP	200	976	5.05E-04	1.0041	1.0396	1.0485	1.0485	0.8076	0.8076	0.1353	1.0353	2.9	24.9	159.5	63.2	268.5	9.3	3755.6	96.5	6205.6	7.2	0.8	0.8	0.8
*EL4-4B-BOT	200	976	5.77E-04	1.0094	1.0402	1.05	1.0532	0.6166	0.609	0.2167	1.0306	31.3	40.2	292.7	10	191.5	48	2555.1	209.7	3652.1	3.9	1	0.8	0.8
*EL4-4C-BOT	200	976	5.05E-04	1.0078	1.0618	1.0701	1.077	0.7715	0.7646	0.1251	1.0537	18.1	57.2	172.6	30.2	269.5	11.6	4017.9	128	7178.3	6.5	0.9	0.7	0.7
*EL4-4C-TOP	200	976	5.26E-04	1.0041	1.0618	1.0701	1.077	0.8076	0.8039	0.1031	1.0353	2.9	24.9	159.5	63.2	268.5	9.3	4210.8	67.4	6738.9	6.8	0.9	0.7	0.7
*EL4-4D-TOP	200	976	5.77E-04	1.0094	1.0402	1.05	1.0532	0.6166	0.609	0.2167	1.0306	31.3	40.2	292.7	10	191.5	48	2555.1	209.7	3652.1	3.9	1	0.7	0.8
*EL4-4D-BOT	200	976	5.44E-04	1.0075	1.0451	1.053	1.0574	0.7115	0.7051	0.1592	1.0374	26.4	43.4	290.6	6.1	194.3	46	4184.6	195	6616.7	4.1	0.7	0.6	0.6
*EL7-1A-TOP	200	976	5.29E-04	1.0293	1.0162	1.046	1.0466	-0.2836	-0.2939	0.9563	0.9873	286.5	11.5	185.8	42.4	28.4	45.3	10234.5	9501.7	2570.5	0.6	1.1	0.4	0.4

78

	200	976																			
*EL7-1A-BOT	200	976	5.86E-04	1.027	1.0133	1.0406	1.0414	-0.3445	1.0126	0.9867	108	0.5	18	88.6	1.4	12382.4	15434.6	3667.5	0.6	1.2	0.4
*EL7-1B-TOP	200	976	5.38E-04	1.0305	1.0092	1.04	1.0418	-0.5317	1.2503	0.9994	281.2	12.4	24.2	41.5	45.8	3450.9	4196.1	338.6	0.9	2.9	0.8
*EL7-1B-BOT	200	976	5.66E-04	1.0313	1.0105	1.0421	1.0438	-0.493	1.201	0.9799	103.2	0.5	13.2	79.2	10.8	4383.5	6234.6	684.2	0.9	2.8	0.6
*EL7-1C-TOP	200	976	5.38E-04	1.0266	1.0078	1.0363	1.0363	-0.5088	1.2637	0.9817	282.9	11.5	20.3	55.3	32.2	3137.4	4218.4	345.2	1	3.2	0.7
*EL7-1C-BOT	200	976	5.62E-04	1.0299	1.0085	1.0386	1.0406	-0.5428	1.2794	0.9792	286.5	8	19.9	65.5	23	3208.6	4581.8	355.9	1	3.5	0.7
*EL7-1D-TOP	200	976	5.43E-04	1.0282	1.0128	1.0414	1.0423	-0.554	1.0535	0.9851	284.3	5.5	17.5	58.9	30.5	5954.9	6652.9	1221.9	0.8	1	0.6
*EL7-1D-BOT	200	976	5.77E-04	1.0166	1.0194	1.0363	1.0364	-0.3713	-0.38	0.9973	279.3	2	9.5	84.6	5	3824	3255.9	2312.6	1.3	1	1.7
*EL7-2A-TOP	200	976	5.10E-04	1.0146	1.0495	1.0649	1.068	-0.0771	-0.086	0.9851	261	2	7.8	84.6	5	34506.5	34506.5	3765.8	0.9	1.5	0.6
*EL7-2A-BOT	200	976	5.29E-04	1.068	1.0532	1.0718	1.068	0.5378	1.0344	0.9973	261	43	42	114	7.8	3824	3255.9	3765.8	0.9	1.5	0.3
*EL7-2B-TOP	200	976	4.99E-04	1.014	1.016	1.0604	1.04	0.5662	1.0387	0.9851	260.8	44.9	41.1	110.4	15.3	15185.3	15185.3	2312.6	1.5	0.5	0.3
*EL7-2B-BOT	200	976	5.30E-04	1.0196	1.04	1.0604	1.016	0.3241	1.02	1.013	261	43	42	111.5	16	1864.9	2020.8	473	2.5	1.4	0.3
*EL7-2C-TOP	200	976	4.66E-04	1.0346	1.0572	1.0567	1.0463	0.3372	1.0203	1.013	259.2	40.1	42.4	111.1	6.3	2275.5	2198.3	819.9	2	1.3	0.8
*EL7-2C-BOT	200	976	4.72E-04	1.0213	1.0346	1.0463	1.0463	0.2208	1.013	1.0006	266.4	38.3	40.1	111.6	0.6	6603.9	7580.6	2198.3	0.8	1.3	0.8
*EL7-2D-BOT	200	976	4.78E-04	1.0226	1.0232	1.0232	1.0463	0.2339	1.0139	0.0026	266.4	38.3	48.9	105.9	6.7	819.9	5214.3	7580.6	0.7	1.3	0.8
*EL7-2D-TOP	200	976	6.13E-04	1.0168	1.0201	1.0427	1.0427	0.3505	1.0155	0.0181	255.3	31	55	112.2	9.7	5300.6	15892.8	5658.6	0.5	1.5	0.8
*EL8-1A-TOP	200	976	8.70E-03	1.0174	1.12	1.1395	1.1524	0.7355	1.1008	0.1504	264.5	31.6	0.5	159.6	56.6	23863.9	41279	41279	2.2	0.4	0.5
*EL8-1A-BOT	200	976	6.31E-03	1.0103	1.1042	1.1156	1.1284	0.8028	1.1029	1.0029	355.4	25.4	0.5	147.5	15.9	55584.4	77472.1	6614.6	1.3	0.4	0.2
*EL8-1B-TOP	200	976	9.29E-03	1.0055	1.1172	1.1233	1.1402	0.9065	0.9012	1.1111	288	22.9	31	164.9	52.4	5386.3	9348.6	22	12.1	0.7	0.6
*EL8-1B-BOT	200	976	9.35E-03	1.0096	1.1163	1.127	1.1422	0.7793	0.8403	1.0021	31.6	23.3	290.7	158.4	55.5	3471.8	3471.8	657.2	1	0.1	0.1
*EL8-1C-TOP	200	976	1.24E-02	1.0138	1.1318	1.127	1.2105	0.8313	1.1237	1.1057	354.5	30.3	7.6	157.5	58.6	55876.3	55876.3	6740.2	1.8	0.2	0.2
*EL8-1C-BOT	200	976	1.05E-02	1.0194	1.1267	1.1377	1.1267	0.64	1.0759	1.0039	51.6	16.8	313.3	171.3	58.7	43065.5	58285	7452.8	1.1	0.3	0.2
*EL8-1D-TOP	200	976	1.39E-02	1.0998	1.1309	1.1976	1.1524	0.5251	1.2695	1.0696	359.2	13.8	8.1	210.8	73.9	182206	187040.6	182206	0.6	0.2	0.1
*EL8-1D-BOT	200	976	8.70E-03	1.027	1.1688	1.1007	1.007	0.3462	1.0142	1.0408	17.1	10.9	0.5	107.4	78.9	31371.6	38154.5	6340.9	0.8	0.4	0.2
*EL9-1A-TOP	200	976	6.62E-02	1.0094	1.0237	1.0033	1.0343	0.4298	1.337	1.0142	113.2	21.1	1.5	252.6	15.9	1131.2	6614.6	1212.8	2.2	0.2	0.2
*EL9-1A-BOT	200	976	5.99E-04	1.0155	1.0209	1.0367	1.0369	0.1488	0.14	1.0054	102.6	5.1	259.8	261.6	1.9	8555.1	6699.8	3313.1	1.1	0.9	0.5
*EL9-1C-TOP	200	976	5.78E-04	1.0289	1.0297	1.0139	1.0152	0.4269	0.421	1.0122	105.6	14.6	31	164.9	13.2	8820.1	9348.6	3986.2	0.7	0.8	0.8
*EL9-1C-BOT	200	976	5.87E-04	1.0082	1.021	1.0294	1.0303	0.4312	0.3316	1.0122	105.6	4.2	290.7	345.4	13.2	3565.8	6740.2	657.2	2.7	1.1	0.6
*EL9-1D-BOT	200	976	6.59E-04	1.021	1.0294	1.034	1.0341	0.4371	0.575	1.0039	100.6	4.2	7.6	260.1	8.8	5845.5	936.1	936.1	2	0.6	0.2
*EL9-1D-TOP	200	976	6.17E-04	1.0188	1.034	1.026	1.026	0.115	1.0039	1.0039	102.3	23.5	313.3	171.3	13.9	5186.7	7452.8	7452.8	1	0.8	0.5
*EL9-2A-TOP	200	976	6.59E-04	1.0132	1.026	1.0286	1.0286	-0.0227	-0.0291	0.9994	95.4	4.2	248	288.4	5.4	16873.5	11466.4	1024.6	0.7	2	0.4
*EL9-2A-BOT	200	976	5.39E-04	1.0098	1.018	1.029	1.029	-0.2802	-0.2866	0.9922	105	4.2	217.7	241.7	10	3959.8	3511.3	1201.7	3.3	1.8	0.7
*EL9-2B-TOP	200	976	6.59E-04	1.0115	1.019	1.0232	1.0232	0.3152	0.4179	1.009	108.5	13.6	5.1	15.1	13.7	1612	1580	1580	1.2	2.3	1.1
*EL9-2B-BOT	200	976	5.78E-04	1.0055	1.0037	1.0193	1.0199	0.0074	0.0017	1.0082	139.9	28.3	5.1	242.7	22.4	937.7	622.9	2760.8	2.6	2.3	1.1
*EL9-2C-TOP	200	976	5.87E-04	1.0017	1.0122	1.0139	1.0152	0.7535	0.752	1.0045	58.6	43.1	310	202.8	40.9	2213.5	424.2	1475.7	2.7	2.7	0.8
*EL9-2C-BOT	200	976	7.63E-04	1.0076	1.0197	1.0197	1.0199	0.2269	0.2222	1.0044	50.4	21.3	353.2	180.7	45.2	2531.8	2152.5	37.3	11.2	1.4	0.4
*EL10-1A-BOT	200	976	5.64E-04	1.012	1.0199	1.0214	1.0214	-0.0461	-0.0514	1.0044	244.4	3.2	316.6	203.8	66.4	2531.8	754	2152.5	1.9	1.4	0.3
*EL10-1A-TOP	200	976	5.64E-04	1.0138	1.0112	1.0235	1.0236	-0.183	-0.1886	0.9958	113.9	44	96.6	344.4	15.6	927.5	604.7	558.4	2.2	2.7	0.8
*EL10-1B-BOT	200	976	1.39E-02	1.0675	1.119	1.1945	1.1947	0.2655	0.2239	0.999	8.9	32	96.6	344.4	42.2	1954.6	2001.7	918	1.6	2.3	0.8
*EL10-1B-TOP	200	976	1.39E-02	1.39E-02	1.119	1.1945	1.1945	0.2655	0.4815	1.0483	88	6	356.5	200.2	74.4	24298.6	34969.7	918	0.6	0.6	0.2
*EL10-1C-TOP	200	976	1.37E-02	1.1121	1.1121	1.1928	1.192	0.2054	0.5292	1.069	90.4	4.2	359.5	199	77.1	24454.3	18615.2	378.6	0.7	0.5	0.3
*EL10-1C-BOT	200	976	1.66E-02	1.1185	1.1155	1.188	1.191	0.2608	0.1531	1.069	88.5	9.9	355.1	204.2	68.2	99008.4	82865.9	18615.2	0.4	0.3	0.1
*EL10-1D-TOP	200	976	1.56E-02	1.0648	1.1878	1.1903	1.1476	0.2699	0.477	1.0476	84.9	10.3	352	207	73	175854.2	144597.3	144531	0.3	0.2	0.1
*EL10-1D-BOT	200	976	1.27E-02	1.0616	1.139	1.2143	1.0729	0.3291	0.0729	1.0729	87.5	8.8	355.3	208.2	72.5	138196	3821.3	12861.1	0.3	0.5	0.4
EL1-1A-BOT	200	976	1.36E-02	1.139	1.139	1.2091	1.1815	0.3705	0.4031	1.0015	89	8.2	356.7	180.7	73	13819.6	5084.1	2861.1	1.2	0.4	0.3
EL1-1A-TOP	200	976	1.53E-02	1.1398	1.2078	1.1771	1.0771	0.3896	0.3602	1.0815	87.5	14.3	355.3	206.3	71.8	22385.6	5084.1	22444	0.5	0.5	0.4
EL1-1B-BOT	200	976	1.28E-02	1.317	1.2157	1.0614	1.0614	0.3802	0.3967	1.0614	91.6	0.6	1.4	183.3	71.8	30142.5	8046.9	27803.4	0.8	0.3	0.3
EL1-1B-TOP	200	976	1.53E-02	1.662	1.2067	1.2214	1.0614	0.3173	0.443	1.0614	89.5	2.5	358.7	187.2	72.1	13917.8	11705.2	11705.2	1.1	0.4	0.3
EL1-1C-BOT	200	976	5.64E-04	1.0267	1.0292	1.0324	1.0243	0.8307	1.0243	1.0243	75.3	8.7	218	344.3	6.5	378.6	378.6	378.6	3.7	0.5	0.4
EL1-1C-TOP	200	976	3.31E-05	1.0024	1.0267	1.0292	1.0289	0.8329	0.8779	1.0289	95.3	72	250.5	342.6	7.1	2275.5	918	918	2.8	1.1	2.8
EL1-2A-BOT	200	976	3.31E-05	1.0147	1.0176	1.0325	0.0804	0.8798	0.5971	1.0028	87.7	45.1	295.5	190.6	14.3	10495	86.8	68	71.7	7.4	3.8
EL1-2A-TOP	200	976	4.23E-05	1.0147	1.0176	1.0325	0.0629	0.8779	0.5971	1.0028	87.7	45.1	295.5	190.6	14.3	439.6	86.8	68	35	10.1	3.8
EL1-2B-BOT	200	976	7.38E-05	1.0083	1.0131	1.0217	0.22	0.2251	1.0048	1.0048	91.8	22	313.2	188.9	16.9	25	25	25	18.5	7.4	6.9
EL1-2B-TOP	200	976	6.71E-05	1.0086	1.0163	1.0215	0.3079	0.3023	0.4225	1.0077	82	46.3	307.2	199.8	24	364.4	364.4	25	5.9	3.2	1.9
EL1-2C-BOT	200	976	8.33E-05	1.0091	1.0127	1.022	0.1626	0.1574	0.5338	1.0035	87.5	42	312.1	201.3	24.2	72.8	32.4	64.8	10	7.6	4.1
EL1-2C-TOP	200	976	2.81E-04	1.0059	1.0396	1.0457	0.7378	0.7327	0.1432	1.0335	312.3	44.7	103.3	207	14.9	9918.3	337.6	13374	3.6	0.5	0.5
EL1-2D-BOT	200	976	2.01E-04	1.0047	1.0204	1.0268	0.6212	0.6174	0.2115	1.0156	311.3	41.9	99.1	205.6	16.8	621.6	44.2	872	9.6	2.5	2
EL1-2D-TOP	200	976	1.92E-04	1.0142	1.018	1.0324	0.1174	0.1096	0.5727	1.0038	329.6	65.6	108.6	203.8	14.9	1567.5	779.6	1212.8	2.7	6.2	1.2
EL1-2E-TOP	200	976	1.55E-04	1.0173	1.0144	1.0356	0.0205	0.0118	0.6563	1.0007	315.2	58.5	104.3	203.8	13.7	237.4	144.5	151.5	6.2	6.1	3.1

79

Label																					
EL1-2E-BOT	200	976	2.40E-04	1.0145	1.0129	1.0275	1.0275	-0.0594	-0.0662	0.7268	0.9984	309.9	39.5	103	208.3	13.7	2111.2	1305.9	1145.6	1.7	2.2	1
EL1-3A-TOP	200	976	7.82E-05	1.0087	1.0061	1.0257	1.0261	0.3082	0.3139	0.4183	1.008	269.8	4.4	0.3	142.9	82.7	25.1	7.2	24.8	25.7	13.9	9.5
EL1-3A-BOT	200	976	1.06E-04	1.0168	1.0168	1.0253	1.019	0.8364	0.8347	0.0862	1.019	102.4	1.5	12.4	219.3	86.6	63.6	0.8	103.2	52.3	6.9	6.5
EL1-3B-TOP	200	976	3.50E-05	1.0236	1.0227	1.0366	1.0372	0.9657	0.9895	0.9657	0.9895	99.5	3.8	189.6	299.7	86	31.2	30.5	9.3	12.1	22.8	8.3
EL1-3B-BOT	200	976	8.17E-05	1.0044	1.0109	1.0157	1.0065	0.4257	0.4226	0.3374	1.0065	87.2	4.4	354.5	184.1	57.7	50.9	10.7	50.4	20.7	7.3	6.2
EL1-3C-TOP	200	976	8.19E-05	1.0076	1.0124	1.0153	1.0047	0.2366	0.2319	0.4753	1.0047	297.9	4.1	28.7	187.1	78.5	38.9	11.3	32.9	16.4	11.3	7.3
EL1-3C-BOT	200	976	8.75E-05	1.0079	1.0124	1.0203	1.0051	0.2461	0.2312	0.4682	1.0051	270.6	2.3	1.1	168.9	78.8	52.9	18.6	46.5	16.7	9.9	6.5
EL1-3D-TOP	200	976	3.43E-05	1.0081	1.0243	1.0339	1.0161	0.4985	0.4924	0.2907	1.0161	269	3.8	4.5	176.4	34	10.9	2	17.3	40.6	16.4	10.4
EL1-3D-BOT	200	976	3.71E-05	1.0085	1.0306	1.0326	1.0133	0.4402	0.4341	0.3296	1.0133	88.7	9.9	345.5	185.9	35.6	41.6	9.6	61.2	22	9	5.6
EL2-1C-BOT	200	976	2.97E-04	1.0088	1.0219	1.0219	1.0042	0.1911	0.1859	0.5111	1.0042	99.3	10.4	2.3	257.5	54.3	910.3	265.6	740.8	3.1	2.6	1.6
EL2-1C-TOP	200	976	4.72E-04	1.0084	1.013	1.021	1.004	0.1928	0.1878	0.5096	1.004	108	9.4	11.1	268.6	52.6	763.6	232.8	624	3.4	2.8	1.6
EL2-1B-BOT	200	976	3.16E-04	1.0084	1.0219	1.0219	1.0042	0.1928	0.1878	0.5096	1.004	108	9.4	11.1	268.6	52.6	763.6	232.8	624	3.4	2.8	1.6
EL2-1B-TOP	200	976	3.17E-04	1.0098	1.0144	1.0245	1.0046	0.1856	0.1914	0.5113	1.0046	15.5	22.1	114.9	245.2	57.9	2131	668.7	1754.2	2.2	1.7	1
EL2-1B-BOT	200	976	3.20E-04	1.0064	1.0176	1.0242	1.0011	0.4591	0.4591	0.3128	1.0011	334	7.6	67	225.3	67.4	10904	179.3	1324.2	5.1	1.9	1.4
EL2-1C-TOP	200	976	3.04E-04	1.0077	1.0139	1.0217	1.0061	0.2846	0.2796	0.4393	1.0061	96.3	3.4	188.7	283.3	54.2	3155.4	761.4	2843	1.9	1.2	0.8
EL2-1C-BOT	200	976	2.50E-04	1.0178	1.0245	1.0254	1.0111	0.455	0.4502	0.3187	1.0111	98.9	3.9	5.9	270.9	52	10706	136.2	1196.4	4.5	2	1.5
EL3-1A-BOT	200	976	4.72E-04	1.0549	1.1605	1.0671	1.6784	1.6784	-0.8251	-0.8204	0.953	79.6	38.9	304.1	190.8	24.2	3050.7	5143.9	44.5	0.9	8.7	15
EL3-1A-TOP	200	976	4.68E-04	1.0075	1.0536	1.0581	1.0381	0.7153	0.7089	0.157	0.953	108.2	7.7	13.5	210.7	57.9	738504	2767	113371.5	1.1	0.2	0.2
EL3-1B-BOT	200	976	4.63E-04	1.0113	1.0539	1.0658	1.0422	0.6389	0.7089	0.157	1.0422	115.8	9	21	222.1	60.8	29461.7	1698.3	41949.8	1.3	0.3	0.3
EL3-1B-TOP	200	976	4.54E-04	1.0064	1.0452	1.0562	1.0386	0.743	0.7486	0.1373	1.0386	302.6	0.5	32.8	211.7	62.6	60589.3	1537	89262.6	1.3	0.2	0.2
EL3-1C-BOT	200	976	4.68E-04	1.0106	1.0562	1.0597	1.0341	0.6047	0.6133	0.2317	1.0341	97.6	22.5	355.5	222	53.8	502579	4661.8	78976.4	1	0.3	0.2
EL3-1C-TOP	200	976	5.62E-04	1.0306	1.0378	1.0402	1.0234	0.6246	0.6189	0.2106	1.0234	291	0.9	21.5	199.4	59.2	933855	5507.6	124992.7	0.7	0.3	0.2
EL4-3C-BOT	200	976	2.53E-04	1.0192	1.0306	1.0378	1.0402	0.5264	0.5118	0.278	1.0431	88.8	3.5	356.6	184.3	57.8	2450806	35442.2	272946.9	0.4	0.1	0.1
EL4-3C-TOP	200	976	1.10E-02	1.0381	1.0984	1.0991	1.0192	0.1796	0.516	0.8.7	1.0431	101.9	1.9	8.7	193.1	30.5	380.3	161.8	265.9	5.5	3.2	2.2
EL4-3B-BOT	200	976	4.66E-04	1.0131	1.0561	1.0744	1.0699	0.6144	0.6038	0.2199	1.0424	81.7	9.8	346.2	188.4	59	10404.5	924.7	14359.3	2.5	0.6	0.5
EL4-3B-TOP	200	976	4.03E-04	1.0139	1.0486	1.0501	1.0201	0.4189	0.4091	0.3466	1.0201	90.1	3.7	357.3	185.2	53.5	2256.1	490	2186.7	3.1	1.1	0.9
EL4-3A-BOT	200	976	6.19E-04	1.0278	1.0377	1.0391	1.0181	0.484	0.4769	0.3009	1.0181	90	5.9	356	188.5	55	23035	3906.3	24686.4	1.1	0.3	0.3
EL4-3A-TOP	200	976	4.06E-04	1.0153	1.0325	1.0493	1.0391	0.355	0.3447	0.3919	1.0169	87	2.9	354.8	180.8	52	14530.4	3905.6	12763	1.1	0.5	0.4
EL3-3C-BOT	200	976	2.53E-04	1.0192	1.0631	1.0835	1.0875	0.5264	0.5118	0.278	1.0431	88.8	3.5	356.6	184.3	57.8	2450806	35442.2	272946.9	0.4	0.1	0.1
EL5-3C-TOP	200	976	1.10E-02	1.0381	1.0984	1.0991	1.0192	0.1796	0.516	8.7	1.0431	101.9	1.9	8.7	193.1	30.5	380.3	161.8	265.9	5.5	3.2	2.2
EL5-4B-BOT	200	976	5.89E-03	1.0436	1.0992	1.1361	1.0634	0.4818	0.4571	0.3141	1.0634	333.2	38	83.5	197.4	42.5	1720	151.5	2193.4	4.2	1.6	1.1
EL5-4A-BOT	200	976	6.12E-03	1.0151	1.1204	1.1373	1.1511	0.7667	0.7533	0.3202	1.1037	2.9	43.1	99.9	197.5	46	578.2	19.1	987.7	15.7	3.5	2.9
EL5-4A-TOP	200	976	5.66E-03	1.0086	1.1107	1.1202	1.1348	0.8492	0.8412	0.0827	1.1012	330.2	31.6	75.1	194.4	49.4	240.9	3.1	434.2	34	1.4	1
EL5-3C-BOT	200	976	1.09E-02	1.0592	1.1689	1.1749	1.0528	-0.7253	-0.7331	1.5291	0.9528	91.3	6.4	353.7	186.6	39.7	49454	72798.9	1380.6	0.3	0.2	0.2
EL5-3C-TOP	200	976	1.09E-02	1.0087	1.0749	1.0749	1.0521	-0.7387	-0.7462	1.5496	0.9521	91.7	7.1	353.2	187.5	39.2	1088342	161034.3	2703.3	0.2	1	0.1
EL5-3C-BOT	200	976	9.61E-03	1.0519	1.0823	1.0834	0.9782	-0.2974	-0.2974	0.9602	0.9782	79.2	18.6	324.5	181.7	32.8	32567.7	318870.8	7853.4	0.6	1.1	0.2
EL5-4C-BOT	200	976	6.91E-03	1.024	1.1285	1.1556	1.1678	0.6716	0.6514	0.1909	1.102	355.5	43.7	101.2	206.1	42	19146.1	1278	28042.9	2	0.4	0.4
EL5-4C-TOP	200	976	1.59E-02	1.0168	1.0702	1.0882	1.0937	0.5916	0.5916	0.2274	1.0525	324.5	14.4	72.3	223.7	36.2	363	3.8	52.5	29.5	7.7	6.1
EL5-4C-TOP	200	976	6.43E-03	1.0128	1.0746	1.0956	1.0611	0.7003	0.6894	0.1684	1.0611	295.6	6	31.5	199.6	44.7	4572.7	176.6	6472.5	4.1	0.9	0.7
EL5-5A-BOT	200	976	1.65E-02	1.0149	1.0718	1.0877	1.0939	0.6485	0.6562	0.2001	1.056	325.2	18.9	76.6	220.2	37	220.7	3.1	57.3	31.7	7.4	6
EL5-5B-TOP	200	976	1.82E-02	1.0111	1.0602	1.0939	1.0776	0.6827	0.6734	0.1778	1.0486	103.7	25.2	348.5	214.8	37.3	34.1	2.2	52.1	36.7	7.6	6.5
EL5-5B-BOT	200	976	1.84E-02	1.0105	1.0578	1.0743	1.0776	0.6873	0.6784	0.1749	1.0468	106.6	19.4	357.1	214	43.5	39.4	2.5	59.8	35.4	7	6.1
EL5-5B-TOP	200	976	1.85E-02	1.0035	1.068	1.0718	1.0812	0.8979	0.8945	0.0542	1.0642	332	30.6	89.4	215.4	37.1	38.1	0.2	71.2	65.9	6.8	6.2
EL5-5C-BOT	200	976	1.90E-02	1.0033	1.0629	1.0664	1.0751	0.898	0.8948	0.054	1.0594	304.3	2.9	38.5	212.3	35	41.4	0.3	76.7	65.3	6.6	6
EL5-5E-TOP	200	976	1.82E-02	1.0376	1.0594	1.0602	1.0162	0.2787	0.2654	0.45	1.0162	107.7	32.9	342.7	220.5	30.9	46	16.4	46	14.8	8.3	5.2
EL5-5E-BOT	200	976	1.93E-02	1.0173	1.0376	1.0601	1.0244	0.4014	0.4014	0.352	1.0244	106.7	32.3	346.8	223.1	35.2	38.6	9	143	19.7	8.2	5.7
EL5-6A-TOP	200	976	2.26E-03	1.0259	1.0587	1.0587	1.006	0.0907	0.1048	0.5884	1.006	85.2	24.3	338.1	204	46.9	233.9	109.1	143	5.9	4.5	2.7
EL5-6A-BOT	200	976	1.85E-03	1.0301	1.0545	1.0545	1.0063	0.1179	0.1048	0.5766	1.0063	79.7	32.2	317.5	194.1	33.1	173.6	92.7	120.8	6.9	4.9	2.9
EL5-6B-TOP	200	976	1.26E-03	1.0237	1.0484	1.0498	1.1016	-0.4109	-0.4207	1.1016	0.9808	89.4	24.1	343.6	209.9	48.7	156.7	167	27.5	4.4	10.6	3.2
EL5-6B-BOT	200	976	1.87E-03	1.0248	1.0456	1.0456	1.006	-0.0973	-0.1083	0.7666	0.9957	88.5	22.6	317.9	188.9	22.6	139.9	123.3	74.5	6	7.1	3
EL5-6C-TOP	200	976	3.91E-03	1.0119	1.051	1.0533	1.0264	0.5235	0.5144	0.2764	1.0264	93.9	13	348.4	194.2	37.9	593.2	83.5	761.1	6.5	2	1.5
EL5-6C-BOT	200	976	3.15E-03	1.0157	1.0301	1.047	1.0141	0.3103	0.3001	0.4242	1.0141	86.7	19	336.1	192.4	38.2	243.4	74.9	236.1	7	3.5	2.4
EL5-6D-TOP	200	976	3.15E-03	1.0217	1.0402	1.0637	1.0182	0.2961	0.2821	0.4374	1.0182	95.5	14.3	358.1	210.7	59.1	2587.4	647.2	2334.6	2.1	1.3	0.8
EL5-6D-TOP	200	976	5.64E-04	1.0113	1.0186	1.0544	1.0451	-0.3042	-0.3162	0.984	0.984	92.7	17	354.4	213.3	58.9	306.1	81.3	81.3	3.3	6.8	2.4
EL5-7A-TOP	200	976	5.64E-04	1.0352	1.0451	1.0553	1.0203	0.4645	0.4727	0.3092	1.0203	92.5	14.5	348.6	196.8	43.6	85.8	15.2	97.4	17	5.7	4.6
EL5-7A-BOT	200	976	7.78E-04	1.0467	1.0579	1.1073	1.1075	0.1043	0.079	0.5982	1.0107	257.1	0.9	352.1	166.9	10.5	234.5	157.7	217.9	5.6	4.8	2.2
EL5-7B-BOT	200	976	5.43E-04	1.0064	1.0102	1.0167	1.0168	0.2311	0.2272	0.4789	1.0038	101.9	12.5	337.2	195.8	16.9	211.3	81.1	193.9	8.1	4.9	3.1
EL5-7B-TOP	200	976	5.04E-04	1.0335	1.0167	1.0424	1.0201	-0.7141	-0.7188	1.5069	0.9729	314.7	46.3	47.6	140.2	43.6	172.2	292.8	7.6	4	22.4	3.1
EL5-7C-TOP	200	976	4.72E-04	1.0079	1.0055	1.0199	1.0039	0.1985	0.1937	0.5049	1.039	22.7	7.3	281.7	187	32.9	66.6	30.4	64.7	11.6	7.7	4.2
EL5-7C-BOT	200	976	7.04E-04	1.0112	1.0201	1.0279	1.0274	0.547	0.5383	0.261	1.0274	116.5	55	324.8	226.4	13.4	6781.1	666.1	817	2.1	0.7	0.5
EL6-1A-TOP	200	977	4.62E-03	1.0255	1.0389	1.0506	1.0531	0.3532	0.336	0.3981	1.0279	201.1	12.3	51.2	319.7	6.8	3493.5	960.3	3041.7	2.3	1	0.8
EL6-1A-BOT	200	977	4.48E-03	1.0301	1.0483	1.0798	1.0805	0.2284	0.2102	0.4921	1.0177	143.6	81.9	47.5	317.4	8.1	441148.7	172357.4	311642.4	0.2	0.1	0.1

Sample																						
EL6-1B-TOP	200	977	5.15E-03	1.0323	1.083	1.0719	1.072	0.0839	0.0667	0.6087	1.0058	160.5	83.7	41.3	3.1	311	5.5	8850.1	4758	4743.9	1	0.7	0.5
EL6-1B-BOT	200	977	5.41E-03	1.0284	1.0409	1.0704	1.0708	0.1786	0.1621	0.53	1.0122	141.1	86.5	36.7	0.9	306.6	3.4	10598.1	4625.3	6937.6	1.1	0.6	0.4
EL6-1C-TOP	200	977	4.92E-03	1.0345	1.0448	1.0808	1.081	0.1275	0.1083	0.5737	1.0099	157.5	83.2	40.3	3.1	310	6	439032.6	216933.5	257120.4	0.2	0.1	0.1
EL6-1C-BOT	200	977	5.16E-03	1.0297	1.0489	1.08	1.0808	0.2406	0.2224	0.4826	1.0187	180.8	82.2	40.5	6	310	4.9	11568.8	4375.3	8268.8	1.1	0.6	0.4
EL6-1D-TOP	200	977	5.10E-03	1.0307	1.0489	1.0811	1.0818	0.2245	0.206	0.4953	1.017	201.1	76.6	41.1	12.6	310.1	4.4	167151.5	64958.5	116457.4	0.3	0.2	0.1
EL6-1D-BOT	200	977	5.83E-03	1.0357	1.0862	1.0811	1.0865	0.152	0.1317	0.5545	1.0126	177.3	83.7	42.2	4.5	311.9	4.4	9820.9	4597.5	5926	0.7	0.7	0.5
EL6-1A-TOP	200	977	1.16E-02	1.0157	1.0428	1.0862	1.0613	0.4572	0.4458	0.3217	1.0267	264.9	34.3	140.4	39.7	311.6	31.6	1690.6	304.4	2192.6	1.3	0.7	0.5
EL8-1A-BOT	200	976	8.07E-03	1.0096	1.0492	1.0593	1.0637	0.6682	0.6602	0.1857	1.0393	270.9	30.4	155.8	35.8	29.6	39.3	21721.7	1391.2	35466.3	1.6	0.4	0.3
EL8-1A-TOP	200	976	1.16E-02	1.0157	1.0428	1.0592	1.0613	0.4572	0.4458	0.3217	1.0267	264.9	34.3	140.4	39.7	311.6	31.6	54392.2	8777.3	70508	3.3	1.1	0.7
EL8-1B-BOT	200	976	5.96E-03	1.015	1.0443	1.0604	1.0628	0.4774	0.466	0.3081	1.0284	265.5	37.3	141.8	36.1	24.3	32.3	9925.1	1196.7	1467	1.1	0.5	0.3
EL8-1B-TOP	200	976	7.13E-03	1.0122	1.0428	1.0555	1.0583	0.2586	0.542	0.2586	1.0302	271.8	33.5	152.2	36.8	30	35.5	2546.6	1751.6	2131.2	1.6	1.5	0.7
EL8-1C-TOP	200	976	4.46E-03	1.0169	1.019	1.0362	1.0363	0.0587	0.0498	0.6231	1.0021	280.5	22.6	159.6	50.9	24.4	29.9	18485.2	10575	12412.2	0.6	0.2	0.2
EL8-1C-BOT	200	976	4.93E-03	1.0265	1.0306	1.0579	1.0579	0.0704	0.0564	0.6175	1.004	279.6	21.5	103.1	68.5	10.1	1.2	2958.2	1024.2	2793.1	1.8	0.6	0.7
EL8-1D-TOP	200	976	1.26E-02	1.0227	1.0382	1.0618	1.0625	0.2519	0.2378	0.4708	1.0152	266.2	24.3	85.9	65.7	176.2	0.1	10279.9	10842.2	3842.8	0.6	1.1	0.3
EL8-1D-BOT	200	976	1.07E-02	1.026	1.0382	1.0417	1.0421	-0.2588	-0.2683	0.9286	0.9895	262.6	19.4	140	56.8	2.4	25.8				1.1	1.1	0.3
EL8-1D-TOP	200	976	1.26E-02	1.0152	1.0618	1.0625	1.0625	0.2519	0.2378	0.4708	1.0152	275.2	19.7	146.8	60	13.4	21.6				0.6	1.1	0.2
EL8-1E-TOP	200	976	1.05E-02	1.0166	1.0399	1.0571	1.0588	0.408	0.3963	0.3555	1.0229	275.2	19.7	146.8	60	13.4	21.6	25141	5481	30812.2	0.8	0.4	0.2
EL8-1E-BOT	200	976	9.47E-03	1.0148	1.037	1.0524	1.054	0.4233	0.4128	0.3441	1.0219	278.7	18.8	158.9	55.6	19	27.6	2150.4	476.1	2861.5	3	1.3	0.8